Spectroscopic characterization of upconversion nanomaterials with systematically varied material composition and surface chemistry

Dissertation

zur Erlangung des akademischen Grades

doctor rerum naturalium (Dr. rer. nat.)

im Fach: Physik

Spezialisierung: Experimentalphysik

eingereicht an der

Mathematisch-Naturwissenschaftliche Fakultät

der Humboldt-Universität zu Berlin

von

Marco Kraft

Dekan: Prof. Dr. Elmar Kulke

Gutachter/in: 1. PD Dr. Stefan Kirstein

2. Prof. Dr. Oliver Benson

3. Prof. Dr. Michael Kumke

Datum der Einreichung: 15.10.2018

Datum der Promotion: 21.12.2018

Zusammenfassung

Ziel dieser Doktorarbeit war es, den Einfluss von verschiedenen Parametern auf die spektroskopischen Eigenschaften von Lanthanid-basierten Aufkonversions-Nanomaterialien zu erforschen. Ein besonderer Fokus lag dabei auf hexagonalen $NaYF_4$ Kristallen, die mit Yb^{3+} und Er^{3+} oder Tm^{3+} Ionen kodotiert wurden. Diese Kristalle sind in der Lage, nach der Absorption mehrerer Photonen im niederenergetischen nahinfraroten Lichtbereich höherenergetische Photonen im ultravioletten-, sichtbaren- und nahinfraroten Lichtbereich auszusenden. Da biologisches Gewebe in diesen nahinfraroten Bereich besser lichtdurchlässig ist als im höherenergetischen Spektralbereich, eignen sich diese Kristalle daher unter anderem besonders für biologische Anwendungen in Bereichen der Bildgebung, Diagnose und Therapie. Andere Applikationen liegen in der Echtheitskodierung, zum Beispiel in Geldscheinen, der Superauflösungs-Mikroskopie und auch in der Photovoltaik.

Eine wesentliche Voraussetzung für mögliche Anwendungen dieser Kristalle ist ein Verständnis aller ihrer wichtigen photophysikalischen Besonderheiten. Die erste Studie dieser Doktorarbeit untersuchte daher, wieso Nanokristalle viel weniger absorbierte in ausgesendete Photonen umwandeln als mikrokristalline Teilchen. Die Ergebnisse zeigten, dass man ungeschalte Kristalle aufgrund von Oberflächen-Lösch-Effekten in zwei Teile unterteilen kann, einen strahlenden Kern und eine Schale aus stark oder vollständig gelöschten oberflächennahen Lanthanid-Ionen, welche für Kristalle abnehmender Größe einen immer größeren Volumenanteil einnimmt. Die zweite Studie untersuchte exemplarisch, ob eine kompliziertere Partikelarchitektur, bestehend aus einem einfach-dotierten $Na(Y,Er)F_4$ Kern und $Na(Y,Yb)F_4$ als Schalenmaterial, diesen Effizienzverlust der Lumineszenz reduzieren kann. Die Ergebnisse zeigten jedoch, dass dies nicht der Fall ist. Eine weitere Studie untersuchte den Einfluss der Konzentration der Tm^{3+} Ionen in $Na(Y,Yb,Tm)F_4$ kodotierten Nanokristallen auf die spektroskopischen Eigenschaften dieser Materialien und zeigte, dass für eine maximale Emission im Lichtwellenbereich über 700 nm andere Tm^{3+} Konzentrationen benötigt werden als für maximale Lichtemissionen in den unteren Lichtwellenbereichen. Die letzte Studie untersuchte den Einfluss eines zuvor berichteten Zersetzungsprozesses von exemplarisch ausgewählten $Na(Y,Yb,Tm)F_4$ kodotierte Nanokristallen in wässrigen Dispersionen auf deren spektroskopische Eigenschaften. Mithilfe dieser Ergebnisse war es möglich, mehrere Emissionsbanden als Parameter für das Langzeit-Stabilitäts-Monitoring dieser Materialien zu identifizieren.

Abstract

This PhD thesis investigated the influence of various parameters on the spectroscopic properties of so-called upconversion nanoparticles (UCNPs). A special emphasis was dedicated to hexagonal-phase $NaYF_4$ crystals that were codoped with Yb^{3+} and either Er^{3+} or Tm^{3+} ions. These crystals are able to emit higher energy ultraviolet-, visible- and near-infrared light after the illumination with lower energy near-infrared light, making them, among others because of the high transparency of biological tissue in the near-infrared, ideal for imaging-, diagnostic- and even therapy purposes in the life sciences. Other applications of UCNPs also include security applications, *e.g.* in money bills, super-resolution microscopy and also solar cells.

However, UCNPs can experience no breakthrough in these applications before all of their important photophysical features are understood. The first study of this PhD thesis therefore investigated, why nanocrystalline upconverters with different surface chemistries convert less absorbed to emitted photons than their microcrystalline counterparts. The results revealed that upconverting crystals apparently have to be subdivided into two parts, with one being the luminescent core and the other being a completely dark shell that is quenched by surface effects and assumes an ever increasing volumetric content for small UCNPs. The second study exemplarily investigated, if a more complex particle nanostructure that consisted of a $Na(Y,Er)F_4$ doped core, surrounded by a $Na(Y,Yb)F_4$ doped shell, could overcome these efficiency losses, however, it concluded that it does not. Another study explored the influence of Tm^{3+} doping concentrations of $Na(Y,Yb,Tm)F_4$ codoped nanocrystals on their spectroscopic properties and concluded that different Tm^{3+} doping concentrations are required for a maximum upconversion luminescence in the wavelength regions above 700 nm, than for the wavelength regions below that. The last study of this PhD thesis investigated the influence of a previously reported dissolution process of UCNPs in aqueous solutions on the spectroscopic properties of exemplarily chosen $Na(Y,Yb,Tm)F_4$ codoped nanocrystals. These results were then utilized to identify several upconversion emission bands that can be used as a screening parameter for the long-term stability monitoring of UCNPs.

Schlagwörter:

Aufkonversion, hexagonale $NaYF_4$ Nanokristalle, Quantenausbeute, Lebenszeitmessung, Spektroskopie, Partikelgröße, Wasser, Nanostruktur, Screening-Parameter

Keywords:

Upconversion, hexagonal-phase $NaYF_4$ nanocrystals, quantum yield, lifetime measurements, spectroscopy, particle diameter, water, nanostructure, screening-parameter

Table of Content

1 Introduction

The phrase photon upconversion, or more commonly only “upconversion” (UC), refers to a non-linear process, where a sequential absorption of two or more low energy photons leads to the emission of photons with higher energy. First studies of this process were published around the year 1960 and investigated solid-state infrared quantum counters as a way to extend photon detection to the 1 – 100 µm wavelength range by upconverting them to a lower wavelength. [1-3] Although at this time, and for some later, this research field was only considered as a scientific curiosity. Before that, all known anti-Stokes emissions, where photons with lower energy get “upconverted” by a Raman scattering process into photons with higher energy, involved energies in excess of excitation energies in the order of the kinetic energy of only a few kT. More and more attention was dedicated to this process ever since, resulting in the discovery of different mechanisms that can lead to UC. These mechanisms can either alone, or in combination, result in the emission of higher energy photons. One of those is the so-called triplet-triplet-annihilation (TTA) mechanism, which takes place between two types of chromophores, one absorbing and another emitting kind. The absorption of the low energy photon hereby leads to the population of an excited singlet state of the absorbing chromophore, which in turn leads to the population of a lower lying triplet state of the same chromophore through an intersystem crossing step. The energy is then transferred to the emitter, resulting in a triplet excited state emitter, and a ground state absorber. Two excited triplet state emitters then undergo the process of triplet-triplet-annihilation and consequently excite the higher singlet excited state of one of the two emitter, from where the final luminescence then occurs.

Other key mechanisms are displayed in Figure 1 with their respective efficiency values for a representative example. [3] Two-photon absorption and second-harmonic generation (SHG) processes, *e.g.*, are characterised by the absorption of multiple photons at the same time. Both mechanisms involve intermediate energy states and represent the processes with the lowest efficiencies in this image. Cooperative luminescence and –sensitization mechanisms involve energy transfer processes, either between two ions, or between a pair of ions and a third one. They are typically more efficient than the two-photon absorption and SHG processes, but less efficient than multi-step absorption processes that involve ground- and excited state absorption (GSA and ESA). Lastly, there is also the sequential energy transfer mechanism, which was

introduced with the name “APTE” (addition de photon par transferts d’energie) and is now commonly known as the energy transfer upconversion (ETU) mechanism.

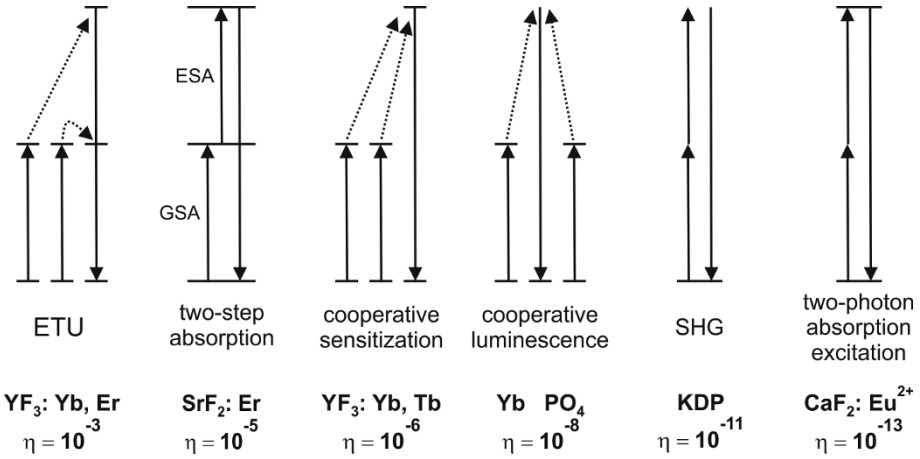

Figure 1: Two-photon UC processes together with their respective typical efficiency, according to Ref [3]. ETU: energy transfer upconversion; GSA: ground state absorption; ESA: excited state absorption; SHG: second-harmonic generation

The ETU process is the most efficient one among the six UC mechanisms that are presented in Figure 1. It furthermore requires a lower excitation power density (*P*) since it does not involve ESA, which typically involves very low absorption cross-sections of the excited states of the emitting ions of most materials. These processes can furthermore be accompanied by energy transfer (ET), or cross-relaxation (CR) processes between identical ions. The CR process is a special kind of energy transfer and typically occurs when a first ion is initially in a higher excited state and exchanges energy with a second ion that is initially in a lower state, resulting in both ions simultaneously changing to intermediate energy states between the two initial states. [4]

Currently used non-linear emitters therefore mainly rely on UC systems that are based on the TTA-, or ETU mechanism. The systems that exploit the ETU process include lanthanide (Ln^{3+})-based so-called upconversion particles (UCPs) that consist of an inorganic crystalline host matrix doped with one or several emissive Ln^{3+} ions and their molecular analogues, *i.e.*, Ln^{3+} complexes. The Ln^{3+} complexes hereby typically consist of an absorbing antenna ligand that is coupled to one of the Ln^{3+} elements, are thereby nanometer-sized and can exhibit large shifts between the absorption and emission wavelengths of over 100 nm, long lifetimes of the intermediate energy levels that are up to a few microseconds long, and sharp emission spectra that are

only tens of nanometers wide. Traditional Ln^{3+} complexes are typically used to "downconvert" higher energy photons into lower energy ones, recent studies, however, also focus on Ln^{3+} complexes that do the opposite and convert *e.g.*, near-infrared (NIR) into visible (vis) light. [5-8] Bimolecular TTA-upconverters combine the energy of two molecules in their excited triplet state to produce the higher energy photon. Their spectroscopic properties can therefore be selected by the use of different chromophores. Their respective excitation and emission wavelengths, *e.g.*, can be tuned between the vis-to-ultraviolet (UV), vis-to-vis, and even NIR-to-vis spectral ranges. [9-11] Some TTA-upconverters with properly chosen absorber/emitter pairs are furthermore able to convert over 30 % of all absorbed lower energy photons into higher energy ones, even at relatively low excitation densities of only tens of $mW \cdot cm^{-2}$. [12]

Both the TTA-upconverters and the Ln^{3+} complexes, however, are out of scope for this Ph.D. thesis, which instead focuses on the crystalline Ln^{3+}-based UCPs, which gained an ever increasing attention since the introduction of solid state lasers, resulting in the first reports of efficient Ln^{3+} based UC in codoped materials in the mid-1970s. [13] The interest in this field increased even further when high brightness UC was later also reported not only in micro-, but also in nanomaterials. [14, 15] Many Ln^{3+} based UCPs have been studied since then with different absorber-emitter, or more commonly "sensitizer"-"activator", pairs and different host matrices. The interest in these systems is especially owed to their unique spectroscopic features, which are principally advantageous for bioanalytical applications, compared with commonly used linear classes of emitters. Some of those features are *e.g.*, their NIR light excitation, which is particularly well suited for deep tissue imaging, the long-lived intermediate energy levels, which allow for an excitation with comparably low energy and inexpensive light sources, the anti-Stokes-shifted emission itself, which can allow for an excellent separation between excitation and emission, and the narrow and multiple emission bands in the UV, vis and NIR regions, which make UCPs ideal for spectral multiplexing and ratiometric measurements. Other interesting features are also their long luminescence lifetimes themselves, which make them ideal for time-gated emission measurements and lifetime multiplexing, the absence of photobleaching or –brightening, which make them ideal for long-term imaging studies, the absence of blinking effects, which opens the doors for single-particle applications, the magnetic properties of some co-dopants (*e.g.* Gd^{3+}), which make them very interesting for combined optical and magnetic resonance imaging, and also their expected low toxicity. [16]

As a result of these features, especially nm-sized UCPs have gained much attention as reporters for theranostics, bioimaging, and multiplex and time-gated assays in complex media, as well as in security and anti-counterfeiting applications and recently owed to the multiphotonic origin of the several emission bands also in super-resolution microscopy. [17-25] The potential use of these Ln^{3+} based UCPs, however, cannot be fully appreciated without a complete understanding of the photophysical features under various conditions. This knowledge is required to create application specific tailor-made bright upconversion nanoparticles (UCNPs).

This Ph.D. thesis therefore dedicated a special attention to four different important issues that were beforehand still not properly and comprehensively addressed in the literature. In short:

(1) The first issue deals with the question why small UCNPs exhibit way lower efficiency values than their microcrystalline counterparts.
(2) The second issue deals with the question if other UC nanostructures can potentially overcome the small efficiency values.

Both were exemplarily addressed for Yb^{3+}, Er^{3+} codoped systems.

(3) The third issue deals with the identification of the optimal doping concentrations that result in the highest UCL of the various Tm^{3+} UCL bands and the (de)population mechanism that lead to them.
(4) The fourth and final issue deals with the investigation of the impact of a previously reported partial dissolution of UCNPs on their spectroscopic properties, aiming to identify an easy to use screening-parameter for the long-term stability of UCNPs. This was exemplarily addressed for Yb^{3+}, Tm^{3+} codoped systems.

2 Fundamentals

2.1 Material requirements for efficient UCPs

The next subchapters focus on what is required from the sensitizer-activator pair and host matrix to allow for an efficient ETU process and which materials fulfil these requirements.

2.1.1 Luminescent centres

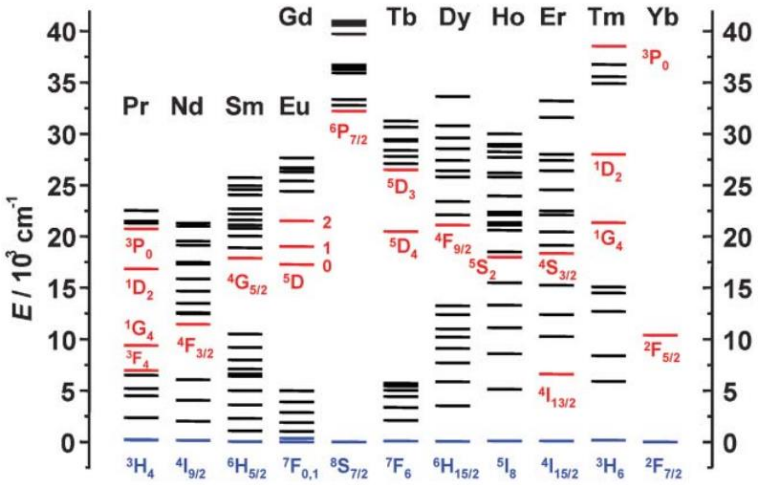

Figure 2: "Partial energy diagrams for the lanthanide ions. The main luminescent levels are drawn in red, while the fundamental level is indicated in blue." Reproduced with permission. [26]

The ETU process first of all requires the presence of absorbing and emitting ions with real and not virtual electronic states. These intermediate real states are required to accumulate a sufficient transient population and therefore to increase the probability of an interaction with the subsequent photons. This is met by systems with parity-forbidden, yet partly allowed optical transitions. Hence, many of the well-known UCP use ions with ladder-like energy levels, such as *e.g.* the trivalent Er^{3+}, Tm^{3+}, Ho^{3+} or Pr^{3+} as luminescent centres (see also Figure 2), embedded in a host matrix with an asymmetrical crystal field to partly allow their f → f transitions. However, these ions have a relatively low absorption cross-section, which is why they are usually codoped with trivalent Yb^{3+}, playing the role of the sensitizing ions that absorb the incoming photons and stepwise transfer the energy to the above mentioned activator ions. All of them have the advantage of retaining their atomic-like emission characteristics due to a high degree of shielding of the f and d orbitals from the chemical environment by the outer-lying s and p electrons. As a result, the energy states of the Ln^{3+} ions behave similar to free Ln^{3+} ions. As also

for other ions, their energy levels are denoted in the Russel-Saunders notation as $^{2S+1}L_J$, using the terms of the spin (S), orbital (L) and total angular momentum (J) of each of their electrons. [27]

2.1.2 Host lattice

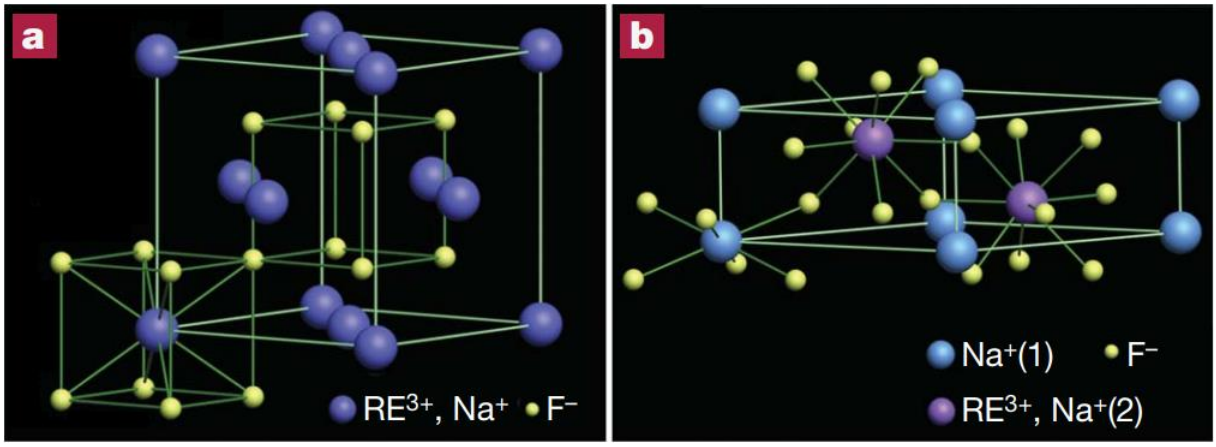

Figure 3: Schematic illustration of the crystal structure of cubic- (**panel A**) and hexagonal-phase (**panel B**) $NaRe_4$ (Re^{3+} = Y^{3+}, Yb^{3+}, Er^{3+}, Tm^{3+}, Ho^{3+}, or Gd^{3+}) structures, respectively. Reproduced with permission. [28]

The host material needs to fulfil a variety of parameters to enable bright and highly efficient UC luminescence (UCL). For instance, it is required to be *transparent to the excitation light and UC emissions*, which is the case for many crystalline lattices with bandgaps greater than around 6 eV, corresponding to the wavelength in the deep UV of 206 nm. Moreover, it should *have a relatively low site symmetry* to efficiently allow the partly forbidden Ln^{3+} transitions. As an example, up to ten times brighter UCL has been observed for Er^{3+} ions in hexagonal-phase (β) $NaYF_4$ hosts with C_{3h} symmetry, compared to cubic-phase (α) $NaYF_4$ hosts with the most symmetric O_h symmetry. [14, 29] The crystal structures of both host matrices are exemplarily illustrated in Figure 3. In addition to this influence on the transition probabilities, the site symmetry of the host material also affects the UCL by shifting the energy levels with significant energy shifts in various hosts. [30-32] An efficient host lattice for UCL also requires *low phonon energies*, since high vibrational phonons can enhance the effect of undesired non-radiative multiphonon-relaxation (MPR) to lower lying energy levels. This may be even more important than the effect of low site symmetry of the Ln^{3+} ion on a crystalline lattice, as can be seen by the fact that Ln^{3+} ions in β-$NaYF_4$ are recognized as the most efficient material for UCL, despite its relatively high C_{3h} symmetry compared to other possible hosts.

Therefore hereinafter, this thesis will focus on codoped β-$NaYF_4$ crystals, which for simplicity henceforth will only be denoted as $NaYF_4$. They are typically covered with an organic capping ligand, usually oleic acid (OA), to improve their colloidal stability. A special interest in the literature was dedicated to Yb^{3+}, Er^{3+} codoped crystals with their emission bands around 410, 520, 540, 655, 810 and 850 nm and to Yb^{3+}, Tm^{3+} codoped crystals with their emission bands around 345, 375, 445, 475, 650, 700 and 800 nm, respectively upon 980 nm excitation. Other sensitizer-activator combinations also include *e.g.*, Yb^{3+}, Ho^{3+} codoped UCNP systems with their pronounced emission bands 485, 540, 645 and 1200 nm, which, however, were out of scope for this Ph.D. thesis. [33]

2.2 Ytterbium – erbium codoped crystals

The doping concentration yielding the brightest UCL was previously determined to be 20 % Yb^{3+} and 2 % Er^{3+} for µm-sized powder samples. [34-36] Both ions can replace the trivalent yttrium ions (Y^{3+}) in the crystal lattice, resulting in 78 % Y^{3+}, 20 % Yb^{3+} and 2 % Er^{3+} ions in this example.

2.2.1 Bulk material

The spectral properties of µm-sized UCPs were thoroughly investigated in 1997 and again in more detail for Yb^{3+}, Er^{3+} codoped $NaYF_4$ powder samples very recently by two separate groups. [37-39] Such µm-sized particles will be further also referred as “bulk” particles. The (de)population dynamics of this bulk system can be described by rate equations that are based on the energy level diagram of Yb^{3+}, Er^{3+} codoped crystals, as displayed in panel A of Figure 4, including the ground-state absorption processes of the Yb^{3+} ions ($^2F_{7/2}\rightarrow{}^2F_{5/2}$), four ETU steps, the ($^4G_{11/2}\rightarrow{}^4F_{9/2}$; $^2F_{7/2}\rightarrow{}^2F_{5/2}$) back-energy transfer (BET) process from Er^{3+} to Yb^{3+}, the ($^4I_{13/2}\rightarrow{}^4I_{15/2}$; $^4I_{13/2}\rightarrow{}^4I_{9/2}$) energy transfer process among Er^{3+} ions, and the respective emissive energy transitions. Panel B of Figure 4 shows the corrected emission spectra of the µm-sized $NaYF_4$: 21 % Yb^{3+}, 2 % Er^{3+} powder sample from Ref. [38]. Note that this spectrum is only displayed in the wavelength region between 500 and 860 nm, and therefore does not display the UCL band at 410 nm, which is negligible at this P of 20 $W \cdot cm^{-2}$. Panel C of Figure 4 shows the respective P-dependent UC quantum yield (Φ) values ($\Phi_{UC}(P)$) of the µm-sized $NaYF_4$: 21 % Yb^{3+}, 2 % Er^{3+} powder sample from Ref. [38]. The $\Phi_{UC}(P)$ values represent the quotient

between the number of absorbed (N_{abs}) and emitted (N_{em}) photons from the investigated specimen and are calculated by (eq.) 01.

$$\Phi_{UC} = 100\ \% \cdot N_{em}/N_{abs} \qquad \text{(eq. 01)}$$

The highest obtainable efficiencies of such ~ 20 % Yb^{3+}, ~ 2 % Er^{3+} codoped crystals amount to values around 0.1, 7, 3 and 0.2 %, respectively for the UCL bands around 810, 655, 540 and 410 nm. These values, however, could be different for UCPs that used different precursors for the particle synthesis and can therefore only be considered as a rough estimate. This is highlighted by the fact that a recent study of µm-sized Er^{3+} doped Gd_2O_2S particles reported a factor of four in the difference in UC emission intensity for particles that were synthesized with matching doping concentrations, yet, *e.g.*, used different precursors. [40]

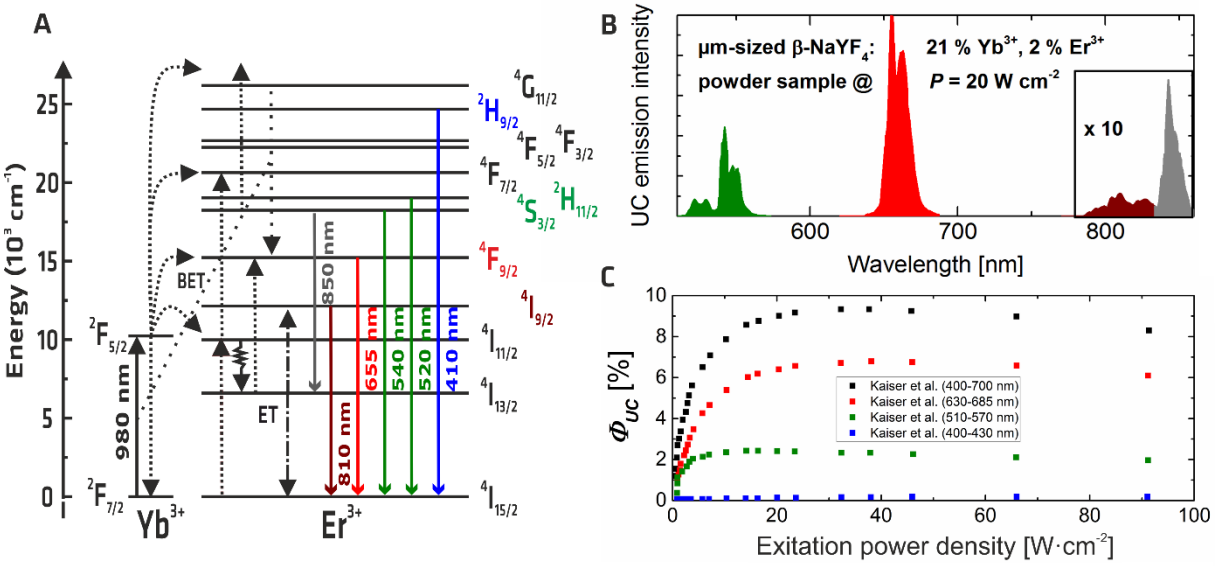

Figure 4: Panel A: Energy level diagram of Yb^{3+}, Er^{3+} codoped UCPs. The short dotted lines represent the ETU steps, the long dotted line the back-energy transfer (BET), the dotted-dashed line an energy transfer process (ET), the zig-zag line a MPR process and the solid lines the respective emissive transitions; **Panel B:** Representative corrected emission spectrum (**panel B**) and *P*-dependent Φ_{UC} values (**panel C**) of the respective visible emission bands of a representative 3 µm-sized $NaYF_4$: 21 % Yb^{3+}, 2 % Er^{3+} bulk powder sample, including the sum of all values, according to Ref. [38]. The NIR UCL bands in panel B were multiplied with a factor of 10 for the convenience of the reader.

The *P*-dependent population behaviour of the various Er^{3+} energy levels is also reflected in the Φ_{UC} values, showing nearly equal values for the green and red emission at low, and a dominant red emission at higher *P*. This is based on the nonlinear optical behaviour of UCPs. For instance,

their emission intensities (I_{em}) are proportional to P to the power of the number of photons that are required to populate the corresponding emissive state (n). For example, the population of the $^4S_{3/2}$ green emitting state is based on the two ($^2F_{5/2}$→$^2F_{7/2}$; $^4I_{15/2}$→$^4I_{11/2}$), ($^2F_{5/2}$→$^2F_{7/2}$; $^4I_{11/2}$→^{4}'$F_{7/2}$) ETU steps, plus non-radiative MPR processes, as depicted in panel A of Figure 4. The emission intensity of the green UCL band at low P is therefore proportional to P^2. The number of absorbed photons that are required for the emission of one high energy photon can be also expressed as the P-dependent slope factors $n(P)$, derived from the respective integral emission, with $I_{em} \propto P^n$ in the low (unsaturated) power regime. They are calculated from energetically neighbouring intensity values $I_{em,i}(\lambda_{em},P_i)$ and $I_{em,j}(\lambda_{em},P_j)$ as follows from (eq.) 02.

$$n(P) = \left[\ln\left(I(x_j)\right) - \ln\left(I(x_i)\right)\right] / \left[\ln\left(P(x_j)\right) - \ln\left(P(x_i)\right)\right] \qquad \text{(eq. 02)}$$

Note that a sinlge linear fit method of the $log(I_{em})$-$log(P^n)$ plot, which is typically used in the literature, can lead to an underestimation of n, since it does not consider the saturation of the population of the lower energy levels with higher P. At high P less photons are required to populate the respective optical transition, resulting in a steady reduction of n, which eventually reaches a constant value, *i.e.*, one for complete saturation. The saturating behaviour of the lower energy levels also explain the constant Φ_{UC} values of the respective UCL bands at high P. The $^4F_{9/2}$ Er^{3+} energy level of the bulk particles, from where the red emission originates, can be populated by different pathways, namely mainly a three- and also partly a two-photon absorption process. The emission intensity of the red UCL band in the non-saturated P regime is therefore proportional to a mixture of a low proportion of P^2 and a much higher one of P^3, explaining the higher Φ_{UC} values of the red UCL band at higher P.

Table 1: Mean luminescence lifetimes of µm-sized $NaYF_4$: 21 % Yb^{3+}, 2 % Er^{3+} UC particles from Ref. [38], determined for DC emission (λ_{ex} = 378 nm for λ_{em} = 410, 540 and 655 nm; λ_{ex} = 940 nm for λ_{em} = 980 nm; λ_{ex} = 978 nm for λ_{em} = 1530 nm) and UC emission (λ_{ex} = 978 nm; 950 µs pulse width), respectively.

	410 nm $^2H_{9/2}$→$^4I_{15/2}$	**540 nm** $^4S_{3/2}$→$^4I_{15/2}$	**655 nm** $^4F_{9/2}$→$^4I_{15/2}$	**980 nm** $^2F_{5/2}$→$^2F_{7/2}$	**1530 nm** $^4I_{13/2}$→$^4I_{15/2}$
UC	420 µs	660 µs	660 µs		
DC	19.5 µs	185 µs	520 µs	2000 µs	8500 µs

Other important spectroscopic features are, *e.g.*, the mean luminescence lifetimes of the respective multi-exponential decays of the emissive Er^{3+} energy levels plus the lifetime of the mono-exponential decay of the $^2F_{5/2}$ excited Yb^{3+} state, shown in Table 1 for the representative $NaYF_4$:

21 % Yb^{3+}, 2 % Er^{3+} 3 µm-sized bulk particles. This table not only includes the UC dynamics, where all Yb^{3+} and Er^{3+} energy levels participate in energy transfer processes, and hence, contribute to the overall lifetimes of the different emissive states, but also the directly excited dynamics of the down-converted (DC) emission of these Ln^{3+} ions, which in the case of Er^{3+} ions only depend on the lifetimes and energy transfer rates of the higher Er^{3+} energy levels. This partly omits contributions from ETU processes involving Yb^{3+}. The direct excitation of the Er^{3+} ions is achieved by an excitation of the higher lying energy levels, which in turn excite the lower energy levels in question through MPR processes.

2.2.2 Effect of particle size

The interest in nm-sized UCPs, *e.g.* for life science applications, encouraged many different researchers to investigate their spectroscopic parameters, revealing that the smaller the UCNPs become, the more their spectroscopic parameters differ from the values of the bulk material, *e.g.* resulting in Φ_{UC} values of 10 nm-sized UCNPs that are several orders of magnitude smaller than the bulk values at the same *P* value. [28, 37, 41-54] Furthermore, the decay kinetics of UCNPs show a shortening of the luminescence decay times of the Er^{3+} and Yb^{3+} energy levels. The various shapes of UCNPs can further complicate this matter, including spherical and rod-shaped structures. [55] The studies from this work in *section 4* thus only focus on spherical structures to exclude a possible influence of the different sites of the hexagonal nanocrystals.

Recent studies of typical Yb^{3+}, Er^{3+} codoped UCNPs started to investigate the origin of the small efficiency values of small UCNPs and subsequently identified the energy transfer from Yb^{3+} ions to solvent molecules, or ligands, or defects on the particle surface as one of the underlying key aspects for the difference between the spectroscopic features of UCNPs and their bulk counterparts. [56] This is especially owed to the fast energy migration among Yb^{3+} ions, which transfer their energy very efficiently among each other, and therefore for small particles also to the particle surface. This finding inspired the research group of Doctor Berry from the University of South Dakota [54] to create a rate equation model that reproduces the decay kinetics and *P*-dependent emission intensities of a $NaYF_4$: 17 % Yb^{3+}, 3 % Er^{3+} core and a $NaYF_4$: 17 % Yb^{3+}, 3 % Er^{3+}@$NaYF_4$ core-shell ensemble sample, only by using the rate constants of a representative bulk sample, and only changing the MPR rate constants for the $^2F_{5/2}$ Yb^{3+}, and $^4I_{11/2}$ and $^4I_{13/2}$ Er^{3+} energy levels. Their model implies that UCNPs with shorter decay times of the $^2F_{5/2}$ Yb^{3+} emission also exhibit shorter decay times of the $^4F_{9/2}$ Er^{3+} emission. However, a

recent study from our group reported that the decay times of the $^4F_{9/2}$ energy level was nearly identical for 23 nm-sized UCNPs in cyclohexane and water, while the mean lifetime (τ_{mean}) of the $^2F_{5/2}$ energy level was clearly smaller in water. [57]

The scaling of the emission intensity with the particle volume is another approach to explain the spectroscopic differences in UCNPs and their bulk counterparts. Here the nanoparticle is divided into a totally quenched dark surface layer and an inner luminescent core. The smaller Φ_{UC} values of smaller UCNPs are therefore explained by the fact that the volume of the dark surface layer still absorbs a fraction of the excitation light, but doesn't contribute to the overall emission of the UCNP. A first study by Zhao *et al.* proposed this model and used it to fit the mean UC decay lifetimes of the green and red UCL bands of 20 to 45 nm-sized $NaYF_4$: 18 % Yb^{3+}, 2 % Er^{3+} UCNPs, dissolved in cyclohexane. [48] They obtained a radius of the dark surface layer of d = 1.5 nm, luminescence decay rates (W) of the dark surface layer of $W_{540\ nm,\ s}$ = 13,040 s^{-1} and $W_{655\ nm,\ s}$ = 9,800 s^{-1} and decay rates of the luminescent core of $W_{540\ nm,\ c}$ = 340 s^{-1} and $W_{655\ nm,\ c}$ = 230 s^{-1}. The subscripts s and c respectively refer to the dark surface layer and particle core. This would account to τ_{mean} of the luminescent core of ≈ 2,900 µs for the green and ≈ 4,350 µs for the red UCL band, which is more than four-times longer than the reported bulk-values in Table 1. Another recent study by Gargas *et al.* utilized this model to fit the particle size dependent emission intensity of single UCNP crystals at a very high P of at least 10^4 $W \cdot cm^{-2}$ between 8 and 200 nm according to (eq.) 03, assuming no optical losses for UCNPs > 100 nm, indicating a radius of the dark surface layer of r_0 = 1.7 nm. [58]

$$\Phi_{UC}(d) = \Phi_0 \cdot V_2(d - d_0)/V_1(d) = \Phi_0 \cdot (d - d_0)^3 \,/\, d^3 \qquad \text{(eq. 03)}$$

Here Φ_0 represents the efficiency value of the luminescent core, d the radius of the investigated UCNP, d_0 the radius of the dark surface region times two ($d_0 = 2 \cdot r_0$), V_2 the volume of the luminescent core, and V_1 the volume of the whole UCNP, respectively. Lastly, the above mentioned study from the research group of Doctor Berry reported an additional very fast decay channel for the $^2F_{5/2}$ Yb^{3+} energy level of 27x56 nm-sized rod-shaped UCNPs, dispersed in toluene. Unable to reproduce the decay kinetics for this sample, they subdivided the nanocrystal in a luminescent core and a dark surface region, this time with a depth of the outer layer of 4.8 nm, and were subsequently also able to reproduce the experimental results for this sample. [54] These different values of the outer dark surface layer underline, that despite all the previous

investigations of the influence of parameters like surface-to-volume ratio and *P* on UCL colour distribution and quenching, the UC mechanism of UCNPs is still not completely understood.

Another feature that apparently depends on the particle size of the UC crystal, and is still debated, is the population behaviour of the $^4F_{9/2}$ energy level from where the 655 nm UCL originates. For example, Jung *et al.* reported that the red emission of 30 nm-sized $NaYF_4$: Yb^{3+}, Er^{3+} UCNPs is dominantly populated by a biphotonic pathway, involving the $^4I_{13/2}$ and $^4F_{9/2}$ energy levels, while other research groups suggested that this emission originates also from triphotonic processes, even for UCNPs that are smaller than 30 nm. [38, 39, 57, 59, 60]

2.2.3 Effect of microenvironment

The efficiency of typical codoped UCNP architectures decreases even further after a transfer from the as-prepared organic medium to aqueous solutions, which are strongly required for the application in biological systems. This originates in particular from the high energy vibrations of the O-H groups between 3,200 and 3,700 cm^{-1}, [61, 62] which *e.g.* favour MPR processes of the $^4I_{11/2} \rightarrow {}^4I_{13/2}$ and $^2H_{11/2}$ / $^4S_{3/2} \rightarrow {}^4F_{9/2}$ transitions of Er^{3+} ions, thereby non-radiatively deactivating the $^4S_{3/2}$ level of Er^{3+}. A consequence of this non-radiative deactivation is a reduction of the population density of the energy level in question, which in turn diminishes the UCL from it. The O-H groups also hamper the population of the higher energy levels indirectly, however, they do not seem to directly affect the population of the $^4F_{9/2}$ level of Er^{3+} with its energy gap of 2,900 cm^{-1} to the neighbouring $^4I_{9/2}$ state. [46] The $^4F_{9/2}$ Er^{3+} energy levels can as a result be populated by different processes in solvents with and without O-H bonds, as depicted in panel A of Figure 5. [57] This is also reflected in the different integrated intensity ratios of the green and red UCL bands (*G/R*) of the representatively chosen 23 nm-sized UCNPs from in water and cyclohexane in the upper image of panel B of Figure 5. The low *G/R* values of the UCNPs in water are, *e.g.*, attributed to an efficient population of the $^4F_{9/2}$ level from the lower $^4I_{13/2}$ level, which is directly fed by MPR processes from the $^4I_{11/2}$ level, and also by MPR processes from the $^2H_{11/2}$ and $^4S_{3/2}$ level. The rising trend of *G/R* with increasing *P* is associated with an increasingly more efficient population of the $^2H_{11/2}$ and $^4S_{3/2}$ level, while the fact that the *G/R* of both samples at high *P* both decrease and converge to a value of 0.4 respectively indicates similar relaxation dynamics of these UCL bands at high *P*, independent of the respective microenvironment.

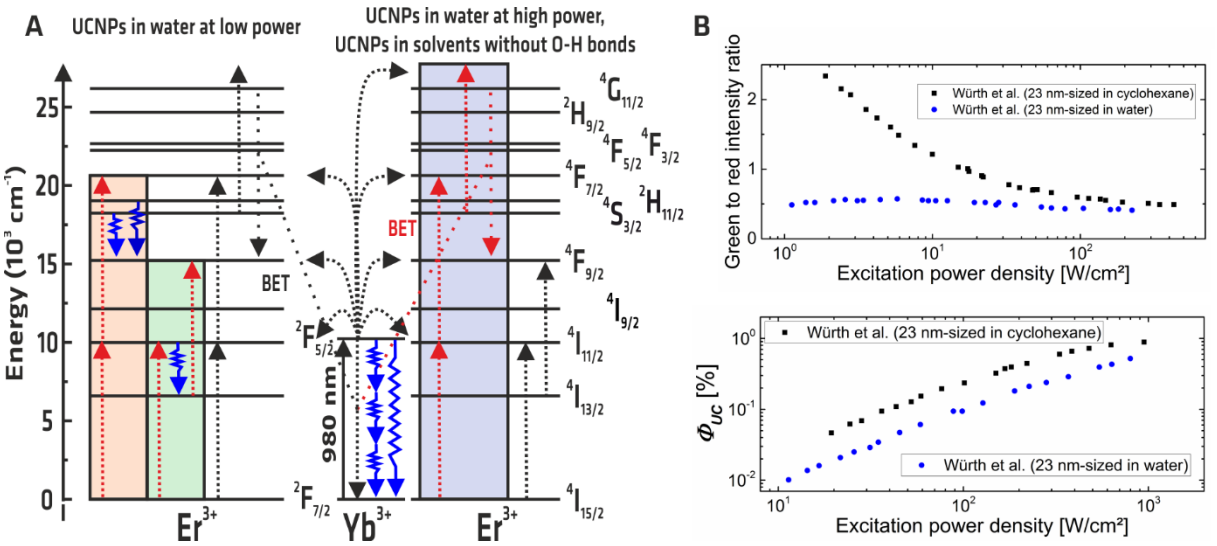

Figure 5: **Panel A:** Energy level diagram of Yb^{3+}, Er^{3+} codoped UC particles, highlighting the dominant population pathways of the $^4F_{9/2}$ Er^{3+} energy level in water at low (left) and high *P* (right). The pathways on the right closely match with the photophysics of UCNPs in solvents without O-H bonds. Blue arrows represent increased MPR due to interactions with O-H vibrations, according to Ref. [57]. **Panel B:** *P*-dependent integrated intensity ratio of the green and red UCL emission band (upper image) and Φ_{UC} values (lower image) of 23 nm-sized UCNPs, respectively dispersed in cyclohexane with OA and water with citrate as a capping ligand, according to Ref. [57]. MPR: multi-phonon relaxation; BET: back-energy transfer

Molecules which contain chemical moieties with high energy vibrations like O-H groups are also known to quench particularly the $^2F_{5/2}$ energy level of Yb^{3+}, which feed the UCL of the Er^{3+} ions via ETU in UCNPs, resulting in lower intensities of similar sized UCNPs in water. [54, 56, 63, 64] As depicted in the lower image of Figure 5, panel B, this leads to a reduction of the Φ_{UC} values by a constant factor of around three at low and of 2.5 at high *P*, compared to cyclohexane. The suppression of the emission intensity via water molecules was even recently utilized for the sensitive probing of the water content of organic solvents. [65] The study from Ref. [57] also investigated the spectroscopic properties of these UCNPs in two other solvents without O-H bonds, using different surface ligands, and with one other surface ligand in water, reporting no significant differences of the spectroscopic properties, respectively in solvents with and without O-H bonds. Furthermore, the results from this study suggest that the typically used doping concentrations may have to be optimized for applications in water, and possibly also for different UCNP sizes.

2.2.4 Core-shell approach

The growth of an inert protective shell is a common approach to partly reduce the optical losses in UCNPs, resulting in improved Φ_{UC} values, compared to similar sized core-only particles. [39, 49, 52] For example, an early study reported that a 30 nm-sized core-shell sample showed nearly the same Φ_{UC} value as a 100 nm-sized sample at an exemplarily P of 150 W·cm^{-2}. [41] Another exemplarily study of 24 nm-sized $NaYF_4$: 33 % Yb^{3+}, 5 % Er^{3+} UCNPs has shown, that the Φ_{UC} values further improve for thicker shell thickness up to around 6 nm. [63] The mechanism behind this improvement can be described in a Förster-type model. In this case, the energy donors are the Er^{3+} and Yb^{3+} ions at the UCNP surface that transfer their energy through the inactive shell to a thin plane-layer of oleate capping ligands that are bound to the outside of the inert shell. [54]

Energy transfer processes to surface-bound energy harvesting, analyte responsive or therapeutically active molecules, [24, 25] however require a close neighbourhood of Ln^{3+} donors and organic acceptors. In this case, core-only nanostructures or core-shell UCNPs with very thin shells are mandatory, making the approach of thick protective shells unfavourable. Furthermore, and in contrast to classical donor-acceptor pairs, UCNPs contain many emitting Ln^{3+} ions together with numerous acceptor dye molecules at different distances to each other. This among other things motivated us and our cooperation partners from Regensburg to perform a joint study of the Förster resonance energy transfer (FRET) process from $NaYF_4$: 20 % Yb^{3+}, 2 % Er^{3+} UCNPs with varying particle diameters between 10 and 43 nm, respectively to two surface-bound model acceptor dyes. [66] The results clearly show the highest FRET efficiency for a mean diameter in the range of 20-25 nm and lower efficiencies for both smaller and bigger UCNPs, suggesting enhanced FRET efficiencies for UCNP-based FRET platforms with this particle size.

2.2.5 Nanostructure

Another approach to address the low efficiency values of UCNPs is the development of versatile core-shell nanostructures with separated sensitizer and activator ions. [33, 67] One example is shown in an exemplarily joint study with cooperation partners from Singapore that investigated the UCL intensity, decay kinetics and FRET efficiencies of sample batches with similar particle concentrations. The focus of this study was a comparison between nanostructures that confined

emitting activator ions in the core and absorbing sensitizer ions in the shell (denoted as Er@Yb), nanostructures that confined sensitizer ions in the core and activator ions in the shell (denoted as Yb@Er), Yb@Er nanostructures with an additional Yb^{3+} codoping concentration in the shell (denoted as Yb@Er,Yb) and lastly, typical codoped core-only nanostructures (denoted as Yb,Er). A schematic illustration of the three new UCNP nanostructures is shown in Figure 6. The respective doping concentrations were 20 % Yb^{3+} and 2 % Er^{3+}. The results show the highest brightness (B) values for UCNP structures with an Yb^{3+} sensitizer-rich core and an Er^{3+}, Yb^{3+} codoped shell. B scales the Φ_{UC} values with the total number of sensitizer ions (N_{Yb}) in the particle and is therefore is especially important for the comparison of the performance of UCNPs with different doping concentrations. It is therefore a quantitative measure of the relative number of emitted photons per particle and follows from (eq.) 04. [33]

$$B = N_{em}/N_{abs} \cdot N_{Yb} \qquad \text{(eq. 04)}$$

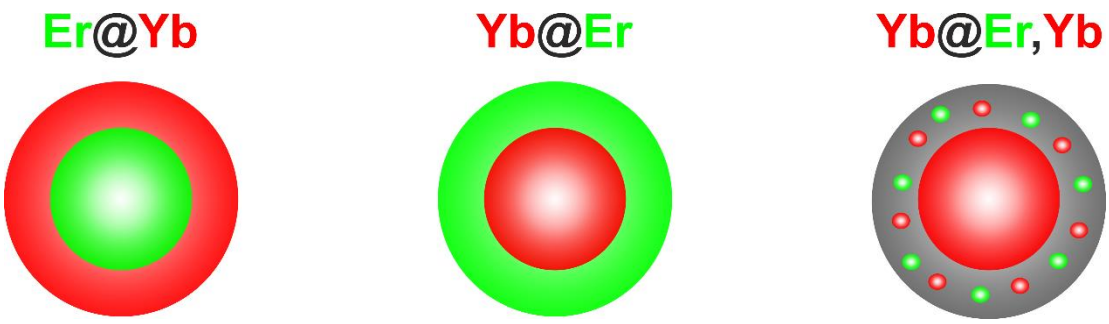

Figure 6: Schematic representation of the Er@Yb, Yb@Er and Yb@Er,Yb UCNP nanostructures.

However, as stated in *section 2.2.3*, it is not clear if the same doping concentrations yield the highest efficiency values both for micro- and nanometer-sized UCPs. This question is especially encouraged by the competing processes in the nanocrystals, such as the energy transfer from Yb^{3+} to Er^{3+}, CR, or ET processes between Er^{3+} ions and also surface quenching-dependent MPR processes. The doping concentrations, or interionic distances, yielding the highest Φ_{UC} values can therefore additionally also depend on the respective excitation power. The highest Φ_{UC} values of $NaYF_4$: Er^{3+} doped microcrystalline powder samples with different interionic Er^{3+}-Er^{3+} distances (λ_{ex} = 1,523 nm and λ_{em} < 1,100 nm) were, *e.g.*, not reported at the same P value. Here the highest values were respectively reported for doping concentrations of around 19 and 30 % for P values of 0.04 and 0.4 $W \cdot cm^{-2}$. [51]

2.3 Ytterbium – thulium codoped crystals

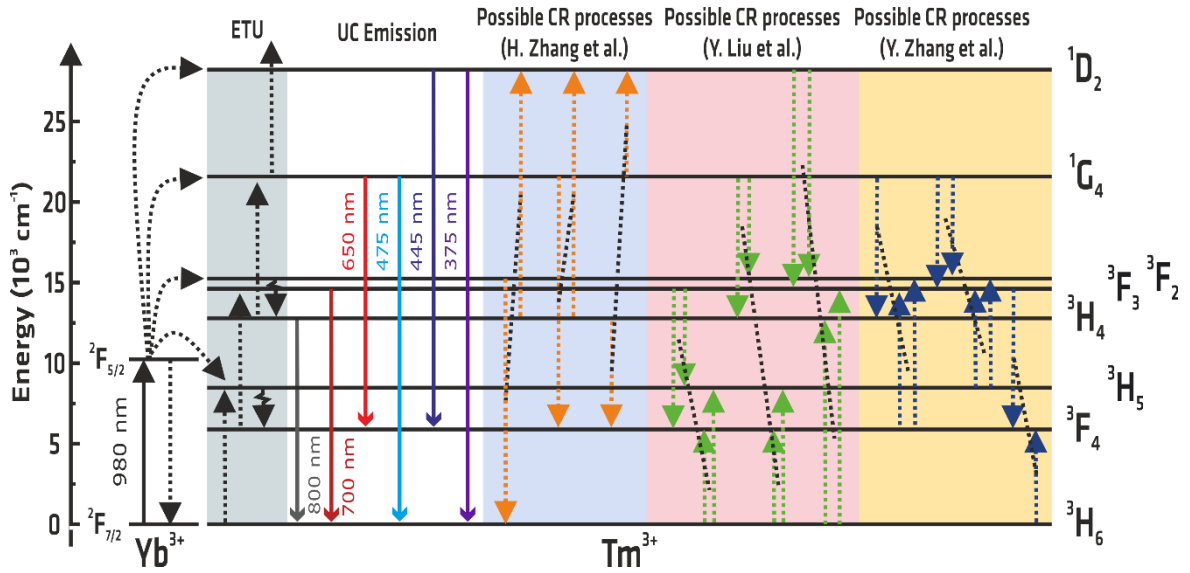

Figure 7: Energy level diagram of Yb^{3+}, Tm^{3+} codoped UC particles. The black short dotted lines represent the ETU steps, the orange short dotted lines the CR processes and the zig-zag lines MPR processes. The possible CR processes according to H. Zhang *et al.* (Ref. [68]), Y. Liu *et al.* (Ref. [69]) and Y. Zhang *et al.* (Ref. [70]) are respectively highlighted with blue, red and yellow background colours. ETU: energy transfer upconversion; CR: cross-relaxation; MPR: multiphonon-relaxation

The doping concentrations yielding the highest efficiency values of Yb^{3+}, Tm^{3+} codoped nanocrystals are even harder to predict, since their particle size- and *P*-dependent (de)population behaviours are less understood than the ones of Yb^{3+}, Er^{3+} codoped UCNPs. This is especially highlighted by the many possible CR processes among the Tm^{3+} ions that can accompany the ETU processes from Yb^{3+} to Tm^{3+}, as shown in Figure 7. [68, 69, 71, 72] Figure 7 also includes the energy transitions of the UC emission bands at 800, 700, 650, 475, 445 and 375 nm, respectively. The next two sub-chapters will now respectively elaborate the proposed (de)population pathways of the lower $^3H_4$ and the higher $^1G_4$ and $^1D_2$ Tm^{3+} energy levels.

2.3.1 (De)population pathways of lower energy levels

At low doping concentrations, where Tm^{3+} CR processes are negligible, the strong NIR emission at 800 nm is widely believed to be populated by a first phonon-assisted ($^2F_{5/2}$→$^2F_{7/2}$; $^3H_6$→$^3H_5$) ETU process, followed by the $^3H_5$→$^3F_4$ MPR, the ($^2F_{5/2}$→$^2F_{7/2}$; $^3F_4$→$^3F_3$) ETU and the $^3F_3$→$^3H_4$ MPR processes. The research group of Professor Andersson-Engels from the Lund University simplified the population pathways of this two-photonic UCL band (see also panel A of Figure 8) and subsequently derived (eq.) 05 to simulate its *P*-dependent Φ_{UC} values. Here

$P_{balance}$ represents the so-called balancing power density and $\Phi_{UC\text{-}sat}$ the saturated Φ_{UC} value of the corresponding two-photon UC emission at high P. [73] Note that this model is also valid for the two-photon UCL of the $^2H_{11/2} \rightarrow {}^4I_{15/2}$ and $^4S_{3/2} \rightarrow {}^4I_{15/2}$ transitions of Yb^{3+}, Er^{3+} codoped crystals.

$$\Phi_{UC}(P) = \Phi_{UC-sat}\,(P/P_{balance}) / (1 + (P/P_{balance})) \qquad \text{(eq. 05)}$$

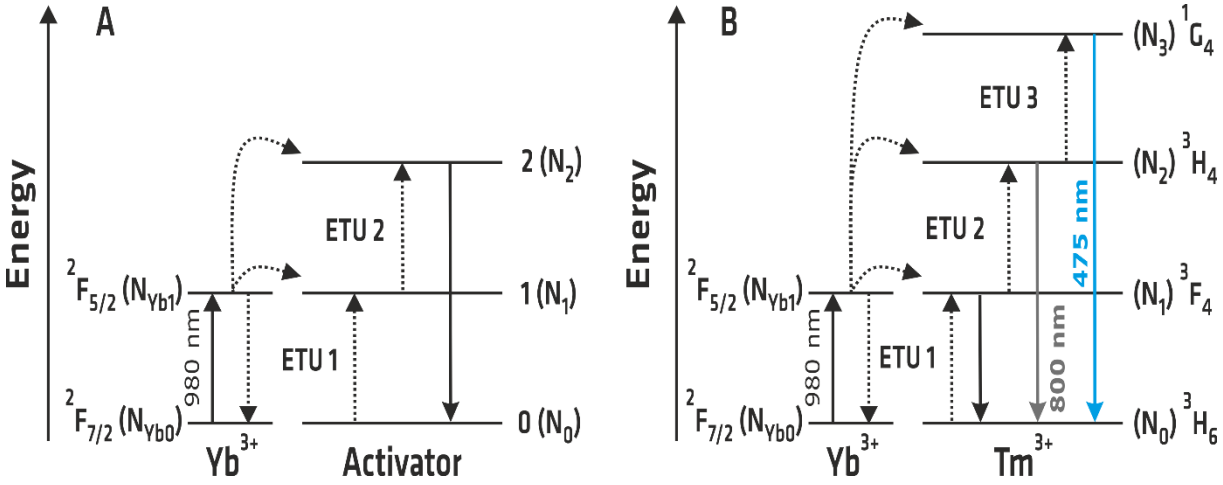

Figure 8: Schematic energy level diagrams that were respectively used to derive (eq.) 05 [73] (**panel A**) and (eq.) 06 [72] (**panel B**).

Another recent study showed, that the ratio between the two-photonic UC band at 800 nm and the three-photonic UC band at 475 nm increases by a factor of over 24, while increasing the Tm^{3+} concentration of 18 nm-sized $NaYF_4$: 20 % Yb^{3+} particles from 0.3 to 4.0 %, resulting in a quasi-monochromatic UCL at 800 nm. [72] They then proposed a rate equation model that is based on a three-photonic absorption process, as shown in panel B of Figure 8, deducted (eq.) 06 and were subsequently able to reproduce the ratio between those two UCL bands with the ratio of τ_{mean} of the $^2F_{5/2}$ Yb^{3+} ($\tau_{980\ nm}$) and $^1G_4$ Tm^{3+} ($\tau_{475\ nm}$) energy levels.

$$I_{475\ nm} / I_{800\ nm} \propto \tau_{980\ nm}\,\tau_{475\ nm} \qquad \text{(eq. 06)}$$

2.3.2 (De)population pathways of higher energy levels

The population pathways of the higher $^1G_4$ and $^1D_2$ Tm^{3+} energy levels are typically assumed to be based on three and four ETU steps, respectively. The research group of Professor Valiente from the University of Cantabria recently used this assumption and created an extensive rate

equation model to reproduce the decay kinetics and emission intensities of a 1-3 µm-sized $NaYF_4$: 25 % Yb^{3+}, 0.3 % Tm^{3+} powder sample up to the $^1D_2$ Tm^{3+} energy level. [74] They were even able to reproduce τ_{mean} of the $^3H_4$ Tm^{3+} energy level for x_{Yb} % Yb^{3+}, 0.3 % Tm^{3+} (x_{Yb} = 0.1, 1, 10, 25, 50 and 99.7) codoped samples by simulating the crystal lattice and calculating the respective concentration dependent energy transfer rates. This model consequently predicts that the ratio of the emission intensities of the UCL bands originating from the $^1D_2$ and $^1G_4$ Tm^{3+} energy levels increases with increasing P and subsequently saturates at higher P values.

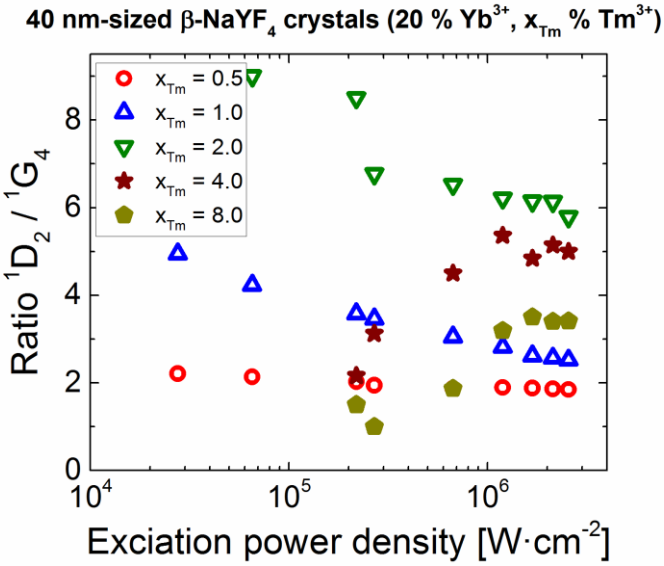

Figure 9: Integrated intensity ratios of the $^1D_2$ to $^1G_4$ classes over P of 40 nm-sized $NaYF_4$: 20 % Yb^{3+}, x_{Tm} % Tm^{3+} (x_{Tm} = 0.5, 1.0, 2.0, 4.0 and 8.0) doped UCNPs, dispersed in cyclohexane, calculated from the $^1D_2/^3H_4$ and $^1G_4/^3H_4$ ratios from Ref. [75].

However, some studies already reported results that are in conflict with this model for Yb^{3+}, Tm^{3+} codoped $NaYF_4$ nanocrystals. [68, 75] For instance, Figure 9 shows the ratio of the sum of the integrated UCL bands originating from the $^1D_2$ Tm^{3+} energy level (centred at 455, 514, 744 and 782 nm) over those originating from the $^1G_4$ Tm^{3+} energy level (centred at 475 and 660 nm) of 40 nm-sized $NaYF_4$: 20 % Yb^{3+}, x_{Tm} % Tm^{3+} (x_{Tm} = 0.5, 1.0, 2.0, 4.0 and 8.0) crystals that are dispersed in cyclohexane. [68] Instead of showing increasing or constant values over P, the ratio from these two energy levels slightly decreases for their lowest x_{Tm} of 0.5. This trend is even more pronounced for the samples with higher x_{Tm} values. This implies that the ETU processes are accompanied by other processes in the population of the higher Tm^{3+} energy levels. Other studies even state that the $^1D_2$ Tm^{3+} is solely populated by CR processes, such as the

pathways ($^3F_2$→$^3H_6$; $^3H_4$→$^1D_2$), ($^1G_4$→$^3F_4$; $^3H_4$→$^1D_2$) and ($^1G_4$→$^1D_2$; $^3H_4$→$^3F_4$), as depicted with the blue background in Figure 7. This is especially motivated by the relatively big energy mismatch between the $^1G_4$→$^1D_2$ and $^2F_{5/2}$→$^2F_{7/2}$ transitions of the ETU process.

Another study proposed even different CR processes to simulate their results. [69] They studied a series of ten 40 nm-sized $NaYF_4$: 20 % Yb^{3+}, x_{Tm} % Tm^{3+} codoped nanocrystal samples with incremental x_{Tm} values from 0.5 to 8.0, excited them with a dual-laser confocal microscope at 980 and 808 nm and subsequently triggered an amplified stimulated emission to deplete the $^3H_4$ Tm^{3+} energy level through an established population inversion relative to the ground level. This lead to an optical inhibition of the UC pathway that generates blue UCL. They were subsequently able to reproduce their experimental results using a simplified rate equation model, based on energy pumping at 980 and 808 nm, four ETU steps and three CR processes. Instead of using all Tm^{3+} energy levels, this model respectively only uses one energy level for the $^3F_4$; $^3H_5$ and $^3H_4$; $^3F_3$; $^3F_2$ Tm^{3+} energy levels, reducing the six CR pathways that are highlighted with a light red background in Figure 7, to only three CR pathways. Lastly, a very recent study from a Chinese research group investigated the spectroscopic properties of *i.a.* $Gd_2(WO_4)_3$ 10 % Yb^{3+}, x_{Tm} % Tm^{3+} (x_{Tm} = 0.1, 0.3, 0.5, 1.0, 1.5, 2.0, 2.5 and 3.0) particles with diameters around hundreds of nanometers. [70] Their results implicate that the Tm^{3+} energy levels of these UCPs are populated by a mixture of ETU and three different CR processes. The corresponding proposed ($^1G_4$→$^3H_4$; $^3F_4$→$^3F_{2/3}$), ($^1G_4$→$^3F_{2/3}$; $^3H_5$→$^3F_{2/3}$) and ($^3H_4$→$^3F_4$; $^3H_6$→$^3F_4$) CR processes are highlighted in Figure 7 with a yellow background.

These results highlight the fact that a single compelling model that highlights all main processes of the (de)population pathways of Yb^{3+}, Tm^{3+} codoped crystals is still lacking. The many proposed CR processes even suggest, that different Tm^{3+} could be favoured for different codoping concentrations, resulting in different optimal doping concentrations that yield the highest UC efficiency for the different Tm^{3+} UC emission bands.

2.4 Dissolution and possible toxicity of UCNPs

Studies about the potential leakage of Ln^{3+} or fluoride anions from fluoride-based UNCPs in water or in physiological media previously raised the concern about the possible toxicity of UCNPs. [76-79] Such studies highlighted that, although the photochemical and thermal stability and chemical inertness of, *e.g.*, Ln^{3+} based µm-sized particles is typically claimed as very high,

based on the relatively low solubility rate of lanthanide fluorides in water, this could differ for their nanoparticle counterparts, due to their larger surface-to-volume ratio (*SA/Vol*). [80] Their solubility can also be affected by pH and the presence of other chemical species that can form complexes with the Ln^{3+} ions, thereby favouring a dissolution process. [81, 82] Previous studies from a group in Slovenia, *e.g.*, suggested the partial dissolution of cubic $NaYF_4$, LaF_3 and GdF_3 UCNPs in water at room temperature (*RT*). [83, 84] The released fluoride ions from these UCNPs, *e.g.*, can modulate intracellular redox homeostasis, induce oxidative stress, alter gene expressions, and cause apoptosis when they appear in a high dose and excel an adequate intake. [85] These preliminary studies, however, payed no intention in the identification of an easy accessible parameter that can be used to screen the stability of UCNPs.

3 Experimental and characterization methods

3.1 Structural and chemical analysis

The studied UCNPs were synthesized and structurally and chemically analysed by the respective cooperation partners. They dedicated special attention to the examination of the crystal phase of the host material and the physical dimensions of the particles, since they can heavily influence the spectroscopic properties of UCNPs, as stated in *sections 2.1.2*. Since all samples were dispersed in a solvent for the spectroscopic analysis, they also investigated the colloidal stability. They therefore performed the following measurements for most of the samples: X-ray diffraction pattern analysis (XRD) to determine the crystal phase, diffraction light scattering (DLS) measurements to ensure their colloidal stability and monodispersity, transmission electron microscopy (TEM) to determine the respective physical dimensions and inductively coupled plasma optical emission spectroscopy (ICP-OES) measurements to ensure that the synthesis yielded the aimed Ln^{3+} doping concentrations. The respective results are shortly given in the subsections "structural and chemical analysis" of the four studies.

3.2 Spectroscopic analysis

The Φ values of traditional fluorophores are typically obtained by a measurement of the absorption and emission spectra of the investigated specimen with commercial spectrometers and a subsequent comparison of these values with a certified reference sample that was measured under the same conditions. This relative measurement procedure allows to easily measure Φ values of non-scattering fluorophores, however, it is not feasible for UCNPs as there are no existing suitable reference materials that can simultaneously cover the same absorption and emission bands as UCNPs and as a better understanding of the deactivation channels of UCNPs also requires the investigation of scattering powder samples. The results from this thesis were therefore obtained by the spectrally resolved number of absorbed and emitted photons using a custom-built integrating sphere setup. The decay kinetics were measured with commercial spectrometers. Both are described in the sections below.

3.2.1 Steady-state measurements

The nonlinear emission behaviour of UCNPs imposes a number of stringent requirements on the excitation and detection channel of the spectroscopic setup. This includes a well-defined

beam profile and a high wavelength and intensity stability at an excitation wavelength that matches the narrow Yb^{3+} absorption band around 980 nm. It furthermore should be possible to vary *P* from the region where the emission behaviour of UCPs show saturation (*e.g.* ≈ 25 $W \cdot cm^{-2}$ for a µm-sized $NaYF_4$: 21 % Yb^{3+}, 2 % Er^{3+} powder sample, ≈ 1,000 $W \cdot cm^{-2}$ for 25 nm-sized $NaYF_4$: 17 % Yb^{3+}, 3 % Er^{3+} particles in toluene and ≈ 20 $W \cdot cm^{-2}$ for 33 nm-sized $NaYF_4$: 25 % Yb^{3+}, 0.3 % Tm^{3+} particles in a non-polar solvent) [38, 73] to a *P* region at least one order of magnitude below to get a better understanding of the population behaviour of UCPs under various conditions. The detection channel must be able to identify the number of absorbed and emitted photons of scattering (*e.g.* powder samples) and non-scattering (*e.g.* nanoparticles in a solvent) samples in a wavelength region between 330 and 1,000 nm under constant measurement conditions. This is especially challenging since the excitation intensity is several orders of magnitude higher than the upconverted emission intensity, based on the typically low absorption values of the UCNPs that are required to avoid an attenuation of the excitation beam in the sample containing cuvette and luminescence efficiencies below 0.01 % of, *e.g.*, small nanocrystals. [41]

Custom built spectrometer with integrating sphere

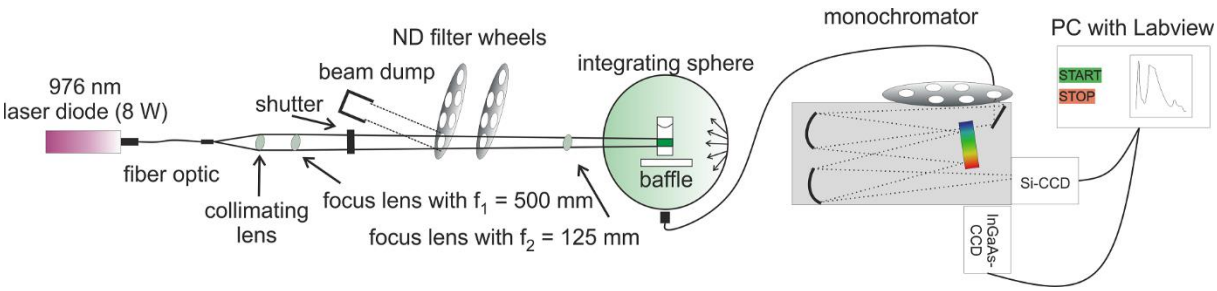

Figure 10: Schematic presentation of the custom-built integrating sphere setup. The setup could be either operated with the focus length with a focal distance of 500 mm, or with the lens with a focal distance of 125 mm.

An accordingly designed first setup that fulfils these requirements was custom-built and recently published by Martin Kaiser, dedicating special attention to its excitation channel. [38] This setup allowed to excite UCPs with an average *P* between 0.25 and 410 $W \cdot cm^{-2}$ with a top-hat beam profile, or 2.5 and 3,400 $W \cdot cm^{-2}$ with a Gaussian beam profile, respectively while using a focus lens with focal distances of 500 or 125 mm. This setup was rebuilt after the laser diode had to be exchanged and furthermore, the detection channel was extended with an additional indium-gallium-arsenide (InGaAs) charge-coupled device (CCD) and a different integrating sphere (diameter of *ca.* 11 cm, coated with high reflectivity hydrophobic Spectralon –

99 % from 400 to 1,500 nm; equipped with six ports) was used to now also cover the NIR emission of UCPs up to 1,550 nm. The new setup with its main parts is displayed in Figure 10. Its excitation channel consists of a 976 nm laser diode, collimating and focusing optics, a shutter that can block the excitation light, filter wheels with neutral density (ND) filters, used to attenuate the excitation light without affecting its stability, and a beam dump that collects the reflected light from the filter wheels. The detection channel consist of the integrating sphere with a sample holder placed inside, baffles that protect the optical fibre from direct illumination, the attached fibre optic, the monochromator (Andor 303i) with a filter wheel at the front and the two Peltier cooled CCDs (T = 188 K; silicon (Si)-CCD: iDus Si DU4230_DD, Andor Technology PLC; CCD line, 1024×256 pixel, pixel sizes of 26×26 µm; InGaAs-CCD: iDus InGaAs DU491A, Andor Technology PLC; CCD line, 1024×1 pixel, pixel sizes of 25×500 µm). The whole system was operated with an also custom-built software that was programmed with "LabView".

The details of the subsequent calibration, performed after a reported protocol, [38, 86, 87] are given in the following sub-chapters. This includes the investigation of the beam profile and stability of the laser for the excitation channel and the wavelength accuracy, linear range of detection and the spectral responsivity for the detection channel of the setup. This extensive calibration subsequently ensures a precise measurement of the narrow emission bands of UCPs under various conditions. However, no measurements were performed with the InGaAs-CCD in this work and therefore its calibration is not included in the following sub-chapters. Furthermore, no measurements were performed with the focus lens with a focal distance of 125 mm in this work neither and therefore its details are not included in the following sub-chapters neither.

Excitation channel

Stability of the excitation source. The fluctuation of the excitation power is shown in Figure 11 over a representative time span of around two hours, revealing an overall very good stability of the (976 ± 1) nm laser diode (RLTMDL-N-976nm-8W, with fixed output power supply PSU-H-FDA) with a standard deviation of ± 0.2 %. This is especially important as one complete measurement cycle can take up to two hours (see also upcoming section *measurement procedure*).

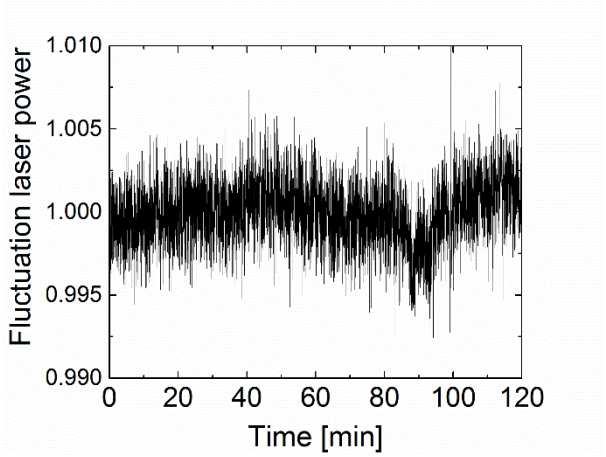

Figure 11: Stability of the output power from the laser diode that was measured over a representative time span of two hours.

Beam profile. The first step for the determination of the beam profile was to mark the spots where the 10 mm long cuvette would be placed in the integrating sphere, followed by the measurement of the profile of the excitation beam with a beam profiler (Newport LBP2) in steps of 1 mm in between the space where the front and the rear position of the cuvette would be. The results are displayed in Figure 12 for the front, centre and rear position of the cuvette, showing only small differences over the 10 mm path length of the so-called top-hat beam profile. The radius of the excitation beam was subsequently determined to be (0.66 ± 0.03) mm and the output power of the laser was determined with a calibrated power meter to be (5.85 ± 0.01) W at the position of the sample, resulting in maximum average P of around 425 W·cm^{-2} in the cuvette.

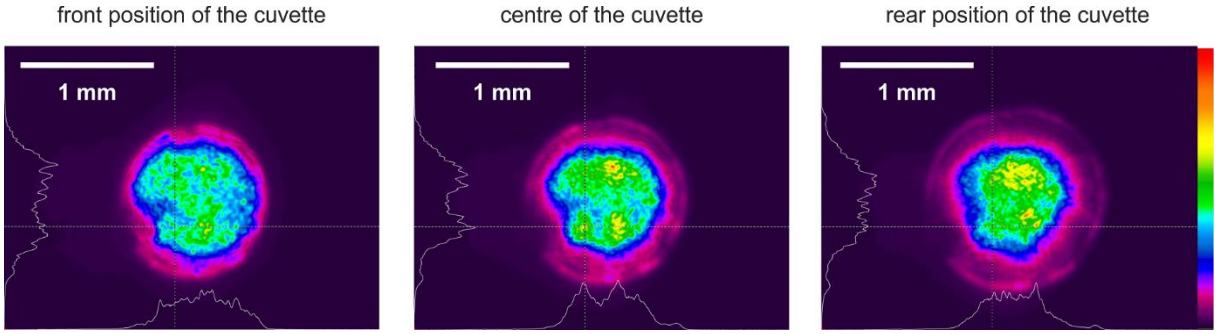

Figure 12: Intensity cross-section of the 976 nm laser that is focused with a 500 mm lens at the front, centre and rear position of the cuvette. The inset represents the scale of 1 mm and the colour scale on the right represents the intensity of the respective pixel in arbitrary units.

Detection channel

The filter wheel in front of the monochromator was equipped with one empty slot, here termed "Filter 1", and five different wavelength responsive bandpass filters that were respectively used to protect the detector from overexposure by light and to reduce stray light from the grating in the monochromator. One of those filters, here termed "Filter 5", is an absorptive ND filter that is used to attenuate the laser light with a factor of around 5,600. Furthermore, the detector only simultaneously covers a wavelength range of around 130 nm for a given position, which is why the whole measurement procedure was subdivided in six overlapping parts, namely between (329-469), (450-585), (571-707), (692-825), (813-944) and (935-1,062) nm. The overlap of two respective neighbouring channels was chosen to be small enough to allow a full spectral measurement with the smallest possible number of steps and yet to be still large enough to allow to smoothly glue and interpolate these channels to one joint emission and excitation spectrum between 330 and 1,000 nm.

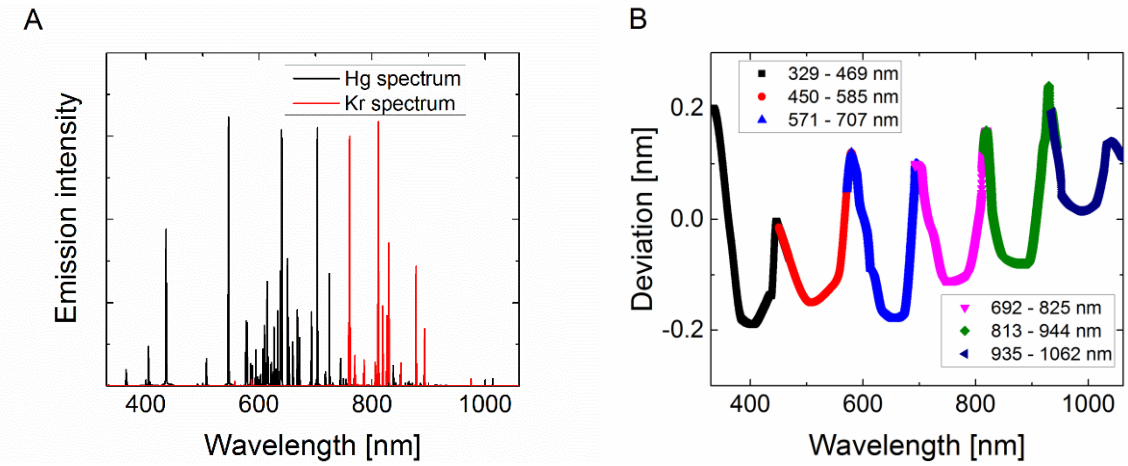

Figure 13: Panel A: Respective emission spectrum of a standardized mercury/argon (Hg) and krypton (Kr) discharge lamp, provided by the NIST. **Panel B:** Extrapolated spectral deviations from the peak position taken form the NIST Physical Reference Data for each of the respective measurement channels.

Wavelength accuracy. The wavelength accuracy of the detection channel was investigated with conventional low pressure mercury/neon (L.O.T. Oriel, Pen Ray Lamp, LSP034) and krypton (L.O.T. Oriel, Pen Ray Lamp, LSP031) discharge lamps for all six measurement channels. This involved the calculation of the deviation of the peak positions that were reported by the National Institute of Standards and Technology (NIST), shown in panel A of Figure 13, from the measured peak positions. The subsequent extrapolation of the results was used for the creation of the

respective correction files with a resolution of around 0.15 nm and is shown in panel B of Figure 13.

Linearity of detector sensitivity. A large linear range of the detector sensitivity is of special importance for the determination of the emission behaviour of UCPs since their emission intensity can vary over several orders of magnitude, depending on various parameters, such as *e.g.* particle size, microenvironment, host matrix and doping concentration. The linear range of a similar Si-CCD, as the one used in this setup, was previously obtained to be over more than two orders of magnitude, underlying a large dynamic range of the detector. [86] The dynamic range was further enhanced by the use of different exposure times for the respective measurement channels by more than three orders of magnitude. The nonlinear behaviour of the integrated emission intensity versus the exposure time of the Si-CCD was accounted for with an additional correction that was interpolated from the data that is displayed in Figure 14.

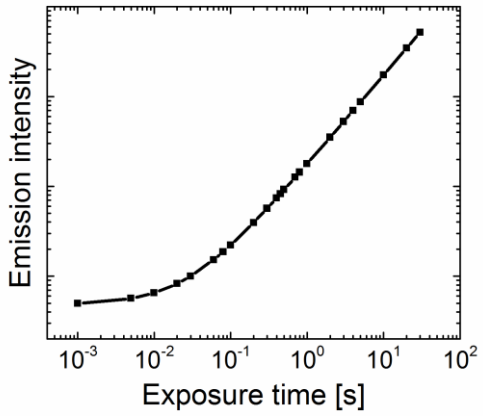

Figure 14: Normalized emission intensity of the detection channel versus the exposure time.

Spectral responsivity. The spectral responsivity $s(\lambda_{em})$ of the integrating sphere - fibre optic - filter wheel – monochromator - CCD ensemble was determined with a calibrated quartz halogen lamp (Gigahertz-Optik GmbH; PTB-calibrated; termed SDS) for all detection bandpass filters that were placed in the filter wheel in front of the monochromator for the respectively selected measurement channels. Additional wavelength filters were used for the determination of the spectral responsivity for the (450-585), (571-707) nm channels to eliminate any stray light from higher wavelengths. However, this was not feasible for the (329-469) nm channel. Its spectral responsivity was calibrated with the spectral emission standard F002. [88] The excitation of the reference dye F002 was performed with an additional previously described excitation channel,

consisting of a 450 W xenon lamp, coupled to a single monochromator, a reference detector and the respective focussing optics. [86] The results were then validated with the certified spectral emission standards F003, F004 and F005 and the reported emission spectra from the dyes Itrybe and IR140, respectively dissolved in ethanol and dimethyl sulfoxide.

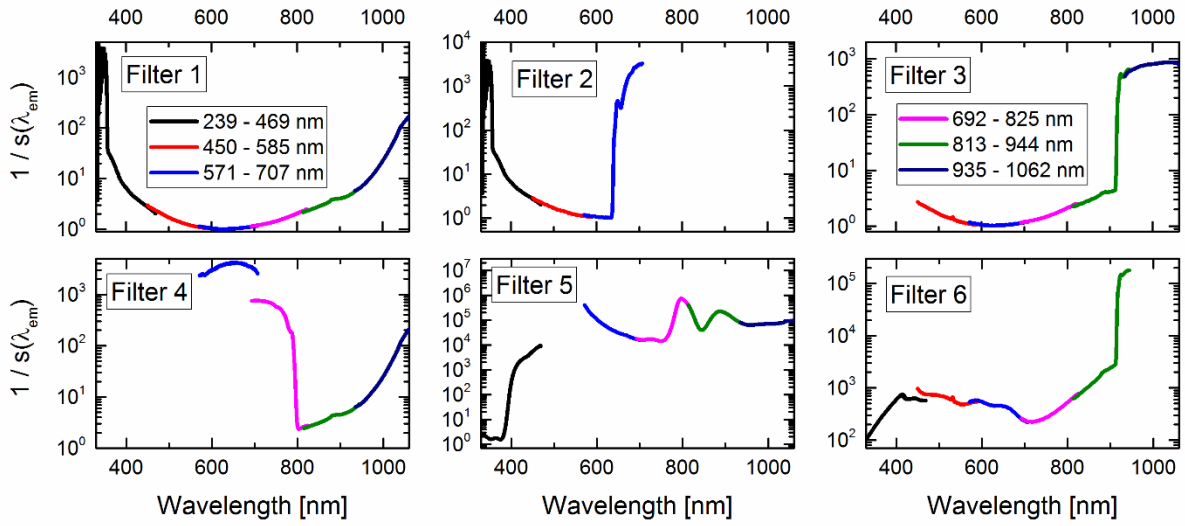

Figure 15: Inverse spectral responsivity $s(\lambda_{em})$ (equalling the emission correction curve) of the detection channel for all filters that were placed in the filter wheel in front of the monochromator.

As $s(\lambda_{em})$ is expressed in radiometric units, so is the wavelength dependent intensity of the resulting spectra. Hence, the detected intensity is proportional to the energy of the detected photons. The respective spectra were therefore then multiplied by the factor $h \cdot c_0 / \lambda_{em}$. Here h is the Planck constant and c_0 is the speed of light in vacuum. The inverse spectral responsivities, as displayed in Figure 15, were then multiplied to the measured intensity spectra to render them traceable to the spectral photon radiance photonic units and thus to the number of detected photons.

Measurement procedure

A typical measurement cycle started with the placement of a 10 mm wide, 10 mm long and 30 mm high cuvette that is filled with the sample material (or the pure solvent in which the UCPs are dispersed - further referred as “blank”) in the middle of the integrating sphere. The precise positioning of the sample / blank inside the integrating sphere was then ensured with an additional small helium-neon laser to exclude possible effects from different positions of the blank

/ sample and thereafter different reflecting behaviour from both cuvettes. After this, the exposure time was adjusted for the respective excitation power density for all measurement channels, followed by the measurement of the dark counts of the detector. Finally, the measurement was started, one time while going from low to high P and another time in reverse. This also includes a possible delay time between two measurements of 0 to 120 s to exclude heating effects within the sample.

Photoluminescence quantum yield

The Φ_{UC} values were calculated from the measured and dark corrected emission and excitation spectra of the investigated specimen and the respective blank material according to Figure 16. One example is shown in. N_{abs} is represented by the integrated difference of the blank and sample material between 962 and 982 nm (orange region in panel A of Figure 16) and N_{em} is represented by the integrated difference of the sample and blank material between 330 and 860 nm (orange region in panel B of Figure 16).

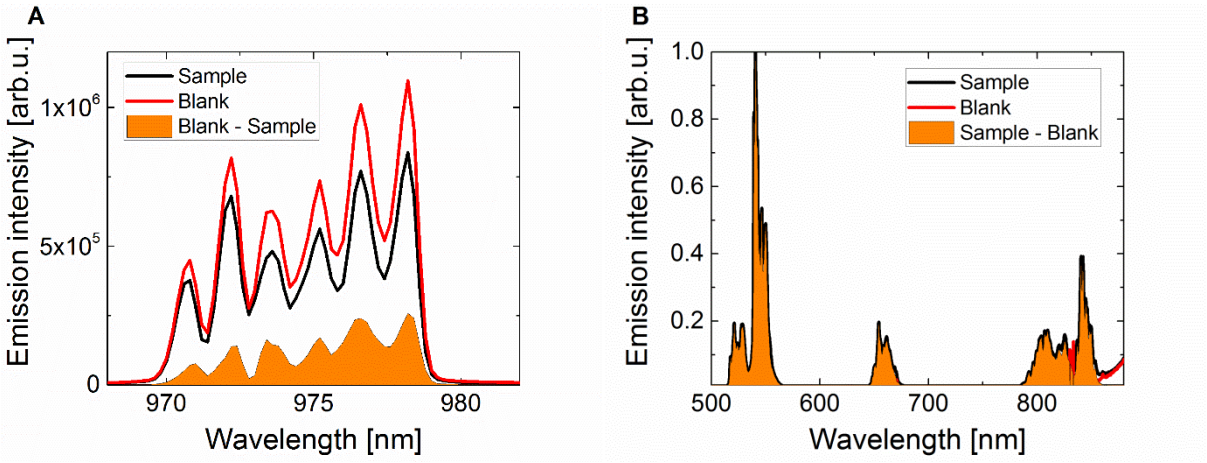

Figure 16: Corrected excitation (**panel A**; wavelength region: 968 – 982 nm) and emission (**panel B**; wavelength range 500 – 880 nm) spectra of a cuvette that is filled with a representative UCNP sample (12 nm-sized $NaYF_4$: 20 % Yb^{3+}, 2 % Er^{3+} UCNPs, dispersed in cyclohexane; black line) and with the respective blank material (cyclohexane - red line) that were measured with the integrating sphere setup. The orange area represents number of absorbed (panel A) and the according number of emitted photons (panel B) for this specimen.

The emission of the excited Yb^{3+} ions at 980 nm, however, was not considered for the determination of the number of absorbed photons, as it was already reported that it is typically negligible for core-only UCNPs. [38]

Integration ranges for data evaluation

The emission spectra were subdivided for data evaluation of the *P*-dependent UCL intensities into several emission bands. Their centre wavelengths, electronic transitions and integration ranges are displayed in Table 2 for the Yb^{3+}, Er^{3+} and in Table 3 for the Yb^{3+}, Tm^{3+} codoped UCNPs:

Yb^{3+}, Er^{3+} codoped particles:

Table 2: Centre wavelengths, electronic transitions and integration ranges that were used in this work for the Yb^{3+}, Er^{3+} codoped UCNPs.

Ln^{3+} ion	Centre wavelength	Electronic transition	Integration range ($\lambda_{IR\text{-}em}$)
Er^{3+}	410 nm	$^2H_{9/2} \rightarrow {}^4I_{15/2}$	400-430 nm
	520 nm	$^2H_{11/2} \rightarrow {}^4I_{15/2}$	510-535 nm
	540 nm	$^4S_{3/2} \rightarrow {}^4I_{15/2}$	535-570 nm
	655 nm	$^4F_{9/2} \rightarrow {}^4I_{15/2}$	630-685 nm
	810 nm	$^4I_{9/2} \rightarrow {}^4I_{15/2}$	783-833 nm
	850 nm	$^4S_{3/2} \rightarrow {}^4I_{13/2}$	833-860 nm

Yb^{3+}, Tm^{3+} codoped particles:

Table 3: Centre wavelengths, electronic transitions and integration ranges that were used in this work for the Yb^{3+}, Tm^{3+} codoped UCNPs.

Ln^{3+} ion	Centre wavelength	Electronic transition	Integration range ($\lambda_{IR\text{-}em}$)
Tm^{3+}	345 nm	$^3P_6 \rightarrow {}^3H_5$	334-353 nm
	375 nm	$^1D_2 \rightarrow {}^3H_6$	353-383 nm
	445 nm	$^1D_2 \rightarrow {}^3F_4$	433-462 nm
	475 nm	$^1G_4 \rightarrow {}^3H_6$	462-500 nm
	650 nm	$^1G_4 \rightarrow {}^3F_4$	610-675 nm
	700 nm	$^3F_3 \rightarrow {}^3H_6$	675-725 nm
	800 nm	$^3H_4 \rightarrow {}^3H_6$	725-860 nm
	744 nm	$^1D_2 \rightarrow {}^3F_3$	725-755 nm
	782 nm	$^1D_2 \rightarrow {}^3F_2$	755-800 nm

The latter two emission bands, however, only become visible at high *P*. To include these two UCL bands, which nearly disappear under the 800 nm emission at low *P*, I first normalized the UC spectra of one exemplarily chosen sample at very high and at relatively low *P* to the emission intensity at 804 nm. I then subtracted the emission spectra between 700-860 nm at low *P*

from the spectra at high P in the same wavelength region (see Figure 17) and subsequently calculated the branching ratio from $^1D_2$ to the $^3F_4$ (445 nm) and $^3F_{2/3}$ energy levels (744 and 782 nm). The resulting integrated intensity from all UCLs that originate from the $^1D_2$ Tm^{3+} energy level is therefore approximated to $I(^1D_2) = I_{375\,nm} + I_{445\,nm} + I_{744\,nm} + I_{782\,nm} = I_{375\,nm} + 2 \cdot I_{445\,nm}$.

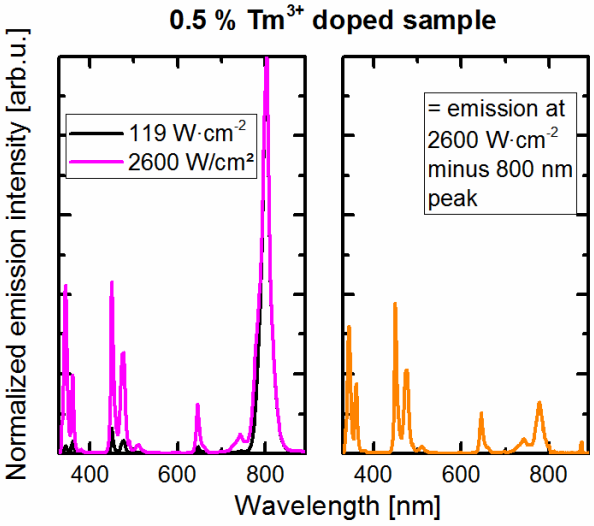

Figure 17. Normalized emission intensity of the exemplarily chosen 17 % Yb^{3+}, 0.5 % Tm^{3+} codoped sample at different P values. To highlight the two UCL bands from the $^1D_2$ energy level between 700-800 nm at higher P, we subtracted the emission peak at 800 nm using the spectra at lower P between 700-860 nm.

Relative spectral photon flux

The relative spectral photon fluxes were calculated according to (eq.) 07 with $I(\lambda_{IR\text{-}em})$ representing the integrated emission intensity in the respective integrating range and $I(\lambda_{all})$ representing the integrated emission intensity of the complete UCL spectra between 330 and 860 nm.

$$Relative\ spectral\ photon\ flux\ (\lambda_{IR-em})[\%] = {I(\lambda_{IR-em})}/{I(\lambda_{all})} \cdot 100\ \% \quad \text{(eq. 07)}$$

3.2.2 Time resolved measurements

The decay parameters of the respective excited Ln^{3+} states were investigated with pulsed fluorometry, using commercials setups that are based on the multi-channel scaling (MCS) method, which allows for the measurement of luminescence lifetimes in the range between 5 µs and 200 s. In short, photons are counted in a time window which sweeps across the full time range

following each excitation pulse. This process creates a histogram of intensity counts versus time. Its quality is therefore improved by adding the data of repeated sweeps.

Experimental setups

The time correlated studies from this work were respectively performed on two commercial spectrofluorometers from the company Edinburgh Instruments. Briefly, the Model FSP-920 respectively consists of two excitation and emission channels. Here, the excitation of the sample can either be performed with a µ-flash lamp 920H (pulse width of 3 µs) that was coupled to a monochromator, or with an electrically pulsed 978 nm laser diode that has an output power of 1 W (adjustable long square pulse width between 50 and 1,000 µs). The subsequently emitted light pulses were then either detected with a red extend photomultiplier tube (PMT) (R2658P) if their wavelength was < 1,000 nm, or with a NIR PMT (R5509P) if their wavelength was > 1,000 nm. Both PMTs were purchased from Hamamatsu. The excitation channels of the Model FLS980-xD2-stm spectrofluorometer were respectively equipped with two 8 W laser diodes, one with a centre wavelength of 978 nm and one with a centre wavelength of 808 nm (adjustable long square pulse widths between 50 and 1,000 µs). Its detection channel was equipped with a red-sensitive PMT from Hamamatsu (H10720-20).

Excitation wavelengths

The sensitizer ions were either excited at 940 nm, using the µ-flash lamp, or, because of the greater power of the laser, at 980 nm. The respectively detected emission wavelengths were set to 980 and 940 nm. The Er^{3+} activator ions were excited and detected in the wavelengths that are given in Table 4 and the Tm^{3+} activator ions were excited and detected in the wavelengths that are given in Table 5:

Yb^{3+}, Er^{3+} codoped particles:

Table 4: Electronic transitions, excitation (λ_{ex}) and emission wavelengths that were used in this work for the Yb^{3+}, Er^{3+} codoped UCNPs.

UC or DC?	Electronic transition	λ_{ex} [nm]	λ_{em} [nm]
UC	$^4S_{3/2} \rightarrow {}^4I_{15/2}$	980 nm	540 nm
UC	$^4F_{9/2} \rightarrow {}^4I_{15/2}$	980 nm	655 nm
DC	$^4S_{3/2} \rightarrow {}^4I_{15/2}$	490 nm	540 nm

DC	$^4F_{9/2} \rightarrow {}^4I_{15/2}$	380 nm	655 nm
DC	$^4I_{13/2} \rightarrow {}^4I_{13/2}$	980 nm	1530 nm

Yb^{3+}, Tm^{3+} codoped particles:

Table 5: Electronic transitions, excitation (λ_{ex}) and emission wavelengths that were used in this work for the Yb^{3+}, Tm^{3+} codoped UCNPs.

UC or DC?	Electronic transition	λ_{ex} [nm]	λ_{em} [nm]
UC	$^1D_2 \rightarrow {}^3H_6$	980 nm	360 nm
UC	$^1G_4 \rightarrow {}^3H_6$	980 nm	475 nm
UC	$^3F_3 \rightarrow {}^3H_6$	980 nm	700 nm
UC	$^3H_4 \rightarrow {}^3H_6$	980 nm	800 nm

Evaluation of the decay kinetics

Fitting of the decay kinetics of UCPs is rather challenging, due to the many different transfer processes via long-lived excited states that play a crucial part in the population of the respective investigated excited Ln^{3+} states. The result is a complex rise and decay behaviour with a still significant energy transfer shortly after the excitation pulse, which can vary for different samples. Therefore only mean lifetimes of luminescence decay spectra that were measured under similar conditions can be obtained, including the same time windows, number of channels and excitation pulse widths.

Fit of the decay components. The luminescence decay kinetics *I(t)* were therefore subsequently fitted according to (eq.) 08 with a mono-, or multi-exponential decay tail fit, always using the time channel were no further rising component was apparent as a starting point. a_i and τ_i represent the respective amplitude- and lifetime components. Furthermore, the amplitude average lifetime τ_{mean} was calculated according to (eq.) 09 to allow a comparison of the decay of the respective excited Ln^{3+} states. [89]

$$I(t) = I_0 \sum a_i exp(-t/\tau_i) \quad \text{(eq. 08)}$$

$$\tau_{mean} = \sum a_i \tau_i \, / \sum a_i \quad \text{(eq. 09)}$$

Integration of decay curve. Fitting of the lifetime components, however, is not feasible for the comparison of the luminescence decay kinetics of samples with a very low UCL intensity. For the desired comparison of the decay curves of such samples, the integrated decay curves, consistently normalized after the excitation pulse, were chosen (for more information see also Figure 41 in the *section 4.4.4*). These integrated intensities were subsequently utilized to calculate the so-called "quenching efficiency" of an investigated process according to (eq.) 10. [90]

$$\eta(quenching)(\%) = 100\ \% \cdot \left(1 - \frac{I_q}{I_0}\right) \qquad \text{(eq. 10)}$$

I_q represents the intensity in the presence of a luminescence quencher / quenching process and I_0 the initially measured integrated luminescence decay curve in the absence of a quencher / quenching process, respectively.

4 Results and discussion

This chapter focuses on the four important issues that were mentioned in the introduction part. In short, the first study investigated the question why small UCNPs exhibit way lower efficiency values than their microcrystalline counterparts, the second study explored ideas for other UC nanostructures than the typical Yb^{3+}, Er^{3+} codoping with the aim to overcome the small efficiency values, the third study aimed to identify the optimal doping concentrations that result in the highest UCL of the various Tm^{3+} UCL bands and the (de)population mechanism that lead to them, and lastly, the fourth study analysed the impact of the partial dissolution of UCNPs in aqueous solutions on their spectroscopic properties, aiming to identify an easy to use parameter for the long-term stability screening of UCNPs.

4.1 Correlating size and surface effects

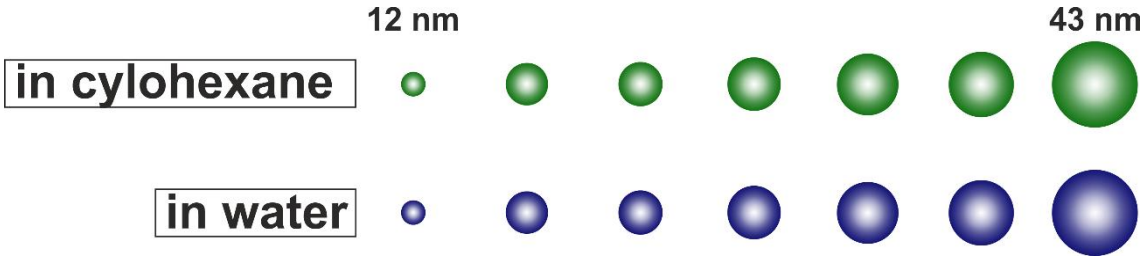

Figure 18: Schematic representation of the UCNP samples that were investigated in this study.

As mentioned in *section 2.2.2*, UCNPs with small diameters show efficiency values that are several orders of magnitude smaller than their microcrystalline counterparts. Our general interest in a better understanding of the complex interplay of the parameters controlling *e.g.*, UCL colour and intensity, therefore encouraged our research group to systematically assess the UCL features of exemplarily chosen 23 nm-sized $NaYF_4$: 20 % Yb^{3+}, 2 % Er^{3+} UCNPs in different environments using steady state and time-resolved fluorometry and integrating sphere spectroscopy. [57] The study presented here is an extension of this previous one and aims to identify the quenching mechanisms that lead to the small efficiency values in organic and aqueous media. Special attention was dedicated to the influence of *P* and surface quenching on the emission colour with the overall goal to quantify the potential of *P* for counterbalancing size- and microenvironment-induced UCL quenching and to clarify the still debated population dynamics of the red emissive $^4F_{9/2}$ energy level of Er^{3+}. The results are published in Ref. [91]. A schematic representation of all investigated UCNP samples is given in Figure 18.

4.1.1 UCNP preparation

As a prerequisite for this study, the research group of Doctor Hirsch from the University of Regensburg synthesised five different batches of UCNPs with respective average diameters between 12 and 43 nm, exchanged the surface ligands of a fraction of the respective batches from oleic acid to polyacrylic acid (PAA) and subsequently dispersed these PAA-stabilized UCNPs in deionized water. The synthesis and surface modifications of three of the five nanocrystal batches were performed with previously reported protocols. [92] As this method only yields UCNPs with diameters between 20 and 35 nm, a codoping with 25 % Gd^{3+} was used for the preparation of UCNPs with smaller sizes to ensure the growth of a hexagonal crystal lattice as reported by other groups, [28, 42, 93] while for the synthesis of larger particles, a core-shell approach was employed, with core and shell consisting of the same chemical composition, *i.e.*, $NaYF_4$: 20 % Yb^{3+}, 2 % Er^{3+}. Afterwards, three more additional batches were synthesized to investigate a possible influence of the Gd^{3+} codoping and the core-shell approach used to tune UCNP size.

4.1.2 Structural and chemical analysis

Our cooperation partners subsequently carried out DLS measurements, revealing the colloidal stability and monodispersity of all five batches. The crystal structure of the UCNP samples was examined with an XRD analysis, while TEM measurements were performed to determine the particle diameters. The results of the XRD measurements confirmed the aimed hexagonal $Na(Y,Gd)F_4$: Yb^{3+}, Er^{3+} crystal structures of the smallest and hexagonal $NaYF_4$: Yb^{3+}, Er^{3+} crystal structures for the other four UCNP batches investigated. The corresponding diameters of the core-only particles are (12.2 ± 0.4), (21.1 ± 1.0), (26.6 ± 0.8) and (30.7 ± 1.0) nm. The UCNPs that were produced in the core-shell approach have diameters of (34.5 ± 0.8) nm for the particle core and (42.8 ± 1.7) nm for the final particles.

The first of the additional batches consists of UCNPs with hexagonal $Na(Y,Gd)F_4$: Yb^{3+}, Er^{3+} crystal structures and particle diameters of (21.9 ± 0.6) nm, while the second one consists of UCNPs with hexagonal $NaYF_4$: Yb^{3+}, Er^{3+} crystal structures and particle diameters of (23.8 ± 1.0) nm. The last batch of UCNPs was synthesized in the core-shell approach with hexagonal $NaYF_4$: Yb^{3+}, Er^{3+} crystal structures and particle diameters of (26.6 ± 0.8) nm for the particle

core and (32.5 ± 1.4) nm for the final particles. Lastly, inductively coupled plasma optical emission spectroscopy measurements were performed for the determination of the real doping concentrations of rare-earth ions in the UCNPs, respectively revealing closely matching doping concentrations of the 20 % Yb^{3+} and 2 % Er^{3+} ions for all eight UCNP batches.

4.1.3 Spectroscopic analysis

The influence of *P* and surface quenching on the emission colour was investigated by me with the integrating sphere setup previously reported for the 21, 26, and 31 nm-sized UCNPs in cyclohexane and deionized water [38, 57, 86] and for the 12 and 43, and the additional 22, 24 and 32 nm-sized UCNPs with the newly assembled and calibrated setup that was mentioned in *section 3.2.1*. All decay kinetics were recorded with the spectrometers that were mentioned in *section 3.2.2*.

The first step of the spectroscopic analysis was to study a possible influence of the Gd^{3+} codoping and the core-shell approach that were both used to tune the UCNP sizes. The influence of the Gd^{3+} codoping was examined by a comparison of the typical spectroscopic features of 22 nm-sized UCNPs that were additionally codoped with Gd^{3+} with 21 and 24 nm-sized UCNPs lacking Gd^{3+}. The influence of the core-shell approach was investigated by a comparison of a core-only with a core-shell UCNP sample with diameters of about 31 and 32 nm, respectively.

Possible influence of Gd^{3+} codoping

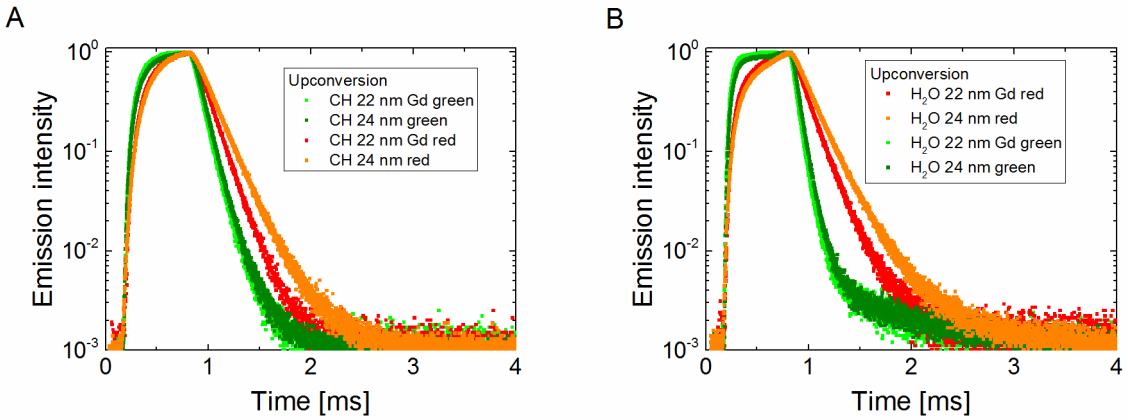

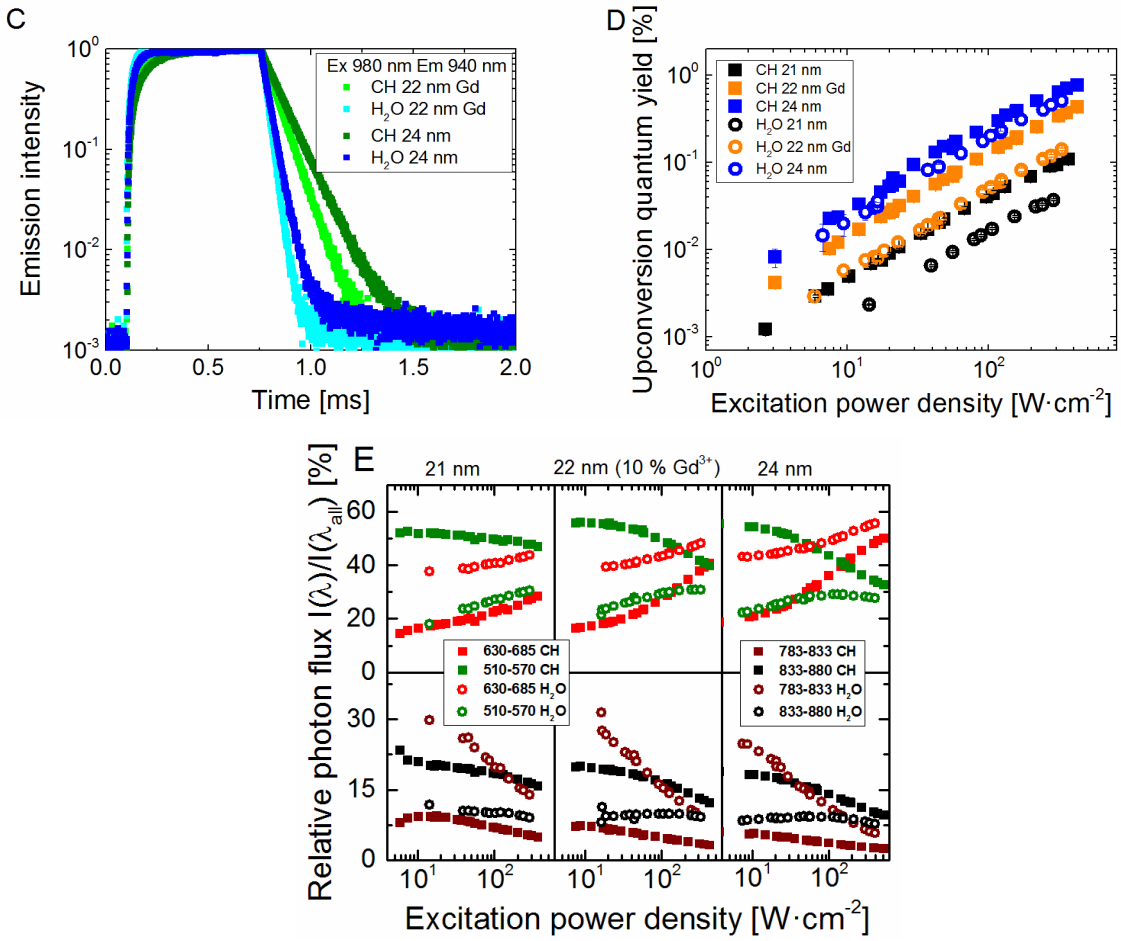

Figure 19. "UCL decay kinetics of the Er^{3+} emission at 540 (green) and 655 nm (red) in cyclohexane (**panel A)** and in H_2O (**panel B**) and of the directly (at 940 nm) excited Yb^{3+} emission at 980 nm in cyclohexane (green) and in H_2O (blue) (**panel C**). **Panel D:** *P*-dependence of Φ_{UC} of 22 nm-sized UCNPs codoped with 10 % Gd^{3+}, and 24 and 21 nm-sized UCNPs lacking Gd^{3+} codoping. **Panel E:** Relative photon flux of the Er^{3+} emission bands from 510-570 nm (green), 630-685 nm (red), 783-833 nm (brown) and 833-860 nm (black), in cyclohexane (full symbols) and H_2O (open symbols) for the 21, 22, and 24 nm-sized UCNPs." Reproduced with permission. [91]

The decay curves in panels A-C of Figure 19 display the comparison of the typical UC decay kinetics of two of the three UCNP samples with and without Gd^{3+} codoping in cyclohexane and water, revealing similar decay times for the 540 nm and longer ones for the 655 and 980 nm emission for the bigger 24 nm-sized UCNPs lacking Gd^{3+}, compared to the 22 nm-sized sample containing 10 % Gd^{3+}. A further comparison with the 21 nm-sized UCNPs lacking Gd^{3+} again reveals similar decay times for the 540, but smaller ones for the 655 and 980 nm emission, compared to the 22 nm-sized UCNPs (data not shown). Panel D and E also include the 21 nm-sized sample lacking Gd^{3+} and respectively show the Φ_{UC} and relative photon flux values, cal-

culated according to (eq.) 07, in both investigated solvents. The results show significantly different values, however, the trend of, *e.g.*, smaller Φ_{UC} values for smaller UCNPs, clearly implicates that the leading cause of these differences is not the Gd^{3+} codoping, but rather the different particle sizes. It can therefore be concluded that there is no significant influence of the Gd^{3+} codoping on the spectroscopic properties of our UCNP samples.

Possible influence of core-shell structure

Panels A-C of Figure 20 display the typical UC decay kinetics of the 31 nm-sized core-only and the 32 nm-sized sample that was synthesized with the core-shell approach. The results from panels A-C always show longer decay times for the bigger UCNPs. Note that, as mentioned in *section 2.2.2*, longer lifetimes would be expected for larger UCNPs anyhow. The results from the Φ_{UC} values in panel D of Figure 20 do not show such a clear trend. For example, although this panel reveals bigger Φ_{UC} values of the bigger UCNPs in water, it shows similar values in cyclohexane at low P and even smaller values at high P. Yet, the relative spectral photon fluxes in panel E of Figure 20 show no significant differences. It can therefore be conclude that this approach causes only small changes in UCL features, which are neglected in the following, except for slightly lower Φ_{UC} values at high P for the core-shell particles in cyclohexane.

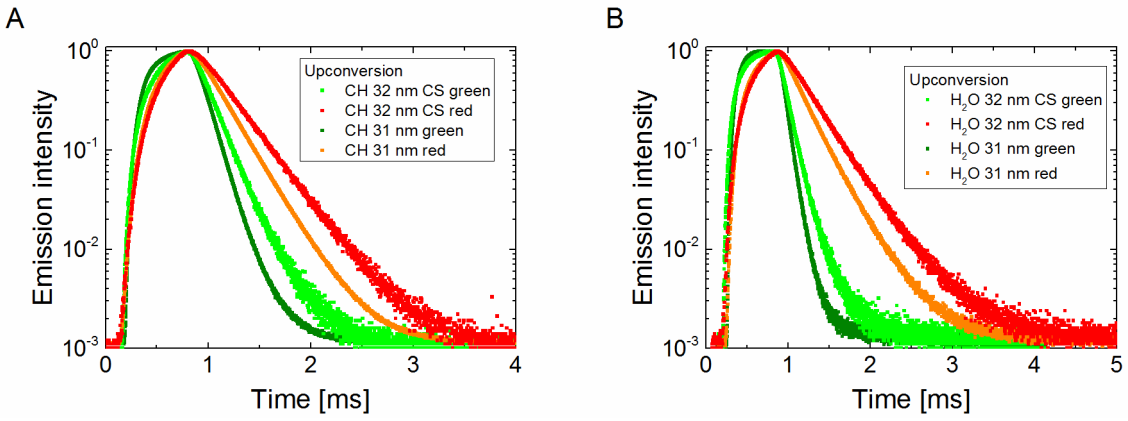

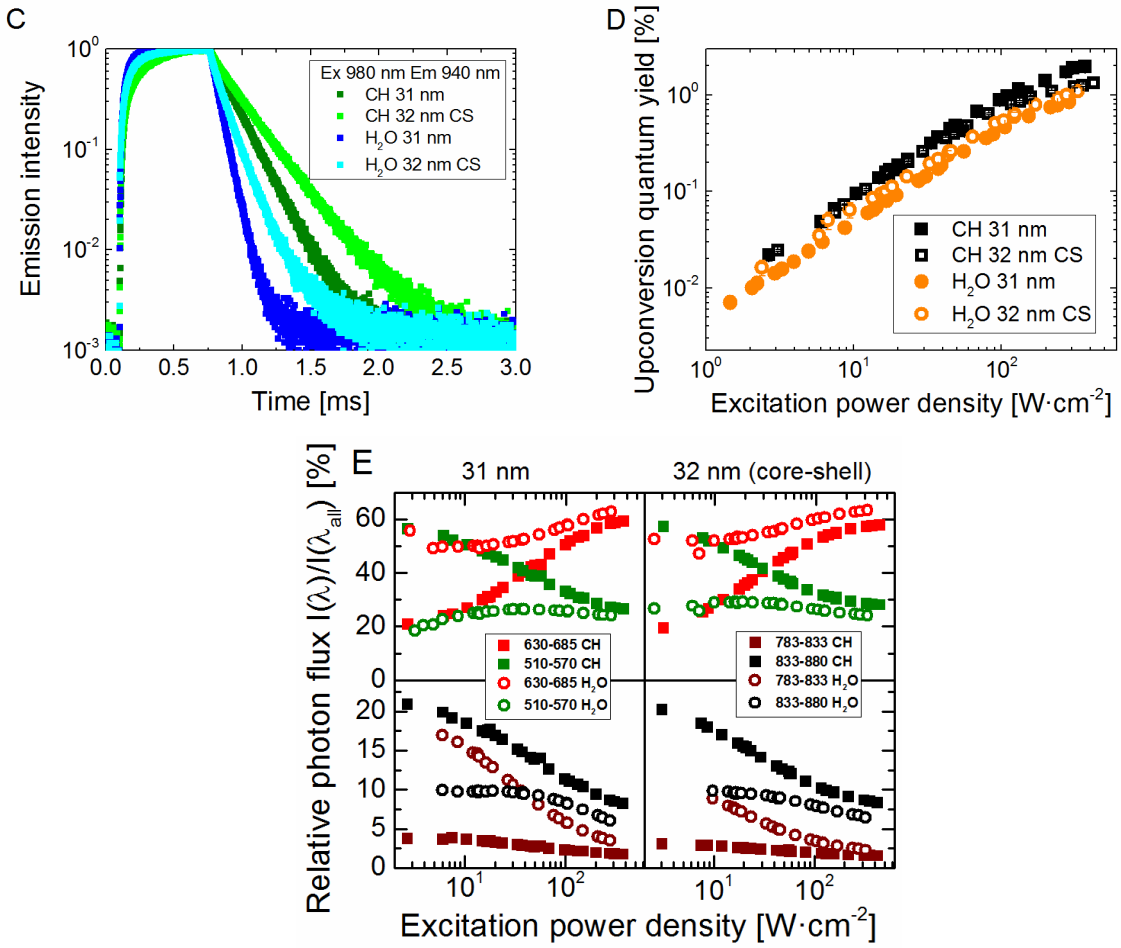

Figure 20. "UCL decay kinetics of the Er^{3+} emission at 540 (green) and 655 nm (red) in cyclohexane (**panel A**) and H_2O (**panel B**), of the directly (at 940 nm) excited Yb^{3+} emission at 980 nm in cyclohexane (green) and in H_2O (blue) (**panel C**). **Panel D:** *P*-dependence of Φ_{UC} of a 32 (core-shell with same doping) and 31 nm-sized core-only sample. **Panel E:** Relative photon flux of the Er^{3+} emission bands at 510-570 nm (green), 630-685 nm (red), 783-833 nm (brown) and 833-860 nm (black), in cyclohexane (full symbols) and H_2O (open symbols) for the 31 and 32 nm-sized particles." Reproduced with permission. [91]

Influence of UCNP size and *P* on UCL colour

Figure 21 gives a first brief view on the influence of the particle size and microenvironment on the respective UC spectra. It displays the emission spectra of the 12 and 43 nm-sized UCNPs from this series, dissolved in cyclohexane and water at an exemplarily chosen *P* of 50 $W \cdot cm^{-2}$ and excitation wavelength of 980 nm, as typically used in bioassays [94-96], and normalized at 540 nm, respectively. This clearly reveals different relative photon fluxes, not only while comparing similar sized UCNPs in both solvents, but also while comparing differently sized UCNPs

in the same microenvironment. The most intriguing part here is the relatively strong contribution of the 810 nm UCL for small UCNPs in water, where UCL is strongly quenched, and even in cyclohexane. The contribution from this emission is, *e.g.*, around 31 times higher for the 12 than for the 43 nm-sized UCNPs in water and even exceeds that of the 12 nm-sized UCNPs in cyclohexane by a factor of about seven. This highlights that this 810 nm NIR UCL is not negligible for small UCNPs, neither for particles that are dissolved in aqueous solutions, nor for ones that are dissolved in organic media. It even becomes dominant for small UCNPs in water, while for all other circumstances, the visible UCLs are dominant.

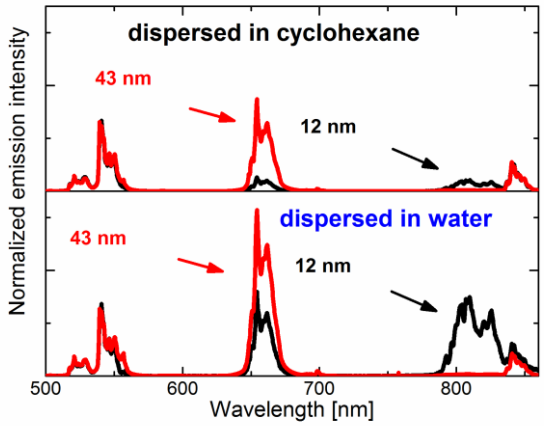

Figure 21. "Spectrally corrected emission spectra of 12 and 43 nm-sized UCNPs in cyclohexane (upper panel) and H_2O (lower panel) at *P* of 50 $W \cdot cm^{-2}$ normalized at 540 nm, upon 980 nm excitation." Reproduced with permission. [91]

More detailed insights can be gained by a closer view on the *P*-dependent relative spectral photon fluxes of the differently sized UCNPs in both solvents, which are displayed in panel A of Figure 22. These values reflect the competition between the radiative depopulation processes of excited Er^{3+} ions, ETU rates from Yb^{3+} sensitizer ions and non-radiative decay pathways from both ions. One of the most obvious observations from this figure is, that an increase in *P* in most cases results in enhanced contributions of the 655 nm and decreased contributions from the 810 nm Er^{3+} UCL, except for the smallest and largest UCNPs from this study, where the contributions from the 655 nm Er^{3+} emission are nearly constant for a low and high *P*. This behaviour underlines the higher photonic order process on the 655 nm UCL, compared to the other UC emission bands. The $^4F_{9/2}$ Er^{3+} energy level, from which this emission occurs, can be populated via bi- and / or triphotonic absorption processes, while the 540 nm UCL is typically

populated via biphotonic absorption processes, and to the 810 nm UCL, which is typically populated via a first ($^2F_{5/2}$→$^2F_{7/2}$; $^4I_{15/2}$→$^4I_{11/2}$) ETU step, followed by a $^4I_{11/2}$→$^4I_{13/2}$ MPR and a ($^4I_{13/2}$→$^4I_{15/2}$; $^4I_{13/2}$→$^4I_{9/2}$) ET step. The trends of only small changes in the relative photon flux values of the green and red Er^{3+} UCL bands for the 12 nm-sized UCNPs up to the highest *P* of 430 W·cm^{-2} used here, and of the 43 nm-sized UCNPs for $P > 60$ W·cm^{-2}, indicate similar photonic orders of the population dynamics of the $^4S_{3/2}$ and the $^4F_{9/2}$ energy levels of Er^{3+} under these conditions.

An extrapolation of the size-dependent relative photon fluxes at fixed excitation densities, as displayed in panel B of Figure 22, reveals that in cyclohexane, different UCL bands become dominant for different particle sizes and *P* values. For instance, the UC spectra at 290 W·cm^{-2} are dominated by the red Er^{3+} UCL for UCNPs with sizes above 23 nm, and by the green Er^{3+} UCL for UCNPs with sizes below 23 nm. At low *P*, the UCL in cyclohexane is always dominated by the green Er^{3+} UCL band for all particle sizes investigated in this study. The red UCL is the second strongest UCL band for diameters above 26 nm and low *P*, however, for smaller particle sizes and low *P*, it is outclassed by both NIR UCL bands. The extrapolation also reveals that at high *P* the contributions from the red Er^{3+} UCL band always increases for increasing particle sizes from 12 to 26 nm, while the contributions from the other UCL bands here always decrease with, *e.g.*, a factor of about two for the 540 and of about six for the 810 nm UCL. UCNPs with bigger particle diameters than 26 nm show no significant differences at high *P*. The contributions at low *P* at different particle sizes overall show a similar trend.

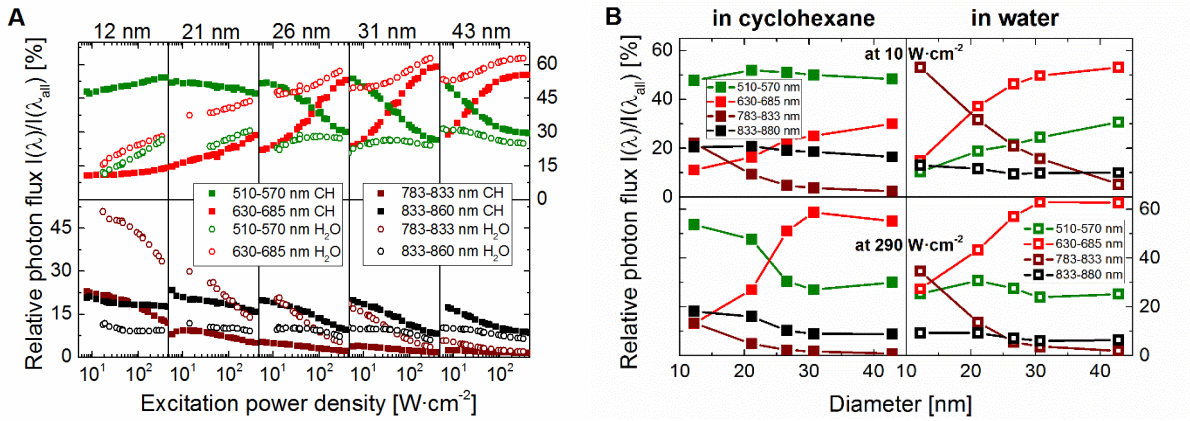

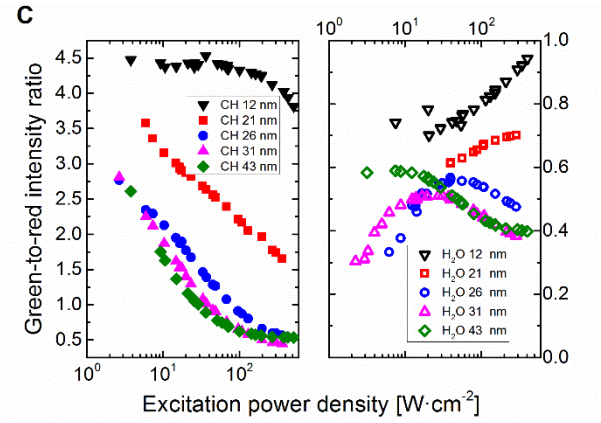

Figure 22. "Panel A: Relative photon flux of the Er^{3+} emission bands between 510-570 nm (green), 630-685 nm (red), 783-833 nm (brown) and 833-860 nm (black), in cyclohexane (full symbols) and H_2O (open symbols) for the 12, 21, 26, 31, and 43 nm-sized UCNPs. **Panel B:** Relative photon flux versus particle diameters in cyclohexane (left panels - solid lines) and water (right panels - dotted lines) for *P* of 10 $W \cdot cm^{-2}$ (upper panels) and 290 $W \cdot cm^{-2}$ (lower panels), respectively. **Panel C:** *P*-dependence of the integrated intensity ratio of the green emission between 510-570 nm and the red emission between 630-685 nm in cyclohexane (left) and water (right) for 12, 21, 26, 31 and 43 nm-sized UCNPs." Reproduced with permission. [91]

The size- and *P*-dependent relative spectral photon fluxes of the differently sized UCNPs in water reveal that the UC spectra in this microenvironment are never dominated by the green Er^{3+} UCL. The contributions from this UCL are here in fact even always lower than the contributions from the red Er^{3+} UCL. This can be ascribed to reduced UC emission intensities of the 540 nm UCL due to efficient coupling of the $^4S_{3/2}$ Er^{3+} energy level, from where this emission originates, to O-H vibrations from surrounding solvent molecules. It is also noteworthy that again a reduction in UCNP size results in decreased contributions from the 655 and enhanced contributions from the 810 nm UCL at high *P* for UCNP sizes between 12 and 26 nm, and in only small changes for bigger particle sizes. As a result, the UC spectra of UCNPs at high *P* in water are dominated by the 810 nm UCL for UCNPs that are smaller than about 12 nm, and by the 655 nm UCL for bigger UCNPs. The changes at low *P* are even more pronounced, showing a dominant 810 nm UCL for particle sizes below about 21 nm, and a dominant 655 nm UCL for bigger particles. At 10 $W \cdot cm^{-2}$ even more than 50 % of all UC photons are emitted between 783 and 833 nm, upon 980 nm excitation. This highlights the need to re-evaluate recent rate equation models, as they do not consider this NIR emission and are therefore not able to comprehensively describe the (de)population processes of small UCNPs in biologically relevant aqueous media. [54, 57, 58, 75]

The effect of an increasing relative contribution of the 810 and decreasing relative contributions of the 655 nm UCL with decreasing particle sizes in both solvents can be ascribed to increased radiationless decay of the Yb^{3+} ions, resulting in a depopulation of the Er^{3+} energy levels with higher photonic orders. This is also reflected by the integrated intensity ratios from the higher energy level at 410 nm, and from the lower energy level at 810 nm. For example, the integrated intensity ratio of these two UCL bands respectively shows decreasing values for a comparison of the 43 nm-sized UCNPs in cyclohexane, the 43 nm-sized UCNPs in water, the 12 nm-sized UCNPs in cyclohexane, and the 12 nm-sized UCNPs in water (data not shown).

A further comparison of the size- and *P*-dependent intensity ratios from both prominent visible UC emissions in panel C of Figure 22 also reveals, that UCNPs with sizes exceeding 26 nm show a very similar UCL behaviour. This demonstrates that the $^4S_{3/2}$, $^2H_{11/2}$ and $^4F_{9/2}$ are populated by similar processes. There are even similar values of *G/R* between 0.4 and 0.6 for UCNPs in both solvents for $P > 160$ W·cm^{-2}, indicating that the $^4F_{9/2}$ Er^{3+} energy levels in both solvents are populated by the same processes at high *P*. This assumption is also substantiated by the decreasing *G/R* values for very high *P*, shown in panel C of Figure 22 for UCNPs with sizes above 21 nm.

P-dependence of the slope factors $n_{\lambda em}(P)$

The so-called *P*-dependent slope factors $n_{\lambda em}(P)$ of the respective UC emission bands reveal more insights in the *P*-dependent population behaviour of the respective energy level from which the UCL originates. They can be obtained by a log-log plot of the emission intensity versus the excitation power density, according to (eq.) 02 and are displayed in panel A of Figure 23 for the prominent visible Er^{3+} UCLs at 540 and 655 nm, exemplarily chosen for the 12, 26 and 43 nm-sized UCNPs in both solvents. This figure shows that in cyclohexane, $n_{655\,nm}$ decreases from $n_{655\,nm}(d = 43\text{ nm}, 10\text{ W·cm}^{-2}) > 2.4$ to $n_{655\,nm}(d = 12\text{ nm}, 10\text{ W·cm}^{-2}) \approx 2.0$ with decreasing size at low *P*, while a constant slope factor for all particle sizes of $n_{655\,nm} \approx 2$ in water at low *P* can be reported. For UCNPs with particle diameters above 12 nm, increasing *P* eventually results in a diminution of both $n_{655\,nm}$ and $n_{540\,nm}$ in cyclohexane and water, which can be explained by a gradual saturation of the lower Er^{3+} energy levels. Hence, for UCNPs with sizes about 12 nm or smaller, $P > 400$ W·cm^{-2} are needed to saturate the lower Er^{3+} energy levels and consequently *n* at high *P* is bigger for smaller particle diameters. The slope factor of the UCL

at 540 nm at low *P* does not change significantly and remains at $n_{540\ nm}(10\ W{\cdot}cm^{-2}) \approx 2$ in cyclohexane and water for all particle sizes.

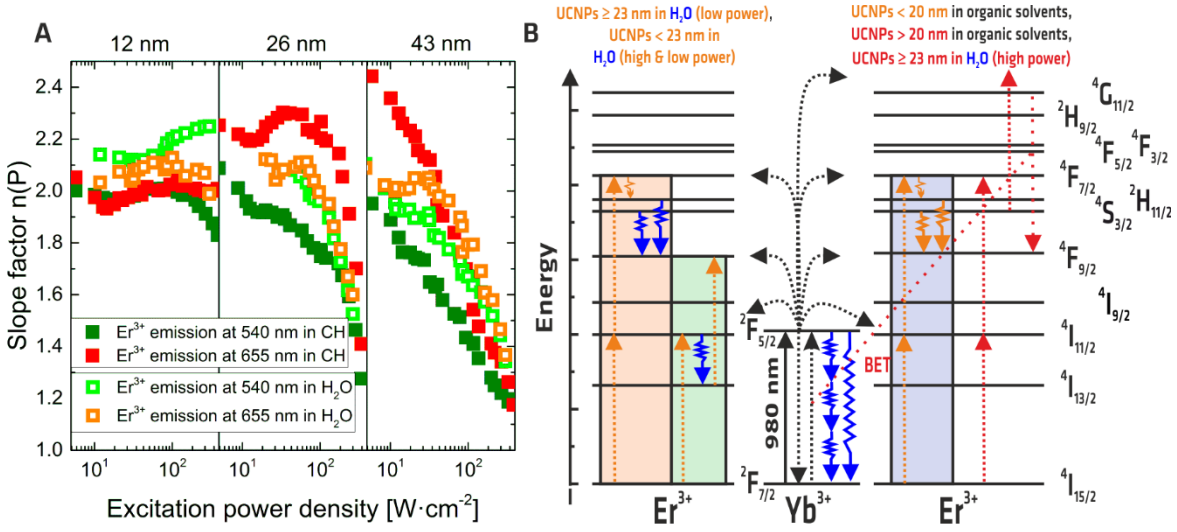

Figure 23. "**Panel A:** *P*-dependent slope factors of the green (540 nm) and red (655 nm) integral UC emissions of 12, 26, and 43 nm-sized UCNPs in cyclohexane (red and dark green full symbols) and in water (orange and light green open symbols), respectively. The plots were smoothed with a Savitzky-Golay filter. **Panel B:** Energy level diagram of $NaYF_4$: Yb^{3+}, Er^{3+} UCNPs. The predominant population pathways of the $^4F_{9/2}$ Er^{3+} energy level for certain UCNP sizes and environments are highlighted in orange for the two-photonic and in red for the three-photonic pathways. The solid and dotted arrows represent photon absorption and emission and the blue zig-zag arrows represent increased non-radiative relaxations favoured by high energy O-H vibrations. [61] BET: back energy transfer;" Reproduced with permission. [91]

Population pathways of the red Er^{3+} level

An extrapolation of $n_{655\ nm}$ at respectively low and high *P* versus the particle diameter indicates, that the $^4F_{9/2}$ Er^{3+} energy level can be fed not only by biphotonic $^4I_{13/2} \rightarrow {}^4F_{9/2}$, but also by triphotonic $^4G_{11/2} \rightarrow {}^4F_{9/2}$ processes, as discussed in *section 2.2.2*. This triphotonic contribution becomes significant for UCNPs with particle diameters exceeding 20 nm in apolar solvents, and also for UCNPs exceeding 23 nm in water at high *P*. For smaller UNCPs in cyclohexane and water, and also for bigger UCNPs in water at low *P*, 655 nm emissions are populated only by biphotonic processes. This behaviour can be attributed to a strong quenching of higher excited Er^{3+} energy levels, hampering the triphotonic population pathway. The subsequently newly proposed population pathways of the $^4F_{9/2}$ energy level, based on the results from this study and our previous work, [57] are summarized in panel B of Figure 23.

Luminescence decay behaviour

Both the up- and down-converted luminescence decay kinetics of our nanocrystals were assessed to investigate the mechanism of surface quenching in more detail. The measurements included the down- and upconverted (DC and UC) lifetimes of $^4S_{3/2}$ (540 nm) and $^4F_{9/2}$ (655 nm) and DC lifetimes of $^4I_{13/2}$ (1530 nm) radiative energy levels of Er^{3+} and also lifetimes of the excited $^2F_{5/2}$ level of Yb^{3+}. As mentioned in *section 2.2.1*, in case of UC, all Yb^{3+} and Er^{3+} energy levels participate in the energy migration processes and therefore contribute to the overall lifetimes of the respective energy levels. In case of DC, however, only the lifetimes and energy transfer rates of the higher Er^{3+} energy levels contribute to the overall lifetime of the respective energy level.

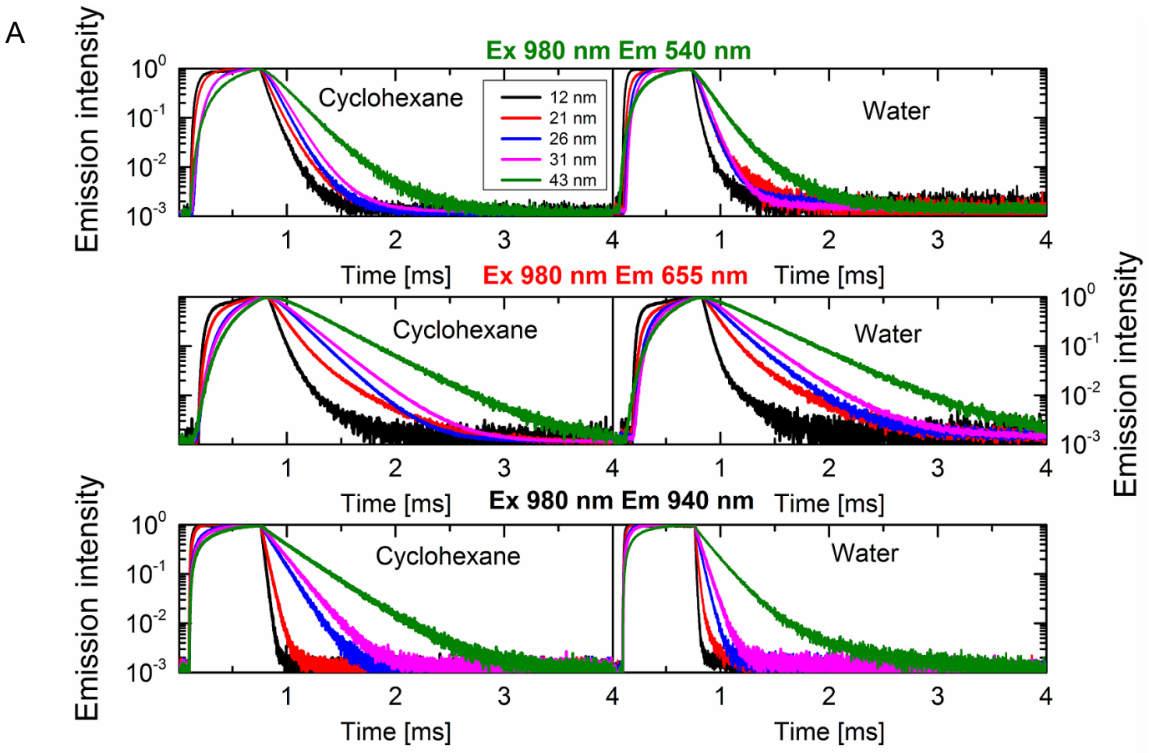

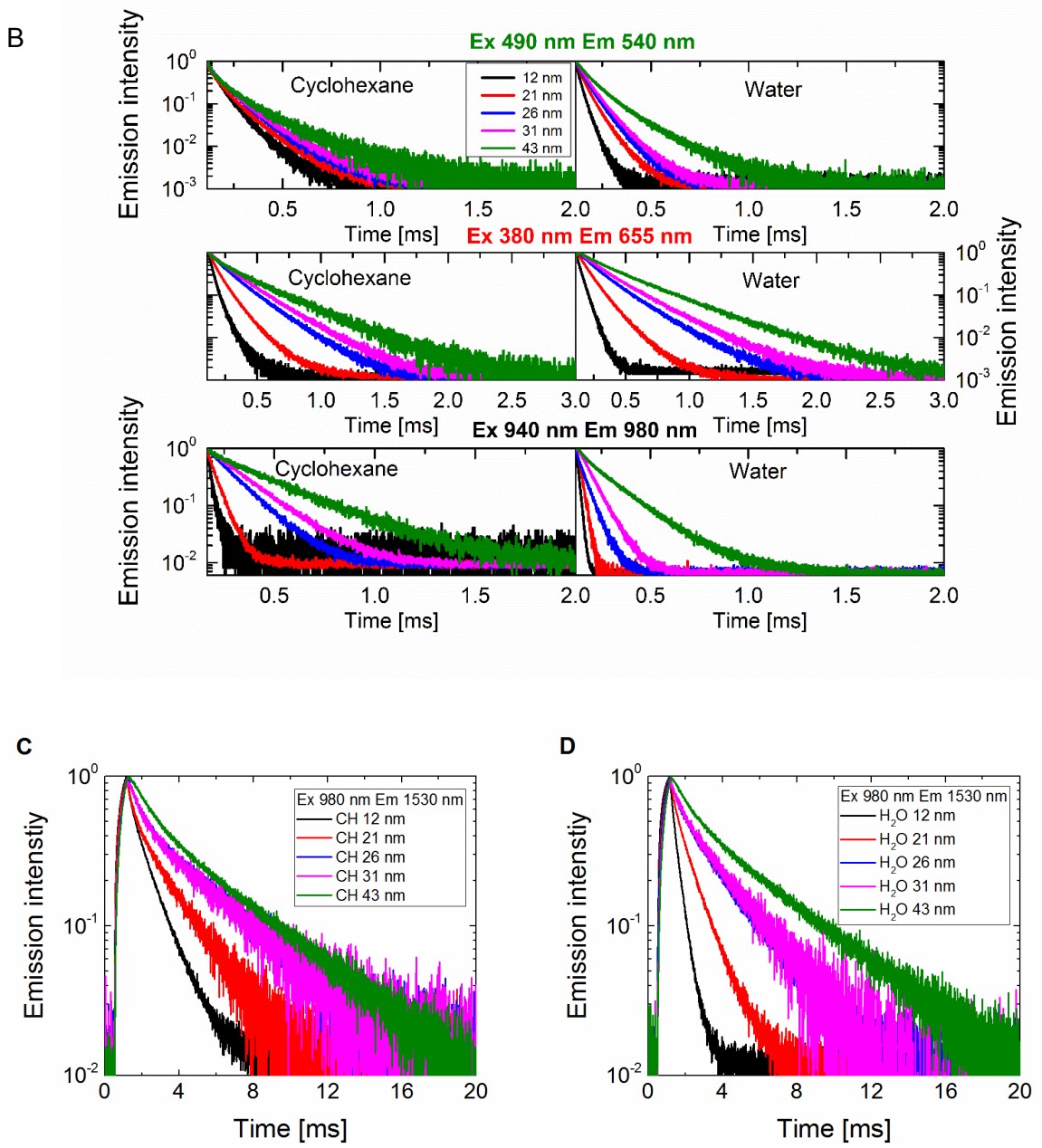

Figure 24. "**Panel A:** Decay kinetics of the green (upper panel) and red (middle panel) UC emission of Er^{3+} and the UC emission of Yb^{3+} at 940 nm (lower panel) of 12, 21, 26, 31 and 43-nm-sized UCNPs in cyclohexane (left panels) and water (right panels). **Panel B:** Luminescence decay kinetics of the green (upper panel), red (middle panel) and 980 nm (lower panel) DC emission bands of 12, 21, 26, 31 and 43 nm-sized UCNPs in cyclohexane (left panels) and water (right panels) excited at 490 nm, 380 nm, and 940 nm, respectively. **Panels C and D** respectively display the time-resolved spectroscopy of the 1530 nm downconversion emission of 12, 21, 26, 31 and 43-nm-sized particles in cyclohexane and in H_2O." Reproduced with permission. [91]

The UC decay kinetics of the 540, 655 and 940 nm emissions of all five batches in both solvents are subsequently displayed in panel A of Figure 24. The corresponding DC decay kinetics are

shown in panel B of Figure 24 for excitation at 490, 390 and 940 nm. The DC decay kinetics of the Er^{3+} luminescence at 1,530 nm upon 980 nm excitation are displayed in panels C and D of Figure 24. The respective left panels show the temporal behaviour of UCNPs in cyclohexane, while the right panels show the temporal behaviour of UCNPs in water. The corresponding fitted mean lifetimes of the UC spectra are displayed in Table 6, while the mean lifetimes from the DC spectra are displayed in Table 7. A first brief comparison of τ_{mean} of the 540 and 655 nm UC emission bands of the largest and smallest UCNPs of our size series revealed a diminution by factors of 2.7 and 4.4 in cyclohexane and by factors of 3.5 and 5.3 in water, respectively. τ_{mean} of the Yb^{3+} emission in water is always smaller than that of similarly sized UCNPs in cyclohexane. These findings agree well with the mean decay rates reported by other groups for differently sized UCNPs, which typically only focus on the UC decay kinetics. [43, 46, 48, 97, 98]

Table 6 . "Mean decay times of the red (655 nm) and green (540 nm) UCL bands of Er^{3+}, excited at 980 nm and the mean decay times of the NIR Yb^{3+} emission (excited at 940 nm) of differently sized $NaYF_4$: 20 % Yb^{3+}, 2 % Er^{3+} UCNPs in cyclohexane (CH) and H_2O. The main component of the biexponential fit of the 940 nm emission is highlighted." Reproduced with permission. [91]

	CH 12	**CH 21**	**CH 26**	**CH 31**	**CH 43**	**H_2O 12**	**H_2O 21**	**H_2O 26**	**H_2O 31**	**H_2O 43**
Er^{3+} UC emission at 540 nm										
τ_{mean} [µs]	78	92	116	136	213	48	92	125	127	166
Er^{3+} UC emission at 655 nm										
τ_{mean} [µs]	85	194	211	249	377	83	207	233	272	444
Yb^{3+} emission at 940 nm										
τ_1 [µs]	**23**	**41**	**124**	140	224	**08**	**19**	**46**	**64**	**161**
τ_2 [µs]	360	106	664	**167**	**325**	30	101	1180	1330	605
τ_{mean} [µs]	29	44	71	159	295	09	29	91	106	205

Table 7. "Downconversion (DC) luminescence mean decay times of the red (655 nm) and green (540 nm) emissive Er^{3+} energy levels and of the Yb^{3+} NIR emission (excitation at 940 nm, recorded at 980 nm) of differently sized $NaYF_4$: 20 % Yb^{3+}, 2 % Er^{3+} nanoparticles in cyclohexane (CH) and H_2O." Reproduced with permission. [91]

	CH 12	**CH 21**	**CH 26**	**CH 31**	**CH 43**	**H_2O 12**	**H_2O 21**	**H_2O 26**	**H_2O 31**	**H_2O 43**
$^4S_{3/2} \rightarrow {}^4I_{15/2}$ (Er^{3+} emission at 540 nm) – excited at 490 nm										
τ_{mean} [µs]	67	97	105	116	135	29	53	64	72	119
$^4F_{9/2} \rightarrow {}^4I_{15/2}$ (Er^{3+} emission at 655 nm) – excited at 380 nm										
τ_{mean} [µs]	39	102	182	216	283	41	112	204	249	356
Yb^{3+} emission at 980 nm – excited at 940 nm										
τ [µs]	21	44	125	164	289	13	25	47	65	155

The next step is to quantify the observed quenching effects for the individual Ln^{3+} energy levels. The influence of particle size on the mean DC lifetimes of the Er^{3+} and Yb^{3+} emission bands in cyclohexane and water is therefore displayed as percentages of τ_{mean} of the respective bulk material, taken from measurements of µm-sized powder samples of the *Berry* and our research group [38, 39] (panel A of Figure 25). The bulk material serves as a rough estimate for an unquenched reference. Note that this approach is only feasible for UCPs with similar doping concentrations, as otherwise CR processes can complicate the comparability of the respective mean lifetimes. In this case, a comparison of the respective rate constants would be feasible, which, however, requires a very time consuming data evaluation. Panel A of Figure 25 clearly illustrates the reduction in τ_{mean} of all DC emission bands with decreasing particle size. It shows that, *e.g.*, for 12 nm-sized UCNPs in cyclohexane, τ_{mean} of the green Er^{3+} emission band at 540 nm is only 36 % of that of the bulk material. It also reveals that the red Er^{3+}, and particularly the Yb^{3+} emission, are obviously more strongly affected by particle size than the green emission. For example, for 12 nm-sized UCNPs in cyclohexane, τ_{mean} of the red Er^{3+} emission and 980 nm Yb^{3+} emission amount to 7 %, and even only 1 % of that of the bulk material. τ_{mean} of the 1,530 nm Er^{3+} band amounts to a value of about 13 %. In water, the changes are even more pronounced. Moreover, they reveal a different trend. For example, the mean DC decay lifetimes of the 12 nm-sized UCNPs in water only reach about 16 and 5 % of the values of the unquenched material for the 540 and 1530 nm emission band and only ≈ 0.6 % for the 980 nm Yb^{3+} emission, respectively. These changes were previously ascribed to efficient coupling to O-H vibrations between 3,300 and 3,700 cm^{-1}. [57, 61] τ_{mean} of the 655 nm Er^{3+} emission band, originating from the $^2F_{9/2}$ energy level, which has an energy gap of 2,900 cm^{-1} to its next lower lying energy level, is, however, barely influenced by these high energy vibrational modes, nor by the high energy modes of the C-H vibrations of the surface ligands OA and PAA. [99-101]

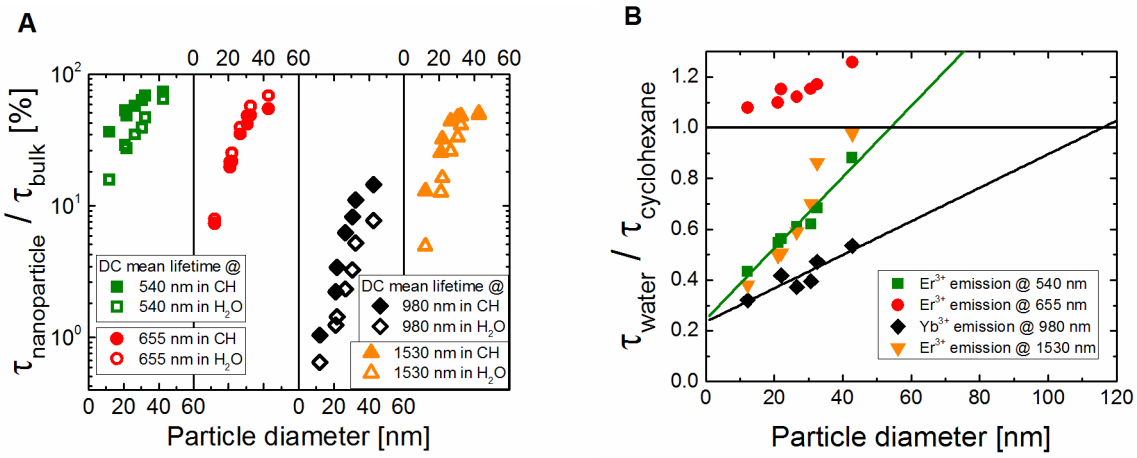

Figure 25. "**Panel A:** Mean lifetimes of the different Er^{3+} DC emission bands, displayed as percentage of the lifetimes of a 3 µm-sized $NaYF_4$: 21.4 % Yb^{3+}, 2.2 % Er^{3+} powder sample (referred as "bulk"; 540 nm: 185 µs, green; 655 nm: 520 µs, red; 1,530 nm: 8,500 µs, orange) as function of particle diameter for direct excitation of Er^{3+} at 490 nm and 380 nm, respectively, and of the Yb^{3+} emission excited at 940 nm and detected at 980 nm (2,000 µs - black). [38, 39] Full and open symbols represent UCNPs dissolved in cyclohexane (CH) and in water, respectively. **Panel B:** Ratio of the mean decay DC lifetimes of similarly sized UCNPs in water and cyclohexane as function of particle diameter for the Er^{3+} and Yb^{3+} emission bands. The ratio of lifetimes of the 540 nm Er^{3+} and the 980 nm Yb^{3+} emission were fitted to estimate a size limit at which these lifetimes become independent on UCNP environment." Reproduced with permission. [91]

An extrapolation of the linear trend of the ratio of τ_{mean} of the Er^{3+} and Yb^{3+} DC emission bands in water and cyclohexane as function of particle diameter, as shown in panel B of Figure 25, suggests the same τ_{mean} values in both solvents for UCNP sizes exceeding about 50 nm for the DC emission of Er^{3+} at 540 nm and about 115 nm for the 980 nm Yb^{3+} emission, respectively. This implies that the particle diameter where the mean decay time of the Yb^{3+} emission remains constant is roughly six times the average energy migration length of about 20 nm calculated by Fischer *et al.* for 20 % Yb^{3+} codoped $NaYF_4$ nanocrystals. [63] The smaller size limit for the green Er^{3+} luminescence could be ascribed to its way smaller doping concentration and therefore, a smaller average energy migration length. This suggests that these UCNP sizes could present a rough limit where the energy migration from the core to the surface becomes inefficient, making the luminescence dynamics of these emissions independent of UCNP diameter. τ_{mean} of the 1,530 nm emission reaches only 4,400 µs in both solvents used here, which amounts to roughly half the value of 8,500 µs reported and calculated for the lifetime of this emission for the bulk material. [47, 102] This result agrees well with the behaviour found by the researchers around *Yuan*. [47] These authors observed that τ_{mean} of the 1,530 nm Er^{3+} emission increased

significantly from 1,200 µs to 3,600 µs for particle sizes from 10 nm to 40 nm and reached 4,000 µs for 100 nm-sized UCNPs.

P-dependence of Φ_{UC}

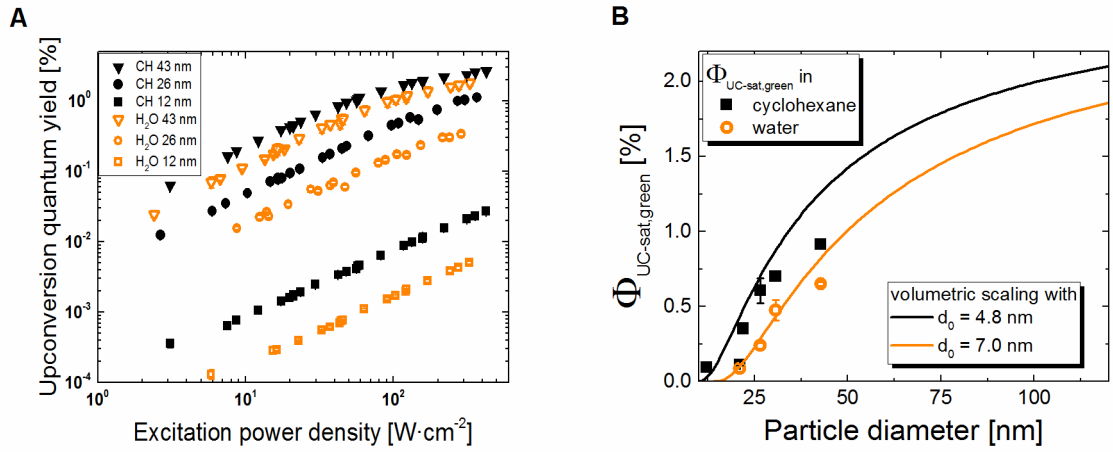

Figure 26. "**Panel A:** *P*-dependent total Φ_{UC} values of representatively chosen 12, 26, and 43 nm-sized $NaYF_4$: 20 % Yb^{3+}, 2 % Er^{3+} UCNPs in cyclohexane (full black symbols) and in water (open orange symbols), respectively. **Panel B:** Particle size-dependent saturation Φ_{UC} of the UC emission between 510-570 nm, calculated according to (eq.) 05 for the 12 to 43 nm-sized UCNPs in cyclohexane and water. The black solid line represents the values calculated with (eq.) 03, using a Φ_0 value of 2.7 % for the luminescent core and r_0 of 4.8 nm (black line; cyclohexane) and r_0 = 7 nm (orange line; water) for the radius of the dark surface layer in cyclohexane (black line) and water (orange line), respectively, all taken from the literature." [38, 54] Reproduced with permission. [91]

The *P*-dependencies of the total Φ_{UC} ($\Phi_{UC}(P)$) were determined considering all UC photons that are emitted in the wavelength region of 400-860 nm [38] in both solvents to quantify the UCL efficiency of the UCNPs. They are exemplarily displayed for the 12, 26 and 43 nm-sized UCNPs in panel A of Figure 26. As follows from this panel, the shape of these plots in different environments is identical for all samples as previously observed for 23 nm-sized UCNPs. [57] These data clearly reflect a loss in UC emission intensity with decreasing particle size. For example, the total Φ_{UC} values of the smallest and largest particles of this UCNP series in cyclohexane vary by a factor of about 260 for *P* below 100 $W \cdot cm^{-2}$. A more detailed analysis of the individual UCL bands at low *P* again reveals the strongest influence of the particle size on the 655, followed by the 540 and 810 nm UCL bands with respective factors of 800, 250 and 27. An increase in *P* results in a partial compensation of UCL quenching. For example, the Φ_{UC}

values of the smallest UCNPs in cyclohexane at P of 430 W·cm^{-2} are nearly identical with those resulting for the largest UCNPs of our size series at a P of 1 W·cm^{-2}.

In water, the total Φ_{UC} values of the largest and smallest UCNPs vary by a factor of even about 560 for P below 100 W·cm^{-2}. A more detailed analysis of the individual UCL bands at low P reveals the strongest influence of the particle size on the 655, followed by the 540 and 810 nm UCL bands with respective factors of now 1,750, 1,300 and 60. A comparison of the total Φ_{UC} values of similarly sized UCNPs in environments with and without O-H bonds yields quenching factors of two for the largest and four for the smallest UCNPs. This can be mainly ascribed to the decreased emission intensities at 540 nm, which are for the smallest UCNPs around 11-times smaller in water than in cyclohexane. Also in water, partial compensation of UCL quenching by high P is feasible, *e.g.*, the Φ_{UC} values of the 43 nm-sized UCNPs in water and cyclohexane are nearly identical for P of 330 and 120 W·cm^{-2}, respectively.

The results from the previous quantitative UCL studies with 25 and 23 nm-sized UCNPs that were provided from two different research groups with slightly varying dopant ion concentrations fit very well in this size series. [38, 57] A more comprehensive comparison with other literature values, however, reveals considerable differences even for UCNPs of the same host matrix and doping concentration in the same environment. [38, 41, 46, 63, 103, 104] For example, this study yielded Φ_{UC} (540 nm, 150 W·cm^{-2}) = (0.32 ± 0.05) % for 31 nm-sized particles in cyclohexane, while *Boyer et al.* measured only Φ_{UC} (540 nm, 150 W·cm^{-2}) = (0.10 ± 0.05) % for 30 nm-sized UCNPs. [41] The observed limited comparability of Φ_{UC} data is ascribed to a mixture of effects originating from different measurement conditions, such as excitation beam profile, [38, 105] uncertainties in the challenging determination of P, the characterization of the spectral responsivity of the excitation channel of the setup used, and material-related factors, originating from different particles batches. [40]

Theoretical analysis of UC performance

Not only the performance of the emitting Er^{3+}, but also that of the absorbing Yb^{3+} ions is strongly influenced by UCNP size and environment. This hampers the comparability of unsaturated Φ_{UC} values of UCNPs with different particle diameters. It was therefore chosen to com-

pare the material- and environment-specific saturation quantum yield ($\Phi_{UC\text{-}sat,green}$) and the balancing power density ($P_{balance}$) values, *i.e.*, the power density where $\Phi_{UC} = \Phi_{UC\text{-}sat,green} / 2$ by fitting $\Phi_{UC}(\lambda_{em} = 510\text{-}570\ nm,\ P)$ of our UCNP size series with (eq.) 05. Note that for Yb^{3+}, Er^{3+} codoped UCNPs, this model is only valid for the 540 nm UCL and not for the other UC emission bands. The results of these fits in cyclohexane and water show strong size- and environment-related changes. For example, for 21 nm-sized UCNPs, the $P_{balance}$ values increase by more than two orders of magnitude relative to the bulk material in cyclohexane and by even over more than three orders of magnitude in water. The size-dependences of the $\Phi_{UC\text{-}sat,green}$ values of the green emission are summarized in panel B of Figure 26. These values of the 21 nm-sized UCNPs change by roughly two orders of magnitude in both solvents. The stronger influence in the size and environment dependence on $P_{balance}$ can be ascribed to the stronger influence of the size- and environment-related quenching of excited Yb^{3+} ions, which is in agreement with the previously discussed decay kinetics of the Yb^{3+} and Er^{3+} ions.

The $\Phi_{UC\text{-}sat,green}$ values obtained for our UCNP size series were thus correlated with the particle volume, thereby considering average distances of energy migration from electronically excited Ln^{3+} ions located in the core and in a surface-near region prone to quenching by ligand and solvent molecules with high energy vibrations, assuming a homogeneous dopant concentration within the particles. The thickness of this strongly quenched, or even dark, surface region depends on the coupling efficiency of the quenching vibrational modes with the respective energy levels of Yb^{3+} and Er^{3+} ions and can hence vary for different emission bands. As discussed in *section 2.2.2*, similar approaches have been reported by other groups. [48, 54, 58] (Eq.) 03 was subsequently used for the volumetric scaling. However, since more data points between 40 nm and 3 µm are needed to obtain a reasonable fit of the volumetric-scaling model with the size-dependent $\Phi_{UC\text{-}sat,green}$, we used literature values to test if the $\Phi_{UC\text{-}sat,green}$ values for UCNP sizes between 12 and 43 nm can be qualitatively reproduced with this model. More precisely, 4.8 nm was used as the radius of the dark surface layer, calculated for 27x56 nm-sized $NaYF_4$: 17 % Yb^{3+}, 3 % Er^{3+} UCNPS dispersed in toluene, [54] and 2.7 % was used as Φ_0, calculated for the saturated Φ_{UC} value of the green emission of 3 µm-sized $NaYF_4$: 21.4 % Yb^{3+}, 2.2 % Er^{3+} UC particles. [38] The results in panel B of Figure 26 agree reasonably well with the $\Phi_{UC\text{-}sat,green}$ values of the 12 to 32 nm-sized UCNPs in cyclohexane, yet not perfectly. Note that at the beginning of this study smaller $\Phi_{UC\text{-}sat,green}$ values were obtained for core-shell UCNPs with same

core and shell doping, which could at least partly explain the differences for the theoretical and experimental $\Phi_{UC\text{-}sat,green}$ value for the 43 nm-sized UCNPs. To reproduce our $\Phi_{UC\text{-}sat,green}$ values in water, clearly a larger radius of the dark shell of r_0 of 7 nm has to be assumed. As displayed in panel B of Figure 26, this model therefore provides $\Phi_{UC\text{-}sat,green}$ values of about 2.1 and 1.8 % for the UCNPs in cyclohexane and water at the roughly predicted size limit for quenching of 115 nm extracted from the lifetime measurements detailed in the previous section. These values amount, however, to only 78 and 66 % of the $\Phi_{UC\text{-}sat,green}$ value of the bulk material. These differences could originate from the fact that for the luminescence decay behaviour only the emission of UC photons plays a role, whereas both the absorption and emission contribute to Φ_{UC}. This could also explain the relatively small changes that were observed for the population dynamics of UCNPs with sizes > 26 nm for comparable P, *e.g.* in all panels of Figure 22, and yet relatively large changes for the Φ_{UC} values of the UCNPs that are bigger than 26 nm, *e.g.* in both panels of Figure 26.

4.2 Influence of doping concentration in core-shell structure

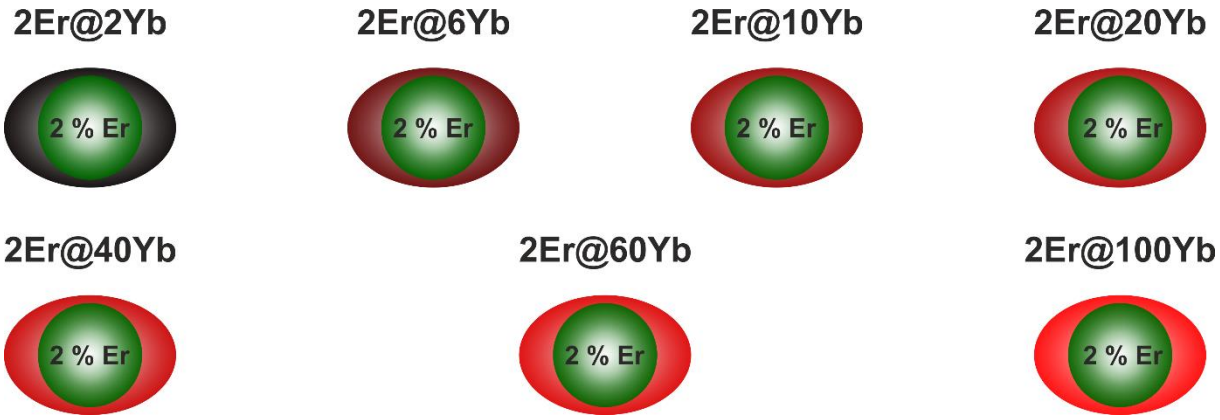

Figure 27: Schematic representation of the core-shell UCNP samples that were investigated in this study.

One approach to overcome the losses in UC efficiencies is to spatially separate the sensitizer and activator ions in multishell particle architectures in combination with surface passivation or shielding shells. A joint study with the research group of Professor Zhang from the National University of Singapore explored the effect of different UCNP core-shell designs on the spectroscopic properties. More specifically, those designs separated the Yb^{3+} and Er^{3+} ions, while respectively confining them into the core and shell of the nanoparticle. [67] This study is an extension of the previous one and focuses on the spectroscopic properties of UCNPs with a defined doping concentration of 2 % Er^{3+} in the $NaYF_4$ particle core and 2-100 % Yb^{3+} in the $NaYF_4$ shell. The UCNPs are subsequently denoted by the names "**2Er@z_{Yb}Yb**", with the number z_{Yb} representing the Yb^{3+} doping concentration in the particle shell. A schematic representation of all investigated UCNP samples from this study is given in Figure 27.

4.2.1 UCNP preparation

As a prerequisite for this study, our cooperation partners synthesised seven different batches with varying z_{Yb} values between 2 and 100. The final UCNPs were synthesized through a two-step synthesis using a modified version of a previously reported protocol for each step. [106] Briefly, the first step consisted of the synthesis of the particle core and the second step of the synthesis of the shell around the core UCNPs.

4.2.2 Structural and chemical analysis

XRD measurements revealed that this synthesis procedure in general yields hexagonal $NaYF_4$ nanocrystals. [67] The size distributions of the $NaYF_4$: 2 % Er^{3+} core-only and six 2Er@z_{Yb}Yb core-shell UCNPs (z_{Yb} = 6, 10, 20, 40, 60 and 100), were investigated via TEM measurements. They revealed a spherical shape of the core-only and cylindrical rod-like shapes of the monodisperse core-shell UCNPs. The size distributions of the UCNPs, evaluated for more than 100 particles, reveal particle sizes of around 20 nm for the spherical core-only and (23x33) nm for the rod-shaped cylindrical core-shell UCNPs. This amounts to respective contributions of the particle core and shell of 30.6 and 69.4 % to the overall volume of around 13,711 nm^3 per nanoparticle, which is comparable to the volume of 30 nm-sized spherical core-only UCNPs. The shell has a volume of 9,515 nm^3, and is therefore the host of around 133,391 Ln^{3+} ions (calculated with the volume of one $NaYF_4$ unit cell of 0.107 nm^3 and the average number of 1.5 Ln^{3+} ions per unit cell). [33, 107] Lastly, an additional batch of core-shell UCNPs was synthesized with a composition of 2Er@2Yb. All analytical measurements were done in Singapore.

4.2.3 Spectroscopic analysis

The influence of z_{Yb} on the UC colour, efficiency and the respective (de)population pathways was subsequently investigated by me via their absolute *P*-dependent UC spectra of the respective UCNPs, which were recorded with the integrating sphere setup previously reported. [38, 57, 86] A further analysis of the decay kinetics was recorded with the spectrometers that were mentioned in *section 3.2.2*.

Upconversion luminescence

An overview of the influence of z_{Yb} on the respective spectroscopic properties can be gained by a view on the respective UC spectra. Panel A of Figure 28 therefore displays the normalized UC spectra of the 2Er@z_{Yb}Yb (z_{Yb} = 6, 10, 20, 40, 60 and 100) UCNPs at an exemplarily chosen *P* of 40 $W \cdot cm^{-2}$ (normalized to the respective absorption value in the integrating sphere). Panel B displays their *P*-dependent Φ_{UC} values between 500-860 nm. The UCL and Φ_{UC} values of the 2Er@2Yb core-shell UCNPs are not included in Figure 28, as the sample concentration was too low for a measurement of their absolute values in the integrating sphere. Furthermore, the UCLs in Figure 28 are only displayed between 500-860 nm. The UCL at 410 nm accounts to less than 2 % of all UC photons and is subsequently neglected in the further discussion.

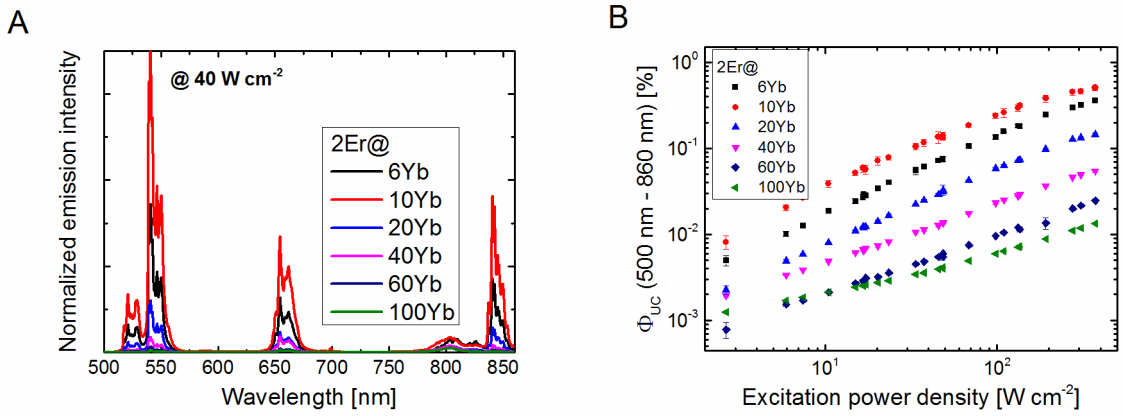

Figure 28: Normalized UCL (to the respective absorption value in the integrating sphere - **panel A**) at an exemplarily chosen P of 40 W·cm^{-2} and Φ_{UC} values of the integrated UCL between 500-860 nm (**panel B**) of the core-shell 2Er@z_{Yb}Yb (z_{Yb} = 6, 10, 20, 40, 60 and 100) UCNPs.

Both panels in Figure 28 show a clear dependence of the spectroscopic properties on z_{Yb}, revealing the highest UCL values for the 2Er@10Yb and the lowest for the 2Er@100Yb UCNPs at all P applied. The emission intensities integrated between 500-860 nm and measured at P = *40 W·cm^{-2}* of the 2Er@10Yb UCNPs are around 38-times higher than the ones from the 2Er@100Yb UCNPs. A further comparison of the integrated emission intensities shows uneven ratios for the respective emission bands at 540, 655 and 810 nm of respectively 136, 47 and 5 for these two UCNP samples. Panel B of Figure 28 furthermore shows slightly different slopes of the Φ_{UC} values versus P in the log-log plot, resulting in Φ_{UC}(2Er@10Yb, P) / Φ_{UC}(2Er@z_{Yb}, P) ratios between (1.4-2.2) and even (7-45). This indicates a considerable influence of the shell doping concentration on the competition between the ETU rates from the Yb^{3+} sensitizer to neighbouring Er^{3+} activator ions, the depopulation processes of the excited Er^{3+} ions and the non-radiative decay pathways.

Emission colour

These competing processes result in different population densities of the respective emissive Er^{3+} energy levels. This is reflected in the P-dependent relative photon fluxes of the UCL bands between 510-570, 630-685 and 783-833 nm, which are calculated according to (eq.) 07 and are displayed in Figure 29 for all UCNP samples. The UCL between 833-860 nm originates from the same energy level as the more pronounced UCL between 510-570 nm and is therefore not regarded in the subsequent discussion. This image shows an increase of the relative photon fluxes between *510-570 nm* while increasing the z_{Yb} values from 2 to 10, and a subsequent

decrease for higher values at all P applied. The corresponding relative photon fluxes are also displayed in panel A of Figure 30 at an exemplarily chosen low P of 40 W·cm^{-2}, revealing values of *e.g.*, 32, 50 and 13 %, for the UCNPs with z_{Yb} values of 2, 10 and 100 respectively. The relative photon fluxes of this UCL band additionally increase with increasing P for all samples, except for the 2Er@10Yb sample, where it remains nearly constant.

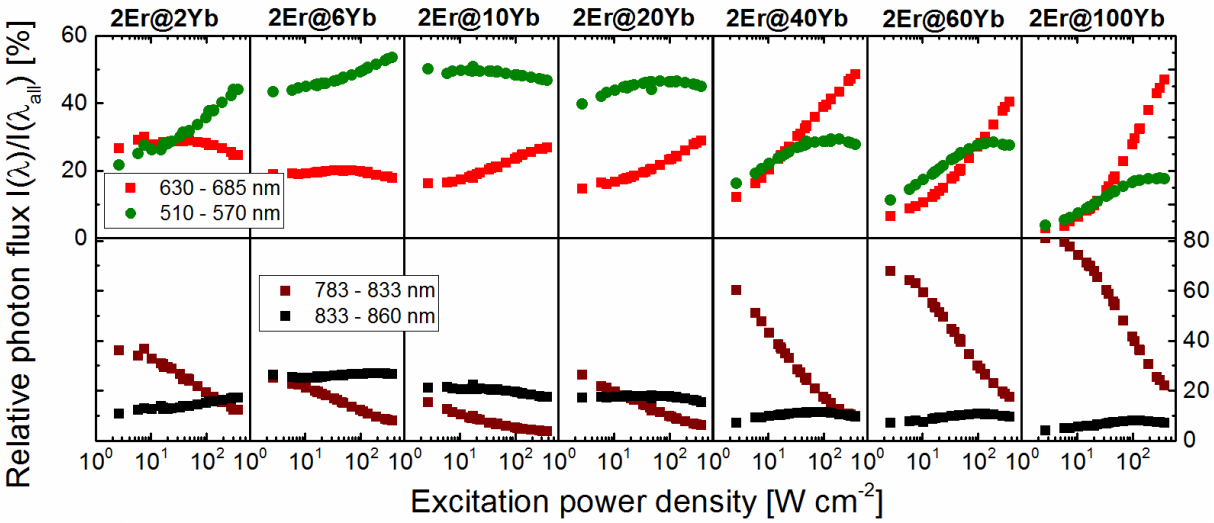

Figure 29: Relative spectral photon flux of the UCL between 510-570, 630-685, 783-833 and 833-860 nm, compared to the overall UCL between 400-860 nm, for the core-shell 2Er@z_{Yb}Yb UCNPs (z_{Yb} = 6, 10, 20, 40, 60 and 100).

The relative photon fluxes of the UCL between *630-685 nm* show a different trend. Noteworthy is, that the P-dependent behaviour of their relative photon fluxes in Figure 29 strongly deviates for the different Yb^{3+} doping concentrations. The relative photon flux remains nearly independent of P for $z_{Yb} < 10$ and subsequently rises with increasing P for higher z_{Yb} values. Its slope versus P is even higher than the one from the 510-570 nm UCL band, making it the dominant UCL band for very high P values for $z_{Yb} \geq 40$, as displayed in panel B of Figure 30. However and despite this trend, the relative photon fluxes of this UCL band still show a decreasing behaviour at low P versus z_{Yb}. The corresponding values at the exemplarily chosen low P of 40 W·cm^{-2} are around 29, 20 and 15 % for UCNPs with z_{Yb} values of 2, 10 and 100.

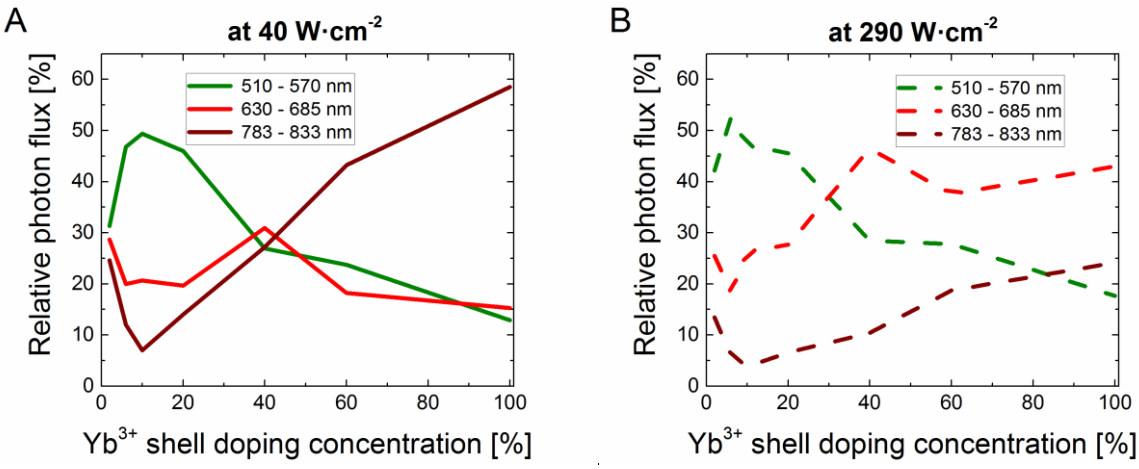

Figure 30: Relative photon flux of the 510-570, 630-685 and 783-833nm UC emission bands versus Yb^{3+} shell doping concentrations z_{Yb} for an exemplarily chosen low *P* of 40 W·cm^{-2} (**panel A** - solid lines) and an exemplarily chosen high P of 290 W·cm^{-2} (**panel B** - dotted lines).

The *P*- and z_{Yb}-dependent relative photon fluxes between *783-833 nm* again show a different trend than the ones between 510-570 nm. For example, they always decrease with increasing *P*, as shown in Figure 29, yet reveal a different behaviour with increasing z_{Yb}. They furthermore follow the complete opposite trend at high and low *P*, as shown in panels A and B Figure 30, *i.e.*, decreasing values for $z_{Yb} < 10$ and increasing relative photon fluxes for higher values. The corresponding relative photon fluxes for this UCL band for $z_{Yb} = 2$, 10 and 100 at 40 W·cm^{-2} are around 25, 7.0 and 59 %. This decreasing trend for $z_{Yb} < 10$ and increasing trend for higher z_{Yb} values even leads to the fact that it outclasses all other UCL bands at this exemplarily chosen low *P* for $z_{Yb} > 40$, making it the dominant UCL band under these conditions, which it never does at high *P* values.

Obviously for $z_{Yb} < 40$ most of the UC photons are emitted from the $^2H_{11/2}/^4S_{3/2}$ energy levels at high and low *P*, from the lower $^4F_{9/2}$ energy level at high *P* for $z_{Yb} > 40$ and from the even lower $^4I_{9/2}$ energy level at low *P* for $z_{Yb} > 40$. As the only occurring changes are the alteration of the concentrations of Yb^{3+} ions in the shell and not of Er^{3+} ions in the core, these observations can be ascribed to an interplay of both decreasing distances between sensitizer and activator ions, and hence higher ETU rates, and increased losses at the particle surface.

Time resolved measurements

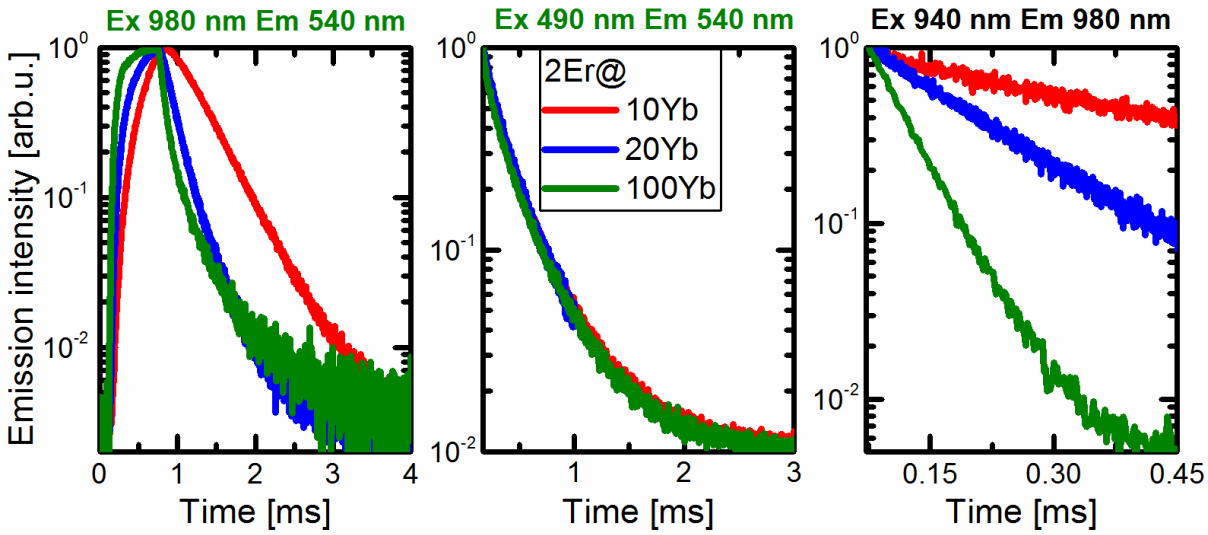

Figure 31: Decay kinetics of three representative core-shell $NaYF_4$: 2 % Er^{3+}@$NaYF_4$: z_{Yb} % Yb^{3+} (z_{Yb} = 10, 20 and 100) UCNP samples with respective excitation and emission wavelengths of (λ_{ex} = 980 nm, λ_{em} = 540 nm), (λ_{ex} = 490 nm, λ_{em} = 540 nm) and (λ_{ex} = 940 nm, λ_{em} = 980 nm) for the left, middle and right image.

This is also reflected in the temporal behaviour of the UCNPs. Figure 31, *e.g.*, exemplarily displays the decay kinetics of the Er^{3+} emission band at 540 nm, one time upon 980 (left) and another time upon 490 nm excitation (middle), and of the Yb^{3+} emission band at 980 nm upon 940 nm excitation (right) for three exemplarily chosen UCNP samples with respective z_{Yb} values of 10, 20 and 100. This figure clearly shows a considerable influence of z_{Yb} on the decay kinetics of the emission band at 540 nm, however, this is not because of altered decay components from the $^2H_{11/2}/^4S_{3/2}$ Er^{3+} energy level, but only because of an altered decay behaviour of the 980 nm $^2F_{5/2}$ Yb^{3+} energy level.

Slope factors

Another parameter that gives valuable information about the population behaviour of the respective UCL band is the slope factor *n(P)* of the log-log plot from its respective emission intensity versus excitation power. They were calculated using (eq.) 02, smoothed with a Savitzky-Golay filter and displayed for exemplarily chosen high and low *P* in panel A of Figure 32 for the UCL band between 510-570 nm and in panel B for the one between 630-685 nm. For example, $n_{540\ nm}$ at 40 $W \cdot cm^{-2}$ shows values around two for all z_{Yb} values, substantiating the typically assumed two-photonic population pathway of the $^2H_{11/2}/^4S_{3/2}$ energy level. Increasing

P to *e.g.*, 290 W·cm^{-2} results in a diminution of $n_{540\ nm}$ to values between 1.8 and 1.6 for all samples, except the 2Er@10Yb sample, where $n_{540\ nm} \approx 1.4$. This indicates a similar partial saturation of the lower Er^{3+} energy levels at this high *P* for all samples.

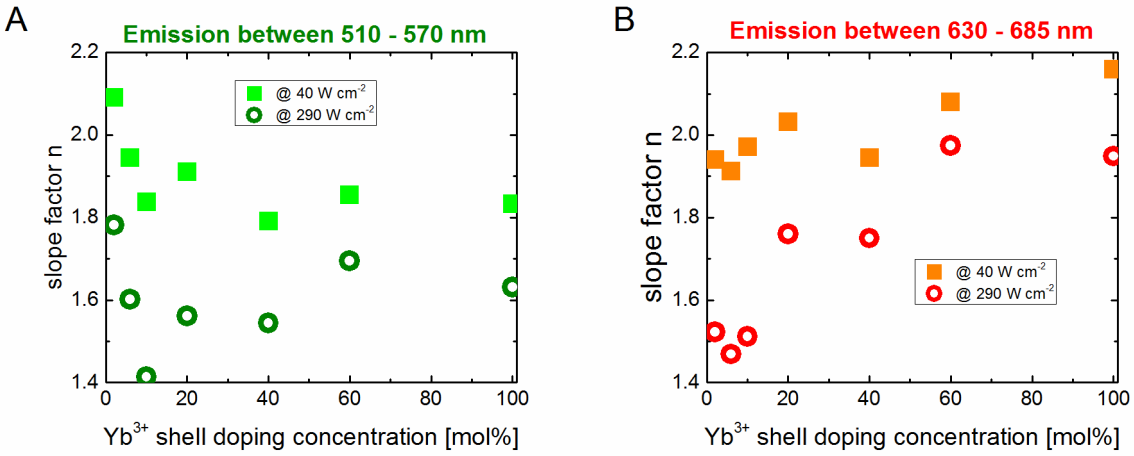

Figure 32: Smoothed slope factor values *n* (using a Savitzky-Golay filter) of the Er^{3+} bands between 510-570 nm (**panel A**) and 635-680 nm (**panel B**) of the core-shell UCNPs, respectively displayed at 40 (closed symbols) and 290 W·cm^{-2} (open symbols) versus the respective Yb^{3+} doping concentration in the particle shell.

$n_{655\ nm}$ shows a different behaviour, *i.e.*, rising values for z_{Yb} values increasing from 1.9 to 2.2 for a relatively low *P* of *e.g.* 40 W·cm^{-2} and from even 1.4 to 2.0 for a relatively high *P* of *e.g.* 290 W·cm^{-2}. This underpins a partial contribution of triphotonic pathways to the population of the $^4F_{9/2}$ energy level, including the ($^4G_{11/2} \rightarrow {}^4F_{9/2}$; $^2F_{7/2} \rightarrow {}^2F_{5/2}$) BET step. This contribution, however, is only visible for the UCNPs with $z_{Yb} > 10$. Below that threshold, the $^4F_{9/2}$ energy level is populated by biphotonic processes only, namely via MPR processes from the $^2H_{11/2}/{}^4S_{3/2}$ energy level as indicated by our previous studies (see also *section 4.1.3, subsection population pathways of the red Er^{3+} level*). This explains the similar slope factors for the UCL bands at 540 and 655 nm under these conditions.

Φ_{UC} at saturation and brightness

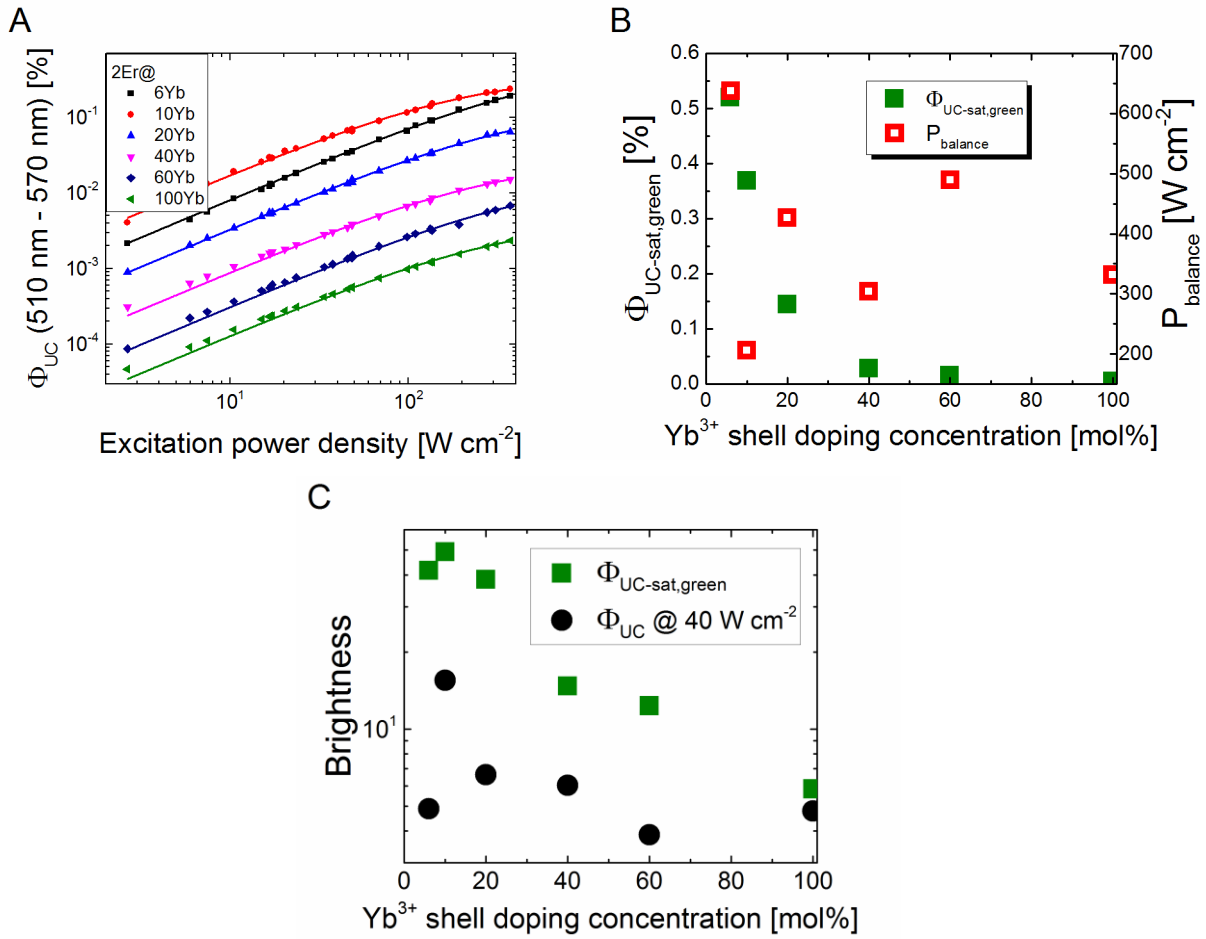

Figure 33: Panel A: Φ_{UC} values of the integrated UCL between 510-570 nm for the core-shell $NaYF_4$: 2 % Er^{3+}@$NaYF_4$: z_{Yb} % Yb^{3+} (z_{Yb} = 6, 10, 20, 40, 60 and 100) UCNPs. The solid lines represent the respective fits with (eq.) 05. **Panel B:** Saturation quantum yield and balancing power values, calculated with (eq.) 05 from the Φ_{UC} values between 510-570 nm from panel A, displayed versus the respective Yb^{3+} shell doping concentration. **Panel C:** Brightness values of the green emission at saturation and of the overall UCL between 500-860 nm at 40 $W \cdot cm^{-2}$, calculated using (eq.) 04.

The different slopes of the Φ_{UC} values versus P in the log-log plot in panel B of Figure 28 suggest, that the z_{Yb} values yielding the most efficient UCNPs regarding the size of UCL differ for the P values used in this study and P values at saturation. I therefore exemplarily calculated the saturation quantum yields of the two-photonic UCL band at 540 nm ($\Phi_{UC\text{-}sat,green}$) and the balancing power densities according to (eq.) 05. The respective fits with this equation are displayed in panel A of Figure 33 for all samples, while panel B displays the resulting $\Phi_{UC\text{-}sat,green}$ and $P_{balance}$ parameters versus z_{Yb}. The results reveal an inverse relation between $\Phi_{UC\text{-}sat,green}$ and

z_{Yb}, with the highest $\Phi_{UC\text{-}sat,green}$ value of about 0.5 % now being reported for z_{Yb} = 6 and the lowest one for z_{Yb} = 100. This trend clearly reflects that the population densities of the $^4S_{3/2}$ / $^2H_{11/2}$ Er^{3+} energy levels of *e.g.*, the 2Er@6Yb UCNPs are obviously greater than the ones of the 2Er@100Yb UCNPs. This is especially noteworthy as the 2Er@100Yb UCNPs have a significantly higher amount of absorbing sensitizer ions per nanocrystal. One possible explanation for this behaviour is, that rather than transferring their energy to the Er^{3+} ions, the energy migrates among the Yb^{3+} ions and eventually recombines non-radiatively at the particle surface. The $P_{balance}$ values reveal a different trend of alternating decreasing and increasing values. At very high *P*, the highest Φ_{UC} values of such nanostructures can therefore be expected at very low z_{Yb} values, which is contrary to the results at lower *P*.

Nevertheless, the 2Er@6Yb UCNPs do not necessarily need to be the ones that convert the highest amounts of incoming photons into UC photons at high *P*, as they contain the lowest amount of absorbing sensitizer ions. Their brightness *B* is therefore a better parameter for the comparison among similar-sized UCNP architectures with different absorption cross-sections. It was subsequently calculated according to (eq.) 04 for saturated efficiency values of the 510-570 nm UCL, and at a low *P* of 40 $W \cdot cm^{-2}$ for the overall UCL between 500-860 nm. The corresponding values are displayed in panel C of Figure 33, revealing that the 2Er@10Yb UCNPs are the brightest ones at all *P* applied. Interestingly, $B(z_{Yb} = 100, P)$ is even around eight times lower for saturated Φ_{UC} values and still around three-times lower at 40 $W \cdot cm^{-2}$, compared to the UCNPs with ten times less absorbing sensitizer ions in the particle shell.

4.2.4 Comparison with conventional UCNPs

But how do these (23x33) nm-sized rod-like UCNPs compare to other nanostructures, such as typical $NaYF_4$: 20 % Yb^{3+}, 2 % Er^{3+} codoped UCNPs? A comparison with the 31 nm-sized UCNPs from *section 4.1*, which have a similar particle volume as the core-shell UCNPs from this study, reveals a considerably higher brightness for the typical codoped UCNPs. They are, *e.g.*, around six-times higher for the green UCL band for saturated values, and even around 11-times higher for the overall UCL between 500-860 nm at 40 $W \cdot cm^{-2}$, compared to $B(z_{Yb} = 10)$ from this study.

4.3 Influence of Tm^{3+} doping concentration

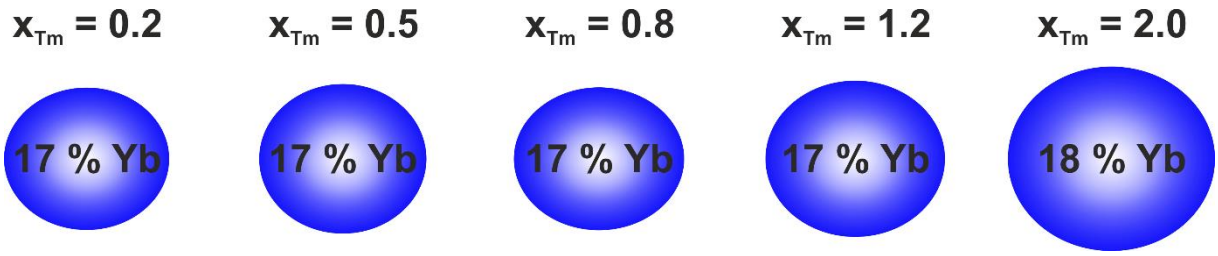

Figure 34: Schematic representation of the UCNP samples that were investigated in this study.

As stated in *section 2.3*, another question that received a lot of attention in the literature, yet is still not completely understood and agreed upon, are the (de)population dynamics of Yb^{3+}, Tm^{3+} codoped upconverting crystals. This becomes especially clear by the existence of many different publications that are discussing rate equations for Tm^{3+} doped and Yb^{3+}, Tm^{3+} codoped systems and who propose different (de)population pathways. [37, 68-70, 72-75, 108-119] The accordingly lack of a single compelling model that can be used to predict the spectroscopic properties of Yb^{3+}, Tm^{3+} codoped systems under various conditions, such as *P* and doping concentration, combined with the lack of sufficient experimental data that report optimal Yb^{3+}, Tm^{3+} doping concentrations yielding the highest upconversion efficiencies of the various Tm^{3+} energy levels, consequently motivated us and the research group of Professor Soukka from the University of Turku to perform a Tm^{3+} doping concentration (x_{Tm})- and *P*-dependent study of the Φ_{UC} and UCL of uniformly sized, monodisperse UCNPs. The results are also submitted to publication in Ref. [120]. A schematic representation of the UCNP samples that were investigated in this study is given in Figure 34.

4.3.1 UCNP preparation

As a prerequisite for this study, our cooperation partners synthesized a series of five UCNP batches using a previously reported protocol, only varying the amounts of rare earth chloride hexahydrates. [121] The amounts of the respective rare earth chlorides were chosen to yield UCNPs with doping concentrations of 20 % Yb^{3+} and x_{Tm} % Tm^{3+} (x_{Tm} = 0.2, 0.5, 0.8, 1.1 and 2.0). For the analytical measurements of the respective UCNPs an aliquot of the as-prepared UCNPs was dried and used as powder sample while the rest were dispersed in toluene as OA ligand-stabilized suspension.

4.3.2 Structural and chemical analysis

Our cooperation partners subsequently performed a XRD pattern analysis, which revealed a pure hexagonal crystal phase for all five batches, while a TEM analysis indicated the monodispersity of all UCNPs with average particle diameters of (36.0 x 40.5), (30.5 x 35.1), (27.9 x 33.3), (29.2 x 32.7) and (27.8 x 32.3) nm for (width x length) of the $NaYF_4$: 20 % Yb^{3+}, x_{Tm} % Tm^{3+} UCNPs with x_{Tm} = 0.2, 0.5, 0.8, 1.1 and 2.0, respectively. The respective doping concentrations were investigated via ICP-OES measurements by my colleague Melissa-Jane Monks, revealing slightly lower Yb^{3+} concentrations between 16 and 18 %, yet closely matching Tm^{3+} concentrations of x_{Tm} = 0.16, 0.49, 0.83, 1.19 and 2.04.

4.3.3 Spectroscopic analysis

The influence of x_{Tm} on the UC colour, efficiency and the (de)population pathways of the respective Yb^{3+}, Tm^{3+} ions was subsequently investigated by me for the oleate-capped UCNPs with our custom build integrating sphere setup as previously reported. [38, 57, 86] Special attention was dedicated to quantitative UCL measurements, using well-calibrated setups and well-defined beam profiles, covering several orders of magnitude of *P*. The decay kinetics were recorded with the spectrometer and the parameters that were outlined in *section 3.2.2.*

UCL at low *P*

An overview of the influence of the Tm^{3+} doping concentration on the respective spectroscopic properties can be gained by a look on the respective UC spectra. Panel A of Figure 35 therefore shows the normalized UC emission spectra of all five UCNP batches upon 980 nm excitation, representatively displayed at a low *P* of 40 $W \cdot cm^{-2}$, which is typically used in bioassays. [94-96] Their UCL bands were highlighted in panel A. Panel B displays the respective Tm^{3+}-Tm^{3+} transitions and corresponding emission wavelengths with the highest UC intensity. The additional weak UCL between 535-560 nm was attributed to Er^{3+} impurities and neglected in the further discussion. The UCL band at 800 nm originates from the $^3H_4$, the band at 700 nm from the $^3F_3$, the UCL bands at 650 and 475 nm from the $^1G_4$, the UCL bands at 782, 744, 445 and 375 nm from the $^1D_2$ and the UCL band at 345 nm from the $^3P_6$ Tm^{3+} energy level. These UCL bands will henceforth only referred with the energy levels from where they originate. The UCL spectra reveal strong dependencies on the Tm^{3+} doping concentrations. For example, the UCL bands from the $^1G_4$, $^1D_2$ and $^3P_6$ Tm^{3+} energy levels are strongest for the $NaYF_4$: 17 % Yb^{3+}, 0.5

% Tm^{3+} codoped UCNPs, while the UCLs from the $^3H_4$ and $^3F_3$ Tm^{3+} energy levels are strongest for the $NaYF_4$: 17 % Yb^{3+}, 1.2 % Tm^{3+} codoped UCNPs.

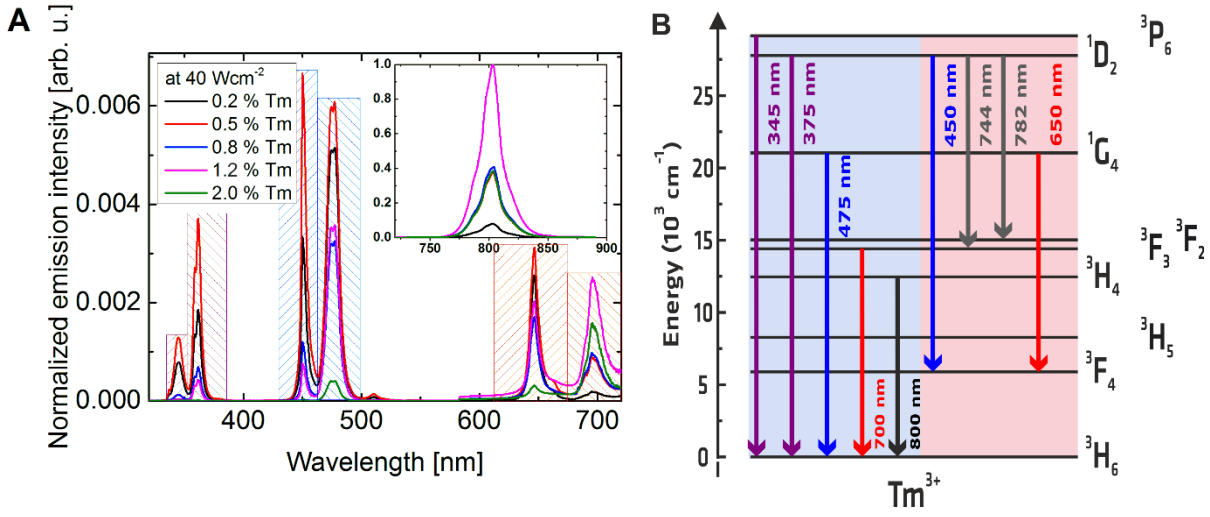

Figure 35: **Panel A:** UCL (normalized to absorption) of β-$NaYF_4$: 20 % Yb^{3+}, x_{Tm} % Tm^{3+} ($x_{Tm} \approx$ 0.2, 0.5, 0.8, 1.2 and 2.0) UCNPs between 320-720 nm in a scale from 0 to 0.007. The UCL in the UV-, blue- red-emission region are highlighted in violet, blue and red, respectively. The inset shows the stronger emission between 720-900 nm in a scale from 0 to 1. **Panel B:** Energy level diagram of Tm^{3+} ions. The solid lines represent the respective UC emission, while the number next to it represents the centre wavelength of the respective transition.

Upconversion efficiencies

The *P*-dependences of the doping dependent UC performances of these nanocrystals are subsequently displayed panel A of Figure 36 from a *P*-region that is typically used for bioimaging purposes to the *P*-region where Φ_{UC} values of Tm^{3+} based UCNPs are known to saturate. [37, 50, 73, 75] The results again show that the $NaYF_4$: 17 % Yb^{3+}, 1.2 % Tm^{3+} codoped UCNPs convert the highest amount of absorbed into emitted photons in the wavelength region between 330 and 860 nm for all *P* applied. More precisely, this image also reveals a different slope of the Φ_{UC} values versus *P*, resulting in $\Phi_{UC}(x_{Tm}, P)$ / $\Phi_{UC}(0.2, P)$ ratios between (1.8 and 4.4), (1.7 and 6.7), (4.1 and 12) and (1.9 and 4.7), respectively for x_{Tm} = 0.5, 0.8, 1.2 and 2.0. The highest observed values were even as high as $\Phi_{UC}(x_{Tm} = 1.2, P = 270\ W{\cdot}cm^{-2}, \lambda_{em} = 330\text{-}860\ nm)$ = (10.3 ± 0.3) %. This is the highest Φ_{UC} value that, to the best of our knowledge, has been so far reported for Yb^{3+}, Tm^{3+} based UCNPs. However, this is only because most of the other research groups do not include the strong UCL band at 800 nm, or only report values at a lower *P*. [37, 50, 73, 75, 122, 123] A more detailed comparison of the reported *P*-dependent Φ_{UC}

values from the literature and the *P*-dependent Φ_{UC} values from this work in wavelength regions between (350-850), (775-825), (450-900) and (470-750) nm reveals comparable values for UCNPs among each other, and values that are more than three-times smaller than the ones that were reported for µm-sized Yb^{3+}, Tm^{3+} codoped upconverting crystals (for more details see also panels B-D of Figure 36**)**. Note that the values of the µm-sized particles had to be converted from the power conversion efficiency to Φ_{UC}. This conversion was done by taking into account the photon energies of the emission bands at 475 and 655 nm and of the absorption band at 980 nm.

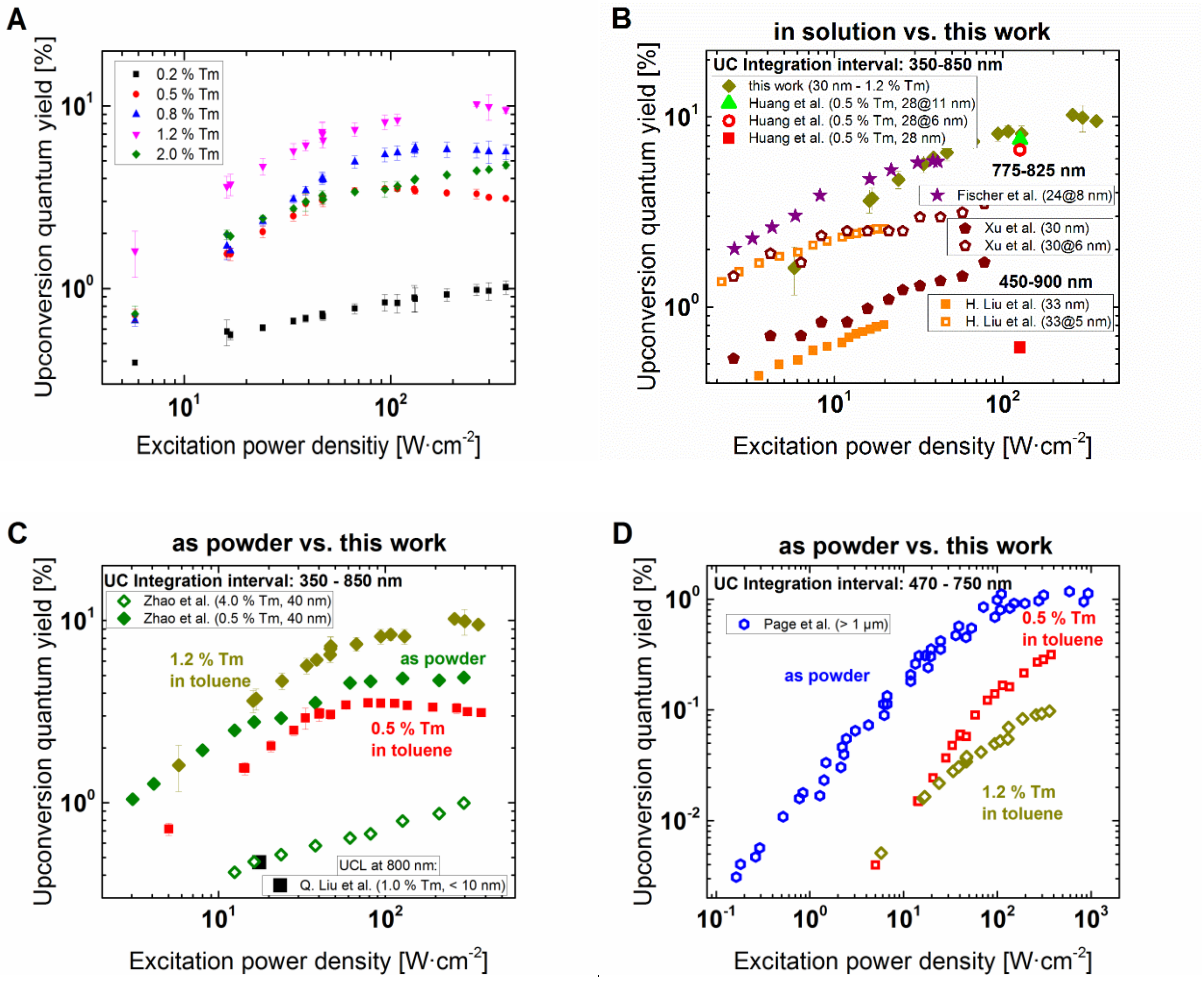

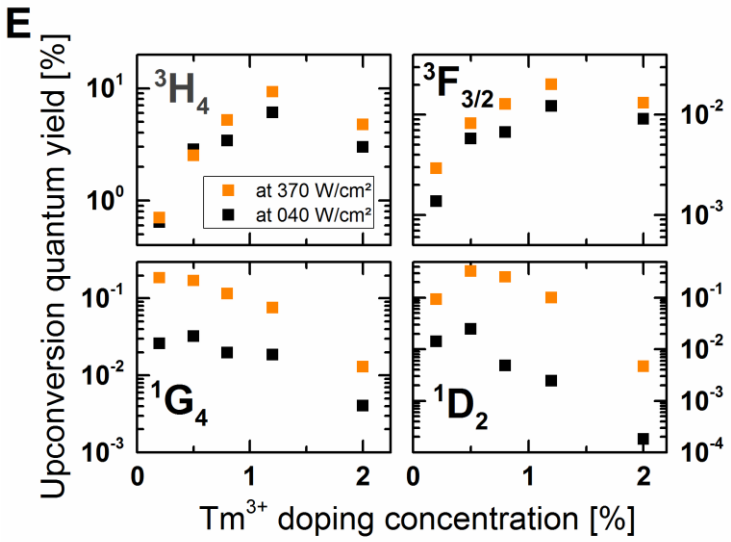

Figure 36: Panel A: Φ_{UC} values between 320-900 nm for all UCNPs; $\Phi_{UC}(\lambda_{em} = 350\text{-}850\ nm)$ values of the 20 % Yb^{3+}, 1.1 % Tm^{3+} $NaYF_4$ UCNPs, compared to literature values, measured in various solutions (**panel B**) and as powder samples (**panel C**). Panel B also shows the $\Phi_{UC}(\lambda_{em} = 350\text{-}850\ nm)$ values of the 20 % Yb^{3+}, 0.5 % Tm^{3+} $NaYF_4$ UCNPs. **Panel D:** $\Phi_{UC}(\lambda_{em} = 470\text{-}750\ nm)$ values of the 20 % Yb^{3+}, 1.1 % Tm^{3+} and 20 % Yb^{3+}, 0.5 % Tm^{3+} $NaYF_4$ UCNPs, compared to literature values, measured as powder samples. [37, 50, 73, 75, 122-124] **Panel E:** Φ_{UC} values at the exemplarily chosen P of 40 and 370 $W \cdot cm^{-2}$ for the UC emission bands that respectively originate from the $^3H_4$, $^3F_3$, $^1G_4$ and $^1D_2$ Tm^{3+} energy levels.

A more detailed examination of the Φ_{UC} values of the respective UCL bands in panel E of Figure 36 reveals a complex, and moreover, different trend for the individual Tm^{3+} energy levels. For instance, increasing x_{Tm} at 40 $W \cdot cm^{-2}$ from 0.2 by factors of 2.5, 4.0 and 6.0 results in increased values of the $^3H_4$ UCL with factors of 4.4, 5.6 and 9.3, respectively. Further increasing x_{Tm} from 1.2 to 2.0 results in decreased UCL intensities. The optimal x_{Tm} value that yields the highest $\Phi_{UC}(\lambda_{em} = 800\ nm)$ value is therefore obviously between 0.8 and 2.0 for β-$NaYF_4$: 20 % Yb^{3+}, x_{Tm} % Tm^{3+} codoped nanocrystals with particle diameters around 30 to 40 nm. While the $^3F_3$ UCL shows the same trend as the $^3H_4$ one, the UCLs that originate from the higher Tm^{3+} energy levels reveal a different behaviour. The integrated intensities of the $^1G_4$ UCLs first in- and subsequently decrease with a factor of 4.3 for $x_{Tm} = 2.0$, while the $^1D_2$ and $^3P_6$ UCLs also first in- and henceforth decrease with factors of over 100 for $x_{Tm} = 2.0$. A very similar trend can also be observed for all x_{Tm}-dependent Φ_{UC} values at an exemplarily chosen high P of 370 $W \cdot cm^{-2}$.

Slope factors

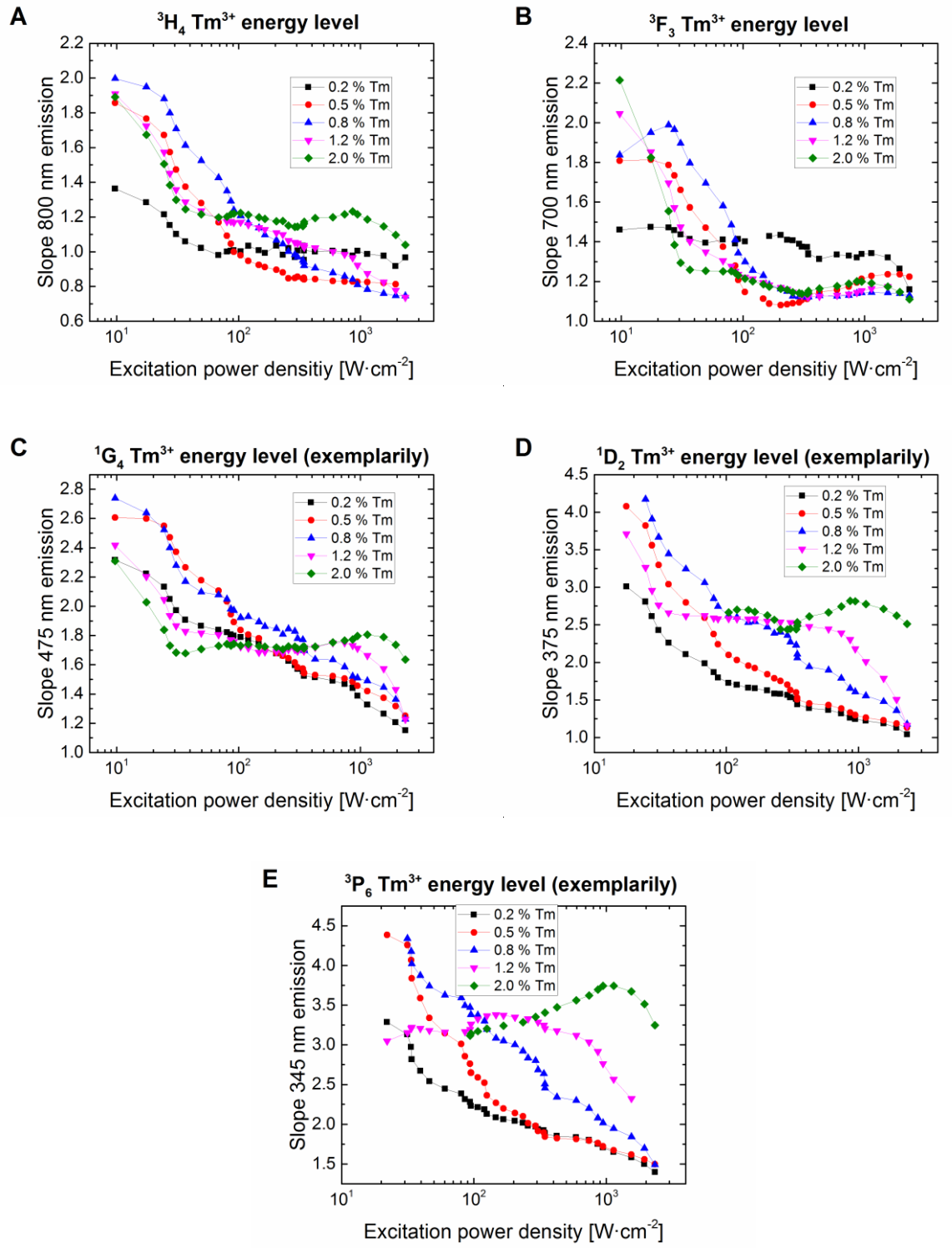

Figure 37: *P*-dependent slope factors *n(P)* of the $^3H_4$ (**panel A**), $^3F_{3,2}$ (**panel B**), $^1G_4$ (**panel C**), $^1D_2$ (**panel D**) and $^3P_6$ (**panel E**) Tm^{3+} energy levels. The plots were smoothed with a Savitzky-Golay filter.

More insights in the (de)population pathways can be gained from a closer view on the photonic order of the emission process from each Tm^{3+} energy level. These factors were subsequently calculated according to (eq.) 02. Note that $n(P, x_{Tm})$ at low P would amount to values of four, three or two, if the energy level from where the UCL in question originates, is respectively dominantly populated by four, three or two ETU steps. n amounts to lower values when CR processes become dominant in the (de)population of the energy level in question. In this study $n(x_{Tm})$ at low P varies between 2.0 and 1.4 for UCL from the $^3H_4$ and $^3F_3$, between 2.8 and 2.3 for UCL from the $^1G_4$, between 4.3 and 3.0 for UCL from the $^1D_2$ and even 4.4 and 3.0 for UCL from the $^3P_6$ Tm^{3+} energy level, respectively. Interestingly, the highest slope factors were not derived for the 17 % Yb^{3+}, 0.2 % Tm^{3+} doped UCNPs, where if any at all, the lowest influences of CR processes and therefore the highest slope factors were expected. For more details see Figure 37. At very low P, $n_{800\,nm}$ in fact shows the lowest values for the 17 % Yb^{3+}, 0.2 % Tm^{3+} doped UCNPs.

(De)population pathways

The results from especially the slope factors in the previous section underpin the complex (de)population behaviour of Yb^{3+}, Tm^{3+} codoped crystals. This consequently highlights the need to critically asses simplified rate equation models, such as one model that only assumes a biphotonic absorption process and was proposed in 2013, [73] and another model that assumes a triphotonic absorption process and was proposed in the year 2014. [72] Both models derived specific equations to test them. More complex proposed (de)population pathways on the other hand can be critically assessed by a comparison of the results from this study with trends that were reported in the literature, *e.g.*, the recent study of another research group from 2017. [70] A detailed comparison with this three models is subsequently shown in the next three subsections.

Model 1 – biphotonic absorption process. The first proposed (de)population pathways of Yb^{3+}, Tm^{3+} codoped UCPs and the resulting rate equation model that is tested, is the one from the research group of Professor Andersson-Engels from the Lund University. [73] This model assumes biphotonic absorption processes, neglects higher energy levels of the emitting ions and does not include any CR processes. It is specifically targeted to describe the UC performance of the 800 nm UCL band of Yb^{3+}, Tm^{3+} codoped UCNPs in dependence on P. The Φ_{UC} values

of the 800 nm UCL band were therefore subsequently fitted to (eq.) 05 for all five differently doped UCNP batches. The results are displayed in Figure 38. This figure shows a good agreement for the UCNPs from this study with x_{Tm} values of 0.2, 1.2 and 2.0. However, the Φ_{UC} values at 800 nm of the UCNPs from this study with x_{Tm} values of 0.5 and 0.8 predict higher values than experimentally obtained at high P, indicating that this model does not contain all main processes that are involved in the (de)population of the Yb^{3+}, Tm^{3+} codoped UCNPs.

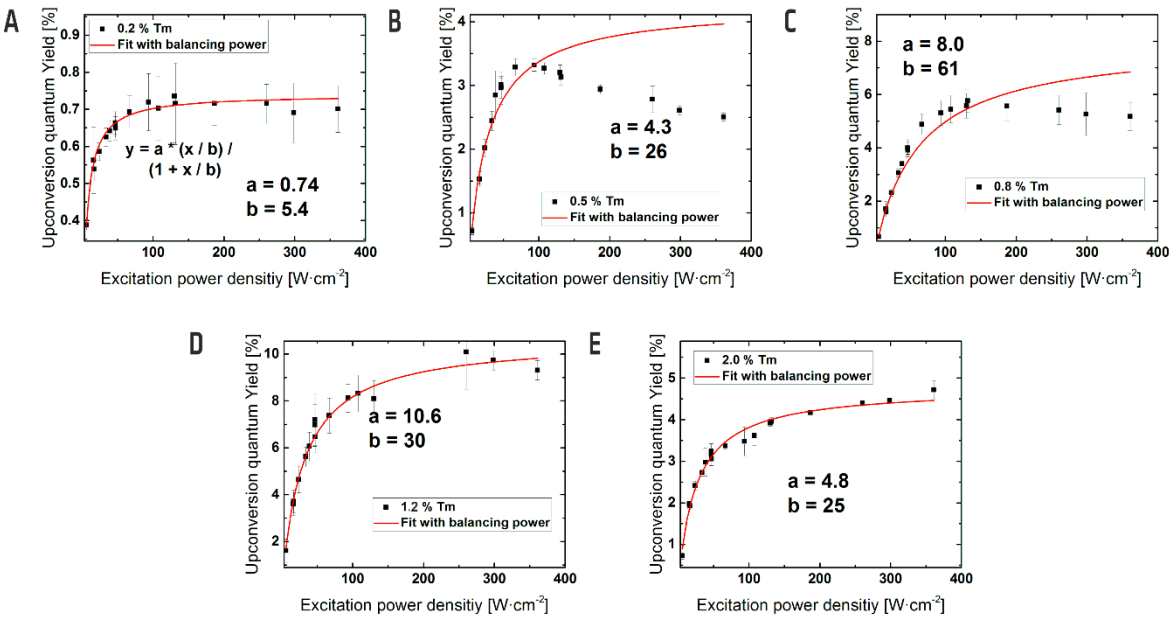

Figure 38. Φ_{UC} values of the 800 nm emission band versus excitation power density P of $NaYF_4$: 20 % Yb^{3+}, x % Tm^{3+} UCNPs with Tm^{3+} doping concentrations of x_{Tm} = 0.2 (**panel A**), 0.5 (**panel B**), 0.8 (**panel C**), 1.2 (**panel D**) and 2.0 (**panel E**). The Φ_{UC} values were fitted using (eq.) 05.

Model 2 – triphotonic absorption process. The research group of Professor Cao from the Harbin Institute of Technology proposed a rate equation model of Yb^{3+}, Tm^{3+} particles, which is only based on ETU processes, yet assumes three and not only two of them. [72] They subsequently successfully correlated the intensity ratio between the $^3H_4$ UCL band at 800 nm and the $^1G_4$ UCL band at 475 nm with τ_{mean} of the $^1G_4 \rightarrow {}^3H_6$ (475 nm) Tm^{3+} and $^2F_{5/2} \rightarrow {}^2F_{7/2}$ (980 nm) Yb^{3+} transitions for 18 nm-sized $NaYF_4$: 20 % Yb^{3+}, x_{Tm} % Tm^{3+} (x_{Tm} = 0.3, 1, 2, 3 and 4) UCNPs in cyclohexane. The correspondingly measured decay kinetics are presented in panel A of Figure 39. Panel B of Figure 39 shows the ratio of the two UCL bands versus the x_{Tm} values at an exemplarily chosen P of 40 $W \cdot cm^{-2}$, revealing increasing values from $I_{800\ nm} / I_{475\ nm}$ (x_{Tm} = 0.2) = 35 to $I_{800\ nm} / I_{475\ nm}$ (x_{Tm} = 2.0) = 1,914. However, the theoretical values of this ratio

amount to only 35 for x_{Tm} = 0.2 and to 146 for x_{Tm} = 2.0 if the respective mean decay times are inserted into (eq.) 06. Even though the relation reflects the trend of increasing $I_{800\ nm}$ / $I_{475\ nm}$ intensity ratios with increasing x_{Tm}, the results clearly differ from the predicted values and therefore do not substantiate this rate equation model, indicating that it also does not contain all main processes.

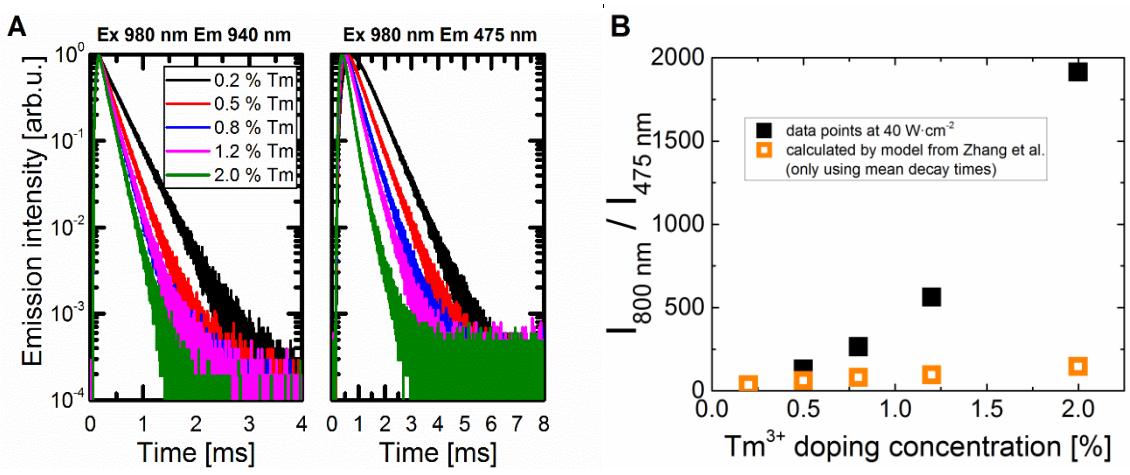

Figure 39. **Panel A:** Time-resolved spectroscopy using 980 nm excitation light of the Yb^{3+} emission at 940 nm (left) and of the Tm^{3+} emission at 475 nm (right) for all five sample batches. **Panel B:** Integrated intensity ratio between the 800 and 475 nm emission band versus Tm^{3+} doping concentrations. The black points represent the data from this work and the open orange points represent calculated values, using (eq.) 06.

Model 3 – ETU and CR processes. The fact that it was not possible to reproduce the results from this study with the equations from the two above presented models clearly shows that not only ETU, but apparently also CR processes apparently play a vital role in the (de)population of Yb^{3+}, Tm^{3+} codoped UCPs. However, it is not possible to select the dominant CR processes among the abundant amount of proposed ones, as *e.g.* depicted in Figure 7, without testing our results with extensive rate equation models, which were out of scope for this spectroscopic study. It nonetheless is possible to get a first idea which of the rate equation models should be tested first by comparing our results with trends that were reported in the literature.

The results from this study, *e.g.*, show a good agreement with the results that were presented by the research group of Professor Chen from the Dalian Maritime University. [70] They measured the intensity of the 475 and 800 nm UC emission bands of $Gd_2(WO_4)_3$: 10 % Yb^{3+}, x_{Tm} % Tm^{3+} (x_{Tm} between 0.1 and 3.0) codoped phosphors. Similar to the results in panel E of Figure 36,

they reported an increase of $I_{800\ nm}$ while increasing x_{Tm} from 0.1 to 0.5, and a decrease of $I_{800\ nm}$ for higher x_{Tm} values. They also reported a decreasing behaviour of $I_{475\ nm}$ with increasing x_{Tm}. They ascribed their behaviour to the three CR processes ($^1G_4 \rightarrow {}^3H_4$; $^3F_4 \rightarrow {}^3F_{2/3}$), ($^1G_4 \rightarrow {}^3F_{2/3}$; $^3H_5 \rightarrow {}^3F_{2/3}$) and ($^3H_4 \rightarrow {}^3F_4$; $^3H_6 \rightarrow {}^3F_4$) that accompany the typically assumed ETU processes.

4.4 Partial dissolution of UCNPs

Previous studies have raised concerns about the use of UCNPs in biological applications, as they revealed that UCNPs partially dissolve in, *e.g.*, aqueous solutions and also in the biological relevant buffer PBS. [76-79, 83] The need for an easy-accessible parameter that can be used to monitor the stability of UCNPs in biological environments therefore motivated us and the research group of Professor Lisjak from the University of Ljubljana to jointly investigate the spectroscopic properties of various batches of ligand-free UCNPs that were artificially *"aged"* under various conditions with *"unaged"* ones from the same batch. A special focus was dedicated to their decay parameters as they are known to be independent of particle concentration, yet still heavily affected by changes in the crystal field within the UCNP and their surface chemistry. Luminescence studies were beyond the scope of this study. The results are also published in Ref. [90].

4.4.1 UCNP preparation

Our cooperation partners synthesized two different batches of $NaYF_4$: 20 % Yb^{3+}, 2 % Tm^{3+} nanoparticles, using a modified version of a previously reported method that prevents a premature contact of the UCNPs with water. [106] The oleate capping of the UCNPs was subsequently removed to allow a transfer of the UCNPs in water. [125] The aging studies of these ligand-free UCNPs were then conducted either in a PBS solution with a defined pH of 7.4, or in deionized water. When dissolved in PBS, the nanoparticles were stored for two days, either at the body temperature of 37 °C, or at an elevated temperature of 50 °C. The aging studies in water consisted of an analysis of the freshly prepared- and of UCNPs that were stored for 10 days at RT in the deionized water suspension.

The variation of the dissolved fluoride ions (F^-) with respect to the nominal composition of the UCNPs (denoted as X_F) was measured by our cooperation partners and subsequently used as a measure of UCNP dissolution. [84] The subsequent measured X_F values are given in mol%, *i.e.*, that, based upon the proposed dissolution pathways and the assumption of spherical particles, a X_F value as high as, *e.g.*, 30 mol% can be interpreted as a reduced particle volume of now only $100\ \% - (30 / 4)\ \% = 92.5\ \%$. In other words, this would result in a reduced diameter of the aged UCNPs of $d_{aged} = 0.97 \cdot d_{unaged}$ for this example.

4.4.2 Structural and chemical analysis

The crystal structure of the two sample batches that were used for the spectroscopic analysis, were then analysed by our cooperation partners via their selected area electron diffraction patterns in a TEM microscope, revealing a hexagonal $NaYF_4$ crystal structure. Their morphology was determined with the same TEM microscope (size distributions obtained from ~ 150 UCNPs per sample), respectively revealing particle distributions of (36 ± 1) and (24 ± 1) nm for the two as-synthesized batches.

4.4.3 Decomposition of UCNPs in PBS and aqueous solutions

The subsequent aging conditions of the UCNPs in PBS were chosen to result in a high dynamic range of X_F values, *i.e.*, comparably higher temperatures for smaller UCNPs. [84] The results are displayed in Table 8, showing X_F values of 9.90 mol% for the 36 nm-sized UCNPs that were stored in PBS for two days at 37 °C, a slightly higher value of 11.9 mol% after an additional storage of these UCNPs in water for 10 days at RT and of only 2.0 mol% for freshly prepared UCNPs of the same batch that were stored in deionized water for 10 days at RT. The 24 nm-sized UCNPs that were stored for two days at 50 °C indeed show higher X_F values of 27.3 mol% and even slightly higher values of 29.3 mol% after an additional storage in water for 10 days at RT.

Table 8: "Released fluoride ions of the differently sized UCNPs that were aged under various conditions." Reproduced with permission. [90]

particle size [nm]	X_F [mol%]	aging conditions
36 ±1	9.90 ± 0.02	PBS, 2 days, 37 °C
	11.9 ± 0.1	PBS, 2 days, 37 °C + water, 10 days, RT
	2.0 ± 0.2	water, 10 days, RT
24 ± 1	27.3 ± 0.1	PBS, 2 days, 50 °C
	29.3 ± 0.2	PBS, 2 days, 50 °C + water, 10 days, RT

4.4.4 Spectroscopic analysis

The influence of the artificial aging process on the steady state and time resolved luminescence spectra was subsequently recorded in Berlin by Doctor Olivija Plohl and me with the spectrofluorometers that were mentioned in *section 3.2.2*. The dried unaged and aged UCNP powder samples were therefore weighted and dispersed in deionized water, always using the same concentration. Early results from this study, *i.e.* the UCL spectra and normalized decay kinetics of

the 980 nm DC emission band, are also published in the Doctoral Dissertation of Olivija from September 2016. It is titled "*Dissolution of fluoride upconverting nanoparticles in aqueous suspensions and their protection with amphiphilic coatings*". These results, however, were only briefly touched in the Doctoral Dissertation of Olivija Plohl and not properly addressed. This will be done in the following.

Upconversion luminescence

The resulting UCL spectra are displayed in panel A of Figure 40. They reveal considerable differences with respective integrated emission intensities between 450 and 850 nm of 100, 22.6, 8.4 and 1.6 % for the 36 nm-sized unaged, the 36 nm-sized aged, the 24 nm-sized unaged and the 24 nm-sized aged UCNPs. The comparison of the UCL spectra of the unaged and aged UCNPs, however, has to be regarded with caution as the dried aged UCNP samples can possibly also contain side products from the dissolution process. That said, a comparison between the integrated UCL from the freshly prepared unaged UCNPs is still valid and substantiates the considerable influence of surface effects on the UCL, reported for Yb^{3+}, Er^{3+} based UCNPs in *section 4.1*.

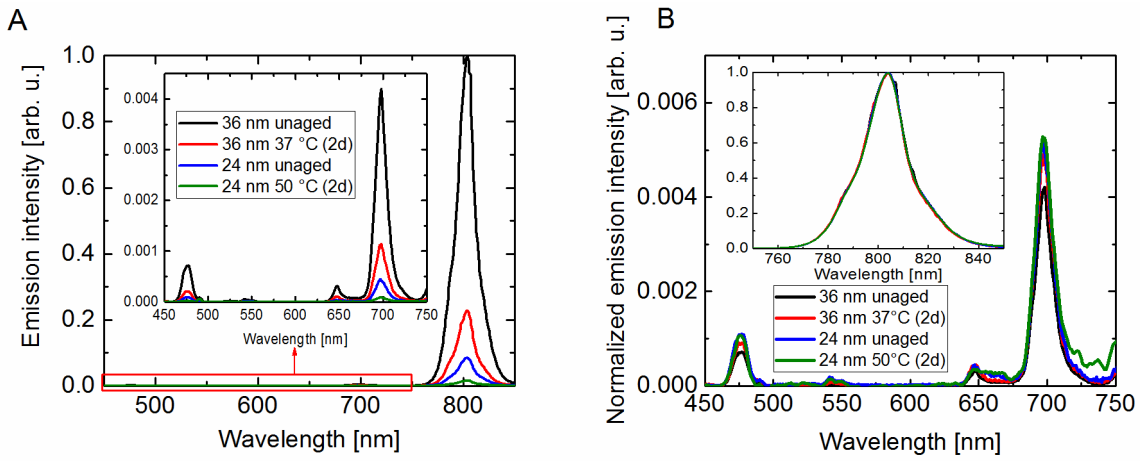

Figure 40: "**Panel A:** Respective UCL spectra from the freshly prepared unaged 36 and 24 nm-sized UCNPs and from the 36 and 24 nm-sized UCNPs that were respectively stored in PBS for two days at 37 or 50 °C. The insets shows a magnification of the emission between 450 and 750 nm. All samples were dispersed with the same concentration of the solid phase in deionized water and were measured using the same conditions. **Panel B**: Normalized UCL spectra (to emission intensity at 800 nm) from panel A. The inset shows the strong 800 nm emission." Reproduced with permission. [90]

The UCL spectra were therefore also normalized to the respective emission intensity at 800 nm, as displayed in panel B of Figure 40. It is noteworthy and surprising that they do not show any clear trend, contrary to our expectations. For example, a smaller ratio of the integrated emission intensities at 475 and 800 nm could have been expected, both for a comparison of the 24 and 36 nm-sized and for a respective comparison of the aged and unaged UCNPs. This assumption is based on previous findings, *e.g.* in *section 4.1*, that suggested a higher order influence of surface quenching effects on three-photonic (here the $^1G_4 \rightarrow {}^3H_6$ transition at 475 nm), compared to two-photonic transition processes (here $^3H_4 \rightarrow {}^3H_6$ at 800 nm). The next step was therefore to look at the luminescence decay curves, as they are not influenced by possible side products from the dissolution process and hence, allow for a direct comparison of the samples.

Luminescence decay behaviour

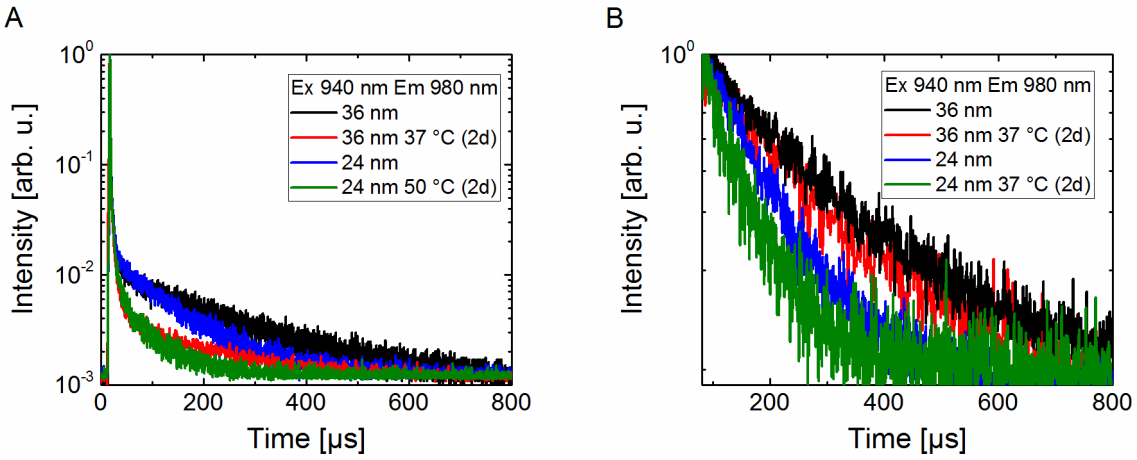

Figure 41: Panel A: Respective normalized luminescence decay curves of the directly excited Yb^{3+} emission of the freshly prepared unaged 36 and 24 nm-sized UCNPs and from the 36 and 24 nm-sized UCNPs that were respectively stored in PBS for two days at 37 or 50 °C. **Panel B:** "Stretched and differently normalized (to emission intensity at $t_1 = 85\ \mu s$) decay kinetics from panel A." Reproduced with permission. [90]

The normalized luminescence decay curves of the directly excited 980 nm emission are displayed in panel A of Figure 41 as one example, revealing significant differences for the respective unaged and aged UCNP samples. For instance, the decay curves show a higher amplitude of a very fast decay component for both aged samples. A comparison of the decay kinetics of this emission band for freshly prepared unaged UCNPs and the same UCNPs, stored for 10 days in water at RT, also revealed a higher amplitude of this short component (data not shown). As stated in the literature, this could be attributed to an additional very fast decay component

from a completely quenched, dark surface layer, created or extended by the surface hydrolysis / dissolution process. [54] To allow for an easy comparison of the decay curves, only the long decay component that becomes dominant after $t_1 = 85\ \mu s$ was chosen for the subsequent evaluation. A tail fit of this decay component, however, was not feasible in this first preliminary proof-of-concept study due to the low signal-to-noise ratio. Furthermore, the higher amplitude of the very short component complicates an easy comparison of spectra that were measured under the same conditions. These spectra were therefore normalized at t_1, as displayed in panel B of Figure 41, now allowing for a comparison of their integrated decay curves, and hence the calculation of the quenching efficiency from the aging process according to (eq.) 10. In this case, I_q refers to the integrated decay curve from the aged and I_0 to the integrated decay curve from the associated unaged UCNP sample.

The normalized decay curves of the Tm^{3+} UCLs at 800, 700 and 475 nm are respectively displayed in panels A-C of Figure 42, again revealing considerable differences for the unaged and aged UCNPs. Furthermore, the decay kinetics of the 800 nm UCL in panel A of Figure 42, *e.g.*, still show a considerable rising component at $t_2 = 0.76\ ms$ for the 24 nm-sized unaged and aged and at $t_3 = 0.96\ ms$ for the 36 nm-sized unaged and aged UCNPs, despite the fact that the intensity of the excitation pulse was already negligible at $t = 0.66\ ms$ (start of the excitation pulse at $t_0 = 0.26\ ms$; pulse width of 0.4 ms). The respective integrated intensities from this UCL were therefore respectively calculated starting from t_2 for the 24 nm-sized unaged and aged and starting from t_3 for the 36 nm-sized unaged and aged UCNP samples (see also green and red areas under the respective curve in panel A of Figure 42).

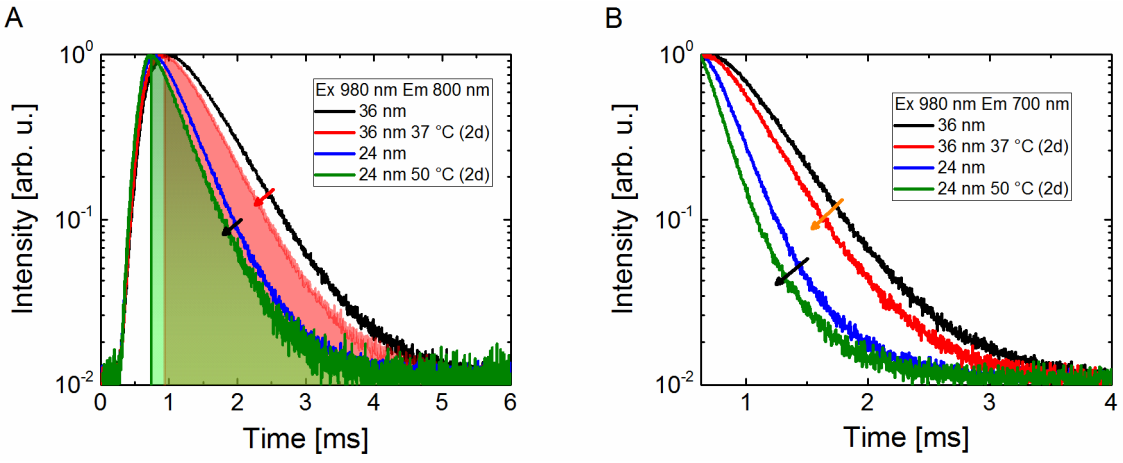

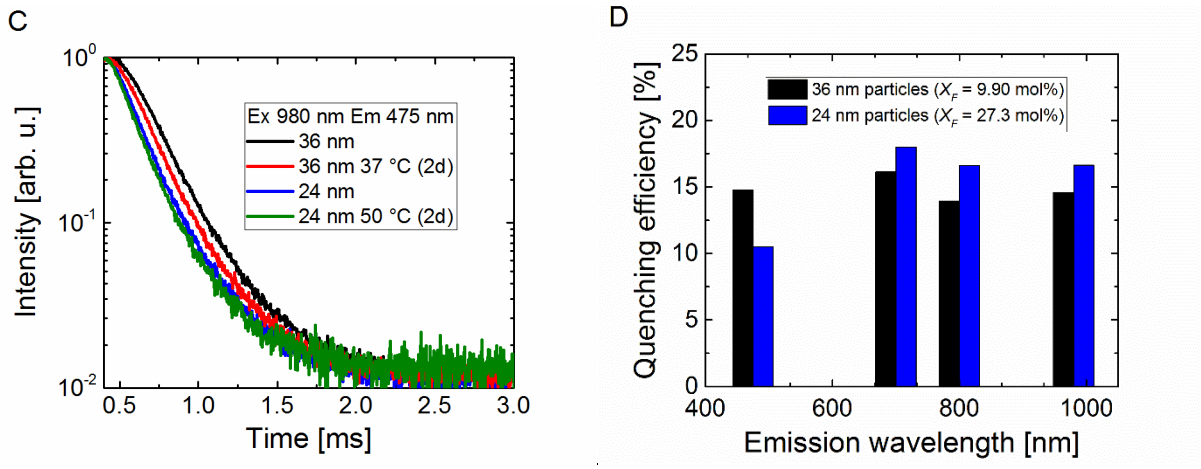

Figure 42: "Normalized luminescence decay curves of the 800 (**panel A**), 700 (**panel B**) and 475 nm (**panel C**) UCL upon 980 nm excitation of the freshly prepared unaged 36 and 24 nm-sized UCNPs and from the 36 and 24 nm-sized UCNPs that were respectively stored in PBS for two days at 37 or 50 °C. The areas under the curve that were used for the data evaluation were respectively highlighted in **panel A** for the decay curves of the aged UCNPs. **Panel D:** Luminescence quenching efficiency (see (eq.) 10) that were derived from the integrated decay curves of the 800, 700 and 475 nm Tm^{3+} UC and directly excited 980 nm Yb^{3+} DC emission." Reproduced with permission. [90]

The decay curves of the UCLs at 700 and 475 nm do not show such a rising component after the excitation pulse, and hence, their integrated intensities were respectively calculated starting from $t_4 = 0.66\ ms$. The resulting quenching efficiencies are displayed in panel D of Figure 42. The values of the quenching efficiency amount to ~ 15 % for all investigated UCL bands of the 36 nm-sized and to ~ 16 % for the 700 and 800 nm Tm^{3+} and 980 nm Yb^{3+} emission band of the 24 nm-sized UCNPs. The quenching efficiency of the 475 nm UCL band of the 24 nm-sized UCNPs, however, only amounts to ~ 11 %, although again a stronger quenching of this three-photonic UCL, compared to the two-photonic UCL at 800 nm, could have been expected based on the previous studies from this thesis.

5 Summary and conclusion

UCNPs have emerged as a novel class of non-linear luminescent with a great potential for many possible applications, as briefly broached in the introduction part. However, some open questions still need to be addressed before UCNPs can experience a true breakthrough. Some of them were addressed and thoroughly investigated in this PhD thesis. This includes on the one side the question how to construct bright and small UCNPs, which was addressed in the first three studies, and on the other side if there is an easy accessible spectroscopic parameter that can be utilized for a long-term stability control of UCNPs in biologically relevant media, which was addressed in the fourth and last study from this work.

5.1 Summary and conclusion of size-dependent study

The first study of this thesis presented a quantitative analysis of the influence of the particle size on the UCL colour, the excited state (de)population pathways of the up- and downconversion luminescence and the respective efficiency values. The resulting size-dependent solvent-induced surface quenching was quantified for $NaYF_4$: 20 % Yb^{3+}, 2 % Er^{3+} UCNPs with diameters ranging from 12 to 43 nm for the most common quenchers, *i.e.* high energy vibrational modes of O-H and C-H bonds as present in many molecules. Most importantly, this study underlined the potential of the parameters *P* and particle size to tune the emission colour as demonstrated by the dominant NIR emission of 12 nm-sized UCNPs under "strongly quenched" conditions in water at low *P*. As current rate equation models do not include this emission, the suitability of these models to accurately simulate all UC (de)population pathways of very small UCNPs needs to be critically assessed. [54, 57, 58, 75] Furthermore, examination of the red emissive $^4F_{9/2}$ energy level of Er^{3+} revealed different feeding pathways under "strongly quenched", *i.e.*, low *P*, small size, O-H vibrations, and "quenched" or "non-quenched" conditions, *i.e.* higher *P*, sizes > 20 nm, C-H containing- / no solvent molecules in the neighbourhood of the Ln^{3+} emitters.

Moreover, it was possible to assess an approach to estimate particle sizes where surface quenching could be neglected, utilizing the experimentally determined decay kinetics of the directly excited 980 nm emission of Yb^{3+} of our UCNP size series in cyclohexane and water and the linear extrapolation of the quotient of these lifetimes, suggesting an upper size limit of about 115 nm. Another result from this study is that the Φ_{UC} values vary by a factor of about 260 for

the 43 and 12 nm-sized UCNPs in cyclohexane at $P < 100$ W·cm^{-2} and even about 560 for those UCNPs in water. This was associated with two factors, namely a reduced effective P of smaller UCNPs and by smaller Φ_{UC} values at high P. Lastly, a volumetric-scaling method was applied to fit the particle size dependent $\Phi_{UC\text{-}sat,green}$ values. The results still indicate considerable differences of the Φ_{UC} values of UCNPs with sizes above 115 nm, respectively dispersed in water and cyclohexane. This could be associated with the fact that the Φ_{UC} values are affected by both the absorption and emission behaviour of the Ln^{3+} ions, whilst the decay kinetics are only affect by their emission behaviour.

It can therefore be concluded that it is crucial to protect especially the Yb^{3+} sensitizer ions from energy transfer processes to surrounding ligands, solvent molecules and surface defects in order to construct highly efficient UCNPs. This could be achieved by the use of different and more complex nanostructures, or by the use of a thin protective shell.

5.2 Summary and conclusion of 2Er@z_{Yb}Yb core-shell nanostructure

The second study explored the spectroscopic properties of a $NaYF_4$@$NaYF_4$ core-shell nanostructure that respectively confines the Er^{3+} activator ions with a defined doping concentration of 2 % in the core and the Yb^{3+} sensitizer ions with defined doping concentrations between 2 and 100 % in the shell. The respective UCNPs were denoted as 2Er@z_{Yb}Yb. The results show considerable differences in UCL colour, revealing different population densities of the respective emissive Er^{3+} energy levels for different Yb^{3+} doping concentrations in the shell. The $^4F_{9/2}$ Er^{3+} energy level, from where the red 655 nm UCL occurs, was even shown to be mainly populated by different processes, namely a mixture of bi- and triphotonic processes for $z_{Yb} > 10$ and solely by biphotonic process otherwise. Consequently, the most UC photons are emitted from the $^2H_{11/2}$/$^4S_{3/2}$ energy levels at high and low P for $z_{Yb} < 40$, from the lower $^4F_{9/2}$ energy level at high P for $z_{Yb} > 40$ and from the even lower $^4I_{9/2}$ energy level at low P for $z_{Yb} > 40$.

Efficiency studies furthermore showed the highest values for the 2Er@10Yb UCNPs at all experimental applied P from this study (3-370 W·cm^{-2}). This trend, however, is different at very high P. For example, an exemplarily fitting of Φ_{UC} versus P of the biphotonic UCL band at 540 nm with the balancing power formula revealed that the $\Phi_{UC\text{-}sat,green}$ values subsequently decrease with increasing z_{Yb}, indicating that at a very high P, the 2Er@2Yb UCNPs should be the most efficient ones. The fitting with this formula furthermore revealed an alternating behaviour of

the $P_{balance}$ value. However, a subsequent comparison of the particle brightness's furthermore revealed the highest values for the 2Er@10Yb and not the 2Er@2Yb UCNPs, not only at the applied *P* from this study, but also even for very high *P*. Nevertheless, the brightness values from these UCNPs were still around six to 11-times lower than the ones from core-only UCNPs with traditional doping concentrations of 20 % Yb^{3+} and 2 % Er^{3+}. It can therefore be concluded that this Er@Yb nanostructure is less suitable for the many different applications of UCNPs, compared to the typical Yb,Er codoped nanostructure.

5.3 Summary and conclusion of Tm^{3+} concentration-dependent study

The third study presented a comprehensive analysis of the influence of Tm^{3+} doping concentrations (x_{Tm}) on the spectroscopic properties of commonly used $NaYF_4$: 16-18 % Yb^{3+}, x_{Tm} % Tm^{3+} codoped UCNPs in a typical apolar solvent. Using absolute fluorometry, it was possible to identify different optimal x_{Tm} values that yield the highest UCL efficiencies for the respective different Tm^{3+} emission bands. For instance, the optimal x_{Tm} value yielding the highest population densities of the $^3H_4$ and $^3F_{3/2}$ Tm^{3+} energy levels, and therefore the highest efficiencies for emission wavelengths above 700 nm, was reported to between 0.8 and 2.0, while the optimal x_{Tm} value yielding the highest population densities of the $^1G_4$, $^1D_2$ and $^3P_6$ Tm^{3+} energy levels, and therefore the highest efficiencies for emission wavelengths below 700 nm, is between 0.2 and 0.8. This different behaviour could be traced back to a (de)population of the respective Tm^{3+} energy levels via an apparent mixture of energy transfer upconversion- and cross-relaxation processes. However, it was not possible to select the dominant cross-relaxation processes without the validation by a comparison with rate equation models, which was beyond the scope of this study.

5.4 Summary and conclusion of dissolution study

The last study of this thesis investigated the spectroscopic properties of exemplarily chosen various batches of ligand-free Yb^{3+}, Tm^{3+} codoped hexagonal $NaYF_4$ UCNPs and compared UCNPs that were artificially *"aged"* under various conditions with *"unaged"* ones from the same batch. The artificial aging process was comprised by a storage of the ligand-free UCNPs at elevated temperatures in either a PBS solution, or in deionized water.

The aim was to subsequently identify an easily and quickly accessible parameter as a prerequisite for the straightforward monitoring and long-term control of UCNPs in biologically relevant

media. An overall comparison of the respective unaged and aged UCNPs indeed revealed a correlation of the partial particle dissolution with the luminescence quenching, however, the size of the luminescence quenching showed no significant quantitative correlation with the degree of UCNP dissolution. The comparison also revealed that the decay kinetics of both the Tm^{3+} UCL bands at 700 and 800 nm, and the directly excited Yb^{3+} emission at 980 nm apparently are suitable screening parameters for a monitoring of the stability of UCNPs. However, the directly excited Yb^{3+} emission at 980 nm requires an elaborate data evaluation and as the 700 nm UCL is more than two orders of magnitude smaller than the UCL at 800 nm. It would therefore be preferable to use the luminescence lifetime of the 800 nm emission as the parameter for stability screening of Yb^{3+}, Tm^{3+} based UCNPs and changes in their particle surface chemistry.

6 Perspectives

A fundamental and very important result of this thesis is that the current rate equation models of Yb^{3+}, Er^{3+} codoped systems need to be critically assessed for very small particles with sizes of 10 nm or less in water, as they do not contain the strongest UCL band of these very small particles in this solvent, the UCL band at 810 nm. This is especially important as a complete understanding of the (de)population dynamics of such nanoparticles can enable the rational design of upconversion nanocrystals with improved luminescence efficiencies and a future computational screening to easily identify the optimal parameters of application-specific tailored, yet very bright particles. This could also help to identify optimal parameters for other nanostructures that potentially could have a higher brightness. One promising example is the same nanostructure as in the third study of this PhD thesis, although now confining the Yb^{3+} sensitizer ions in the core and the Er^{3+} activator ions in the particle shell. The recent joint study with the research group of Professor Zhang from the National University of Singapore briefly explored this architecture and even proposed to use additional bridging Yb^{3+} in the particle shell to achieve an ever brighter UCL. The highest UCL was reported for an Yb^{3+} concentration of 70 % in the particle core and a codoping of 6 % Er^{3+} and 4 % Yb^{3+} in the particle shell. [67] Another approach that is currently discussed in the literature is to increase the brightness of small UCNPs by either coating them with a layer of gold and consequently exploiting plasmonic surface effects to enhance both the absorption and emission properties of the UCNP, or to bind organic antenna dyes to the UCNP surface that possess a much greater absorption coefficient than the typically used Yb^{3+} ions.

Furthermore, as the last study from this thesis presented a proof-of-concept study only, the next step in the derivation of a clear correlation between spectroscopic properties, fluoride release and particle dissolution is a systematic study of differently sized UCNPs that were respectively aged under the same conditions, also including UCL efficiency measurements that could not be performed in the fourth and last study. This new study should moreover also include UCNPs that are codoped with Er^{3+} and other Ln^{3+} ions.

7 Appendix

List of Abbreviations

Symbol	*Description*
UC	upconversion
TTA	triplet-triplet-annihilation
SHG	second-harmonic generation
GSA	ground state absorption
ESA	excited state absorption
APTE	addition de photon par transferts d'energie
ETU	energy transfer upconversion
ET	energy transfer
CR	cross-relaxation
MPR	multiphonon-relaxation
BET	back-energy transfer
a-$NaYF_4$	sodium yttrium tetrafluoride with cubic crystal structure
β-$NaYF_4$	sodium yttrium tetrafluoride with hexagonal crystal structure
Ln^{3+}	trivalent lanthanide ion
Y^{3+}	trivalent yttrium ion
Yb^{3+}	trivalent ytterbium ion
Er^{3+}	trivalent erbium ion
Tm^{3+}	trivalent thulium ion
Ho^{3+}	trivalent holmium ion
Pr^{3+}	trivalent praseodymium ion
Gd^{3+}	trivalent gadolinium ion
$^{2S+1}L_J$	Russel-Saunders-notation
S	total spin
L	total orbital momentum
J	total angular momentum
UCL	upconversion luminescence
UCP	upconversion particle

UCNP	upconversion nanoparticle
UV	ultraviolet
vis	visible
NIR	near-infrared
P	excitation power density
Φ	quantum yield
Φ_{UC}	upconversion quantum yield
N_{abs}	number of absorbed photons
N_{em}	number of emitted photons
I_{em}	integrated emission intensity
$\lambda_{IR\text{-}em}$	integration range for evaluation of emission intensity
n	number of photons that are required to populate the corresponding emissive energy state (also called “slope factor”)
DC	down-converted
λ_{ex}	excitation wavelength
λ_{em}	emission wavelength
I(t)	luminescence decay kinetic
τ_{mean}	amplitude weighted lifetime
a_i	amplitude component
τ_i	lifetime component
W	luminescence decay rate
r_0	radius of the dark surface layer
Φ_0	efficiency value of the luminescent core
d	radius of the spherical upconversion nanoparticle
V_2	volume of the luminescent core
V_1	volume of the whole particle
G/R	integrated emission intensity ratio of the green and red Er^{3+} upconversion luminescence bands
FRET	Förster resonance energy transfer
Er@Yb	core-shell nanostructure with confined Er^{3+} doping in the particle core and Yb^{3+} doping in the particle shell
Yb@Er	core-shell nanostructure with confined Yb^{3+} doping in the

	particle core and Er^{3+} doping in the particle shell
Yb@Er,Yb	core-shell nanostructure with confined Yb^{3+} doping in the particle core and an Yb^{3+} and Er^{3+} codoping in the particle shell
B	brightness
N_{Yb}	number of Yb^{3+} sensitizer ions
$P_{balance}$	balancing power density
$\Phi_{UC\text{-}sat}$	saturation upconversion quantum yield
$\Phi_{UC\text{-}sat,green}$	saturation upconversion quantum yield of the integrated Er^{3+} UCL between 510-570 nm
$\tau_{980\ nm}$	mean lifetime of the $^2F_{5/2}$ Yb^{3+} energy state
$\tau_{475\ nm}$	mean lifetime of the $^1G_4$ Tm^{3+} energy state
x_{Yb}	Yb^{3+} doping concentration
x_{Tm}	Tm^{3+} doping concentration
z_{Yb}	Yb^{3+} doping concentration in the particle shell
SA/Vol	surface-area-to-volume ratio
RT	room temperature
PBS	phosphate buffered saline
XRD	X-ray pattern diffraction analysis
DLS	diffraction light scattering
TEM	transmission electron microscopy
ICP-OES	inductively coupled plasma optical emission spectroscopy
InGaAs	indium-gallium-arsenide
CCD	charge-coupled device
ND	neutral density
Si	silicon
NIST	National Institute of Standards and Technology
F002-F005	calibrated spectral emission standards from the Bundesanstalt fuer Materialforschung und -pruefung
$s_{\lambda em}$	spectral responsivity
h	planck constant
c_0	speed of light in vacuum
MCS	multi-channel counting

PMT	photomultiplier tube
I_q	intensity in the presence of a luminescence quencher / quenching process
I_0	initially measured intensity in the absence of a quencher / quenching process
η(quenching)	quenching efficiency
OA	oleic acid
PAA	polyacrylic acid
F^-	fluoride ion
X_F	variation of the dissolved fluoride ions with respect to the nominal composition of the UCNPs

8 Bibliography

[1] Parker, C. A.; Hatchard, C. G. Sensitised anti-stokes delayed fluorescence. *P Chem Soc London* **1962**, 386-&.

[2] Bloembergen, N. Solid state infrared quantum counters. *Phys Rev Lett* **1959,** *2*, 84-85.

[3] Auzel, F. Upconversion and anti-stokes processes with f and d ions in solids. *Chemical Reviews* **2004,** *104*, 139-173.

[4] Fischer, S.; Steinkemper, H.; Loper, P.; Hermle, M.; Goldschmidt, J. C. Modeling upconversion of erbium doped microcrystals based on experimentally determined einstein coefficients (vol 111, 013109, 2012). *J Appl Phys* **2012,** *111*.

[5] Hyppanen, I.; Lahtinen, S.; Aaritalo, T.; Makela, J.; Kankare, J.; Soukka, T. Photon upconversion in a molecular lanthanide complex in anhydrous solution at room temperature. *Acs Photonics* **2014,** *1*, 394-397.

[6] Nonat, A.; Chan, C. F.; Liu, T.; Platas-Iglesias, C.; Liu, Z. Y.; Wong, W. T.; Wong, W. K.; Wong, K. L.; Charbonniere, L. J. Room temperature molecular up conversion in solution. *Nat Commun* **2016,** *7*.

[7] Souri, N.; Tian, P. P.; Platas-Iglesias, C.; Wong, K. L.; Nonat, A.; Charbonniere, L. J. Upconverted photosensitization of tb visible emission by nir yb excitation in discrete supramolecular heteropolynuclear complexes. *J Am Chem Soc* **2017,** *139*, 1456-1459.

[8] Aboshyan-Sorgho, L.; Cantuel, M.; Petoud, S.; Hauser, A.; Piguet, C. Optical sensitization and upconversion in discrete polynuclear chromium-lanthanide complexes. *Coordin Chem Rev* **2012,** *256*, 1644-1663.

[9] Singh-Rachford, T. N.; Castellano, F. N. Low power visible-to-uv upconversion. *J Phys Chem A* **2009,** *113*, 5912-5917.

[10] Islangulov, R. R.; Lott, J.; Weder, C.; Castellano, F. N. Noncoherent low-power upconversion in solid polymer films. *J Am Chem Soc* **2007,** *129*, 12652-+.

[11] Wu, M. F.; Congreve, D. N.; Wilson, M. W. B.; Jean, J.; Geva, N.; Welborn, M.; Van Voorhis, T.; Bulovic, V.; Bawendi, M. G.; Baldo, M. A. Solid-state infrared-to-visible upconversion sensitized by colloidal nanocrystals. *Nat Photonics* **2016,** *10*, 31-34.

[12] Aulin, Y. V.; van Sebille, M.; Moes, M.; Grozema, F. C. Photochemical upconversion in metal-based octaethyl porphyrin-diphenylanthracene systems. *Rsc Adv* **2015,** *5*, 107896-107903.

[13] Bril, A.; Sommerdijk, J. L.; Jager, A. W. D. Efficiency of yb3+-er3+ activated up-conversion phosphors. *Journal of the Electrochemical Society* **1974,** *121*, C95-C95.

[14] Heer, S.; Kompe, K.; Gudel, H. U.; Haase, M. Highly efficient multicolour upconversion emission in transparent colloids of lanthanide-doped nayf4 nanocrystals. *Advanced Materials* **2004,** *16*, 2102-+.

[15] Yi, G. S.; Lu, H. C.; Zhao, S. Y.; Yue, G.; Yang, W. J.; Chen, D. P.; Guo, L. H. Synthesis, characterization, and biological application of size-controlled nanocrystalline nayf4 : Yb,er infrared-to-visible up-conversion phosphors. *Nano Letters* **2004,** *4*, 2191-2196.

[16] Resch-Genger, U.; Gorris, H. H. Perspectives and challenges of photon-upconversion nanoparticles - part i: Routes to brighter particles and quantitative spectroscopic studies. *Anal Bioanal Chem* **2017,** *409*, 5855-5874.

[17] Wilhelm, S. Perspectives for upconverting nanoparticles. *ACS Nano* **2017**.

[18] Pichaandi, J.; Boyer, J. C.; Delaney, K. R.; van Veggel, F. C. J. M. Two-photon upconversion laser (scanning and wide-field) microscopy using ln(3+)-doped nayf4 upconverting nanocrystals: A critical evaluation of their performance and potential in bioimaging. *J Phys Chem C* **2011,** *115*, 19054-19064.

[19] Yang, Y. M.; Shao, Q.; Deng, R. R.; Wang, C.; Teng, X.; Cheng, K.; Cheng, Z.; Huang, L.; Liu, Z.; Liu, X. G. et al. In vitro and in vivo uncaging and bioluminescence imaging by using photocaged upconversion nanoparticles. *Angew Chem Int Edit* **2012,** *51*, 3125-3129.

[20] Zhan, Q. Q.; Qian, J.; Liang, H. J.; Somesfalean, G.; Wang, D.; He, S. L.; Zhang, Z. G.; Andersson-Engels, S. Using 915 nm laser excited tm3+/er3+/ho3+-doped naybf4 upconversion nanoparticles for in vitro and deeper in vivo bioimaging without overheating irradiation. *Acs Nano* **2011,** *5*, 3744-3757.

[21] Resch-Genger, U.; Grabolle, M.; Cavaliere-Jaricot, S.; Nitschke, R.; Nann, T. Quantum dots versus organic dyes as fluorescent labels. *Nature Methods* **2008,** *5*, 763-775.

[22] Haase, M.; Schafer, H. Upconverting nanoparticles. *Angewandte Chemie-International Edition* **2011,** *50*, 5808-5829.

[23] Xu, C. T.; Zhan, Q. Q.; Liu, H. C.; Somesfalean, G.; Qian, J.; He, S. L.; Andersson-Engels, S. Upconverting nanoparticles for pre-clinical diffuse optical imaging, microscopy and sensing: Current trends and future challenges. *Laser & Photonics Reviews* **2013,** *7*, 663-697.

[24] Resch-Genger, U.; Gorris, H. H. Perspectives and challenges of photon-upconversion nanoparticles - part i: Routes to brighter particles and quantitative spectroscopic studies. *Analytical and Bioanalytical Chemistry* **2017**.

[25] Gorris, H. H.; Resch-Genger, U. Perspectives and challenges of photon-upconversion nanoparticles - part ii: Bioanalytical applications. *Analytical and Bioanalytical Chemistry* **2017**.

[26] Bunzli, J. C. G.; Piguet, C. Taking advantage of luminescent lanthanide ions. *Chem Soc Rev* **2005,** *34*, 1048-1077.

[27] Russell, H. N.; Saunders, F. A. New regularities in the spectra of the alkaline earths. *Astrophysical Journal* **1925,** *61*, 38-69.

[28] Wang, F.; Han, Y.; Lim, C. S.; Lu, Y. H.; Wang, J.; Xu, J.; Chen, H. Y.; Zhang, C.; Hong, M. H.; Liu, X. G. Simultaneous phase and size control of upconversion nanocrystals through lanthanide doping. *Nature* **2010,** *463*, 1061-1065.

[29] Suyver, J. F.; Grimm, J.; Kramer, K. W.; Gudel, H. U. Highly efficient near-infrared to visible up-conversion process in nayf4 : Er,3+yb3+. *Journal of Luminescence* **2005,** *114*, 53-59.

[30] Liu, G. K. Advances in the theoretical understanding of photon upconversion in rare-earth activated nanophosphors. *Chemical Society Reviews* **2015,** *44*, 1635-1652.

[31] Gamelin, D. R.; Gudel, H. U. Excited-state dynamics and sequential two-photon upconversion excitation of mo3+-doped chloro- and bromo-elpasolites. *Journal of Physical Chemistry B* **2000,** *104*, 10222-10234.

[32] Luthi, S. R.; Hehlen, M. P.; Riedener, T.; Gudel, H. U. Excited-state dynamics and optical bistability in the dimer system cs3lu2br9 : Yb3+. *Journal of Luminescence* **1998,** *76-7*, 447-450.

[33] Pilch, A.; Wurth, C.; Kaiser, M.; Wawrzynczyk, D.; Kurnatowska, M.; Arabasz, S.; Prorok, K.; Samoc, M.; Strek, W.; Resch-Genger, U. et al. Shaping luminescent properties of yb3+ and ho3+ co-doped upconverting core-shell beta-nayf4 nanoparticles by dopant distribution and spacing. *Small* **2017,** *13*.

[34] Cao, B. S.; He, Y. Y.; Zhang, L.; Dong, B. Upconversion properties of er3+-yb3+:Nayf4 phosphors with a wide range of yb3+ concentration. *Journal of Luminescence* **2013,** *135*, 128-132.

[35] Kramer, K. W.; Biner, D.; Frei, G.; Gudel, H. U.; Hehlen, M. P.; Luthi, S. R. Hexagonal sodium yttrium fluoride based green and blue emitting upconversion phosphors. *Chemistry of Materials* **2004,** *16*, 1244-1251.

[36] Suyver, J. F.; Grimm, J.; van Veen, M. K.; Biner, D.; Kramer, K. W.; Gudel, H. U. Upconversion spectroscopy and properties of nayf4 doped with er (3+), tm3+ and/or yb3+. *Journal of Luminescence* **2006,** *117*, 1-12.

[37] Page, R. H.; Schaffers, K. I.; Waide, P. A.; Tassano, J. B.; Payne, S. A.; Krupke, W. F.; Bischel, W. K. Upconversion-pumped luminescence efficiency of rare-earth-doped hosts sensitized with trivalent ytterbium. *J Opt Soc Am B* **1998,** *15*, 996-1008.

[38] Kaiser, M.; Wurth, C.; Kraft, M.; Hyppanen, I.; Soukka, T.; Resch-Genger, U. Power-dependent upconversion quantum yield of nayf4:Yb3+,er3+ nano- and micrometer-sized particles - measurements and simulations. *Nanoscale* **2017**.

[39] Anderson, R. B.; Smith, S. J.; May, P. S.; Berry, M. T. Revisiting the nir-to-visible upconversion mechanism in beta-nayf4:Yb3+,er3+. *J Phys Chem Lett* **2014,** *5*, 36-42.

[40] Martin-Rodriguez, R.; Rabouw, F. T.; Trevisani, M.; Bettinelli, M.; Meijerink, A. Upconversion dynamics in er3+-doped gd2o2s: Influence of excitation power, er3+ concentration, and defects. *Advanced Optical Materials* **2015,** *3*, 558-567.

[41] Boyer, J. C.; van Veggel, F. C. J. M. Absolute quantum yield measurements of colloidal nayf4: Er3+, yb3+ upconverting nanoparticles. *Nanoscale* **2010,** *2*, 1417-1419.

[42] Chen, F.; Bu, W. B.; Zhang, S. J.; Liu, X. H.; Liu, J. N.; Xing, H. Y.; Xiao, Q. F.; Zhou, L. P.; Peng, W. J.; Wang, L. Z. et al. Positive and negative lattice shielding effects co-existing in gd (iii) ion doped bifunctional upconversion nanoprobes. *Advanced Functional Materials* **2011,** *21*, 4285-4294.

[43] Lim, S. F.; Ryu, W. S.; Austin, R. H. Particle size dependence of the dynamic photophysical properties of nayf4:Yb, er nanocrystals. *Optics Express* **2010,** *18*, 2309-2316.

[44] Schietinger, S.; Menezes, L. D.; Lauritzen, B.; Benson, O. Observation of size dependence in multicolor upconversion in single yb3+, er3+ codoped nayf4 nanocrystals. *Nano Letters* **2009,** *9*, 2477-2481.

[45] Vetrone, F.; Boyer, J. C.; Capobianco, J. A.; Speghini, A.; Bettinelli, M. Wet chemical synthesis and luminescence properties of erbium-doped nanocrystalline yttrium oxide. *Journal of Materials Research* **2004,** *19*, 3398-3407.

[46] Xue, X. J.; Uechi, S.; Tiwari, R. N.; Duan, Z. C.; Liao, M. S.; Yoshimura, M.; Suzuki, T.; Ohishi, Y. Size-dependent upconversion luminescence and quenching mechanism of liyf4: Er3+/yb3+ nanocrystals with oleate ligand adsorbed. *Optical Materials Express* **2013,** *3*.

[47] Yuan, D.; Tan, M. C.; Riman, R. E.; Chow, G. M. Comprehensive study on the size effects of the optical properties of nayf4:Yb,er nanocrystals. *Journal of Physical Chemistry C* **2013,** *117*, 13297-13304.

[48] Zhao, J.; Lu, Z.; Yin, Y.; McRae, C.; Piper, J. A.; Dawes, J. M.; Jin, D.; Goldys, E. M. Upconversion luminescence with tunable lifetime in nayf4:Yb,er nanocrystals: Role of nanocrystal size. *Nanoscale* **2013,** *5*, 944-52.

[49] Fischer, S.; Johnson, N. J. J.; Pichaandi, J.; Goldschmidt, J. C.; van Veggel, F. C. J. M. Upconverting core-shell nanocrystals with high quantum yield under low irradiance: On the role of isotropic and thick shells. *J Appl Phys* **2015,** *118*.

[50] Xu, C. T.; Svenmarker, P.; Liu, H. C.; Wu, X.; Messing, M. E.; Wallenberg, L. R.; Andersson-Engels, S. High-resolution fluorescence diffuse optical tomography developed with nonlinear upconverting nanoparticles. *Acs Nano* **2012,** *6*, 4788-4795.

[51] Fischer, S.; Frohlich, B.; Kramer, K. W.; Goldschmidt, J. C. Relation between excitation power density and er3+ doping yielding the highest absolute upconversion quantum yield. *J Phys Chem C* **2014,** *118*, 30106-30114.

[52] Pokhrel, M.; Kumar, G. A.; Sardar, D. K. Highly efficient nir to nir and vis upconversion in er3+ and yb3+ doped in m2o2s (m = gd, la, y). *Journal of Materials Chemistry A* **2013,** *1*, 11595-11606.

[53] Kumar, G. A.; Pokhrel, M.; Sardar, D. K. Absolute quantum yield measurements in yb/ho doped m2o2s (m=y, gd, la) upconversion phosphor. *Materials Letters* **2013,** *98*, 63-66.

[54] Hossan, M. Y.; Hor, A.; Luu, Q.; Smith, S. J.; May, P. S.; Berry, M. T. Explaining the nanoscale effect in the upconversion dynamics of β-nayf4:Yb3+,er3+ core and core-shell nanocrystals. *The Journal of Physical Chemistry C* **2017**.

[55] Shang, Y. F.; Hao, S. W.; Liu, J.; Tan, M. L.; Wang, N.; Yang, C. H.; Chen, G. Y. Synthesis of upconversion beta-nayf4:Nd3+/yb3+/er3+ particles with enhanced luminescent intensity through control of morphology and phase. *Nanomaterials* **2015,** *5*, 218-232.

[56] Xiang, G. T.; Zhang, J. H.; Hao, Z. D.; Zhang, X.; Pan, G. H.; Luo, Y. S.; Lu, W.; Zhao, H. F. Importance of suppression of yb3+ de-excitation to upconversion enhancement in beta-nayf4: Yb3+/er3+@beta-nayf4 sandwiched structure nanocrystals. *Inorg Chem* **2015,** *54*, 3921-3928.

[57] Wurth, C.; Kaiser, M.; Wilhelm, S.; Grauel, B.; Hirsch, T.; Resch-Genger, U. Excitation power dependent population pathways and absolute quantum yields of upconversion nanoparticles in different solvents. *Nanoscale* **2017,** *9*, 4283-4294.

[58] Gargas, D. J.; Chan, E. M.; Ostrowski, A. D.; Aloni, S.; Altoe, M. V. P.; Barnard, E. S.; Sanii, B.; Urban, J. J.; Milliron, D. J.; Cohen, B. E. et al. Engineering bright sub-10-nm upconverting nanocrystals for single-molecule imaging. *Nat Nanotechnol* **2014,** *9*, 300-305.

[59] Berry, M. T.; May, P. S. Disputed mechanism for nir-to-red upconversion luminescence in nayf4:Yb3+,er3+. *J Phys Chem A* **2015,** *119*, 9805-9811.

[60] Jung, T.; Jo, H. L.; Nam, S. H.; Yoo, B.; Cho, Y.; Kim, J.; Kim, H. M.; Hyeon, T.; Suh, Y. D.; Lee, H. et al. The preferred upconversion pathway for the red emission of lanthanide-doped upconverting nanoparticles, nayf4:Yb3+,er3+. *Phys Chem Chem Phys* **2015,** *17*, 13201-13205.

[61] Arppe, R.; Hyppanen, I.; Perala, N.; Peltomaa, R.; Kaiser, M.; Wurth, C.; Christ, S.; Resch-Genger, U.; Schaferling, M.; Soukka, T. Quenching of the upconversion luminescence of nayf(4):Yb(3)(+),er(3)(+) and nayf(4):Yb(3)(+),tm(3)(+) nanophosphors by water: The role of the sensitizer yb(3)(+) in non-radiative relaxation. *Nanoscale* **2015,** *7*, 11746-57.

[62] Scatena, L. F.; Brown, M. G.; Richmond, G. L. Water at hydrophobic surfaces: Weak hydrogen bonding and strong orientation effects. *Science* **2001,** *292*, 908-912.

[63] Fischer, S.; Bronstein, N. D.; Swabeck, J. K.; Chan, E. M.; Alivisatos, A. P. Precise tuning of surface quenching for luminescence enhancement in core–shell lanthanide-doped nanocrystals. *Nano Letters* **2016**.

[64] Chen, G. Y.; Shen, J.; Ohulchanskyy, T. Y.; Patel, N. J.; Kutikov, A.; Li, Z. P.; Song, J.; Pandey, R. K.; Agren, H.; Prasad, P. N. et al. (alpha-naybf4:Tm3+)/caf2 core/shell nanoparticles with efficient near-infrared to near-infrared upconversion for high-contrast deep tissue bioimaging. *Acs Nano* **2012,** *6*, 8280-8287.

[65] Guo, S. H.; Xie, X. J.; Huang, L.; Huang, W. Sensitive water probing through nonlinear photon upconversion of lanthanide-doped nanoparticles. *Acs Applied Materials & Interfaces* **2016,** *8*, 847-853.

[66] Muhr, V.; Würth, C.; Kraft, M.; Buchner, M.; Baeumner, A. J.; Resch-Genger, U.; Hirsch, T. Particle-size-dependent förster resonance energy transfer from upconversion nanoparticles to organic dyes. *Analytical Chemistry* **2017,** *89*, 4868-4874.

[67] Huang, K.; Liu, H. C.; Kraft, M.; Shikha, S.; Zheng, X.; Agren, H.; Wurth, C.; Resch-Genger, U.; Zhang, Y. A protected excitation-energy reservoir for efficient upconversion luminescence. *Nanoscale* **2018,** *10*, 250-259.

[68] Zhang, H.; Li, Y. J.; Lin, Y. C.; Huang, Y.; Duan, X. F. Composition tuning the upconversion emission in nayf4:Yb/tm hexaplate nanocrystals. *Nanoscale* **2011,** *3*, 963-966.

[69] Liu, Y. J.; Lu, Y. Q.; Yang, X. S.; Zheng, X. L.; Wen, S. H.; Wang, F.; Vidal, X.; Zhao, J. B.; Liu, D. M.; Zhou, Z. G. et al. Amplified stimulated emission in upconversion nanoparticles for super-resolution nanoscopy. *Nature* **2017,** *543*, 229-+.

[70] Zhang, Y. Q.; Xu, S.; Li, X. P.; Sun, J. S.; Zhang, J. S.; Zheng, H.; Zhong, H.; Hua, R. N.; Xia, H. P.; Chen, B. J. Concentration quenching of blue upconversion luminescence in tm3+/yb3+ co-doped gd-2(wo4)(3) phosphors under 980 and 808 nm excitation. *J Alloy Compd* **2017,** *709*, 147-157.

[71] Villanueva-Delgado, P.; Kramer, K. W.; Valiente, R.; de Jong, M.; Meijerink, A. Modeling blue to uv upconversion in beta-nayf4:Tm3+. *Physical Chemistry Chemical Physics* **2016,** *18*, 27396-27404.

[72] Zhang, J. Y.; Zhao, H.; Zhang, X. T.; Wang, X. Z.; Gao, H.; Zhang, Z. G.; Cao, W. W. Monochromatic near-infrared to near-infrared upconversion nanoparticles for high-contrast fluorescence imaging. *J Phys Chem C* **2014,** *118*, 2820-2825.

[73] Liu, H. C.; Xu, C. T.; Lindgren, D.; Xie, H. Y.; Thomas, D.; Gundlach, C.; Andersson-Engels, S. Balancing power density based quantum yield characterization of upconverting nanoparticles for arbitrary excitation intensities. *Nanoscale* **2013,** *5*, 4770-4775.

[74] Villanueva-Delgado, P.; Kramer, K. W.; Valiente, R. Simulating energy transfer and upconversion in beta-nayf4: Yb3+, tm3+. *J Phys Chem C* **2015,** *119*, 23648-23657.

[75] Zhao, J. B.; Jin, D. Y.; Schartner, E. P.; Lu, Y. Q.; Liu, Y. J.; Zvyagin, A. V.; Zhang, L. X.; Dawes, J. M.; Xi, P.; Piper, J. A. et al. Single-nanocrystal sensitivity achieved by enhanced upconversion luminescence. *Nat Nanotechnol* **2013,** *8*, 729-734.

[76] Gnach, A.; Lipinski, T.; Bednarkiewicz, A.; Rybka, J.; Capobianco, J. A. Upconverting nanoparticles: Assessing the toxicity. *Chemical Society Reviews* **2015,** *44*, 1561-1584.

[77] Li, J. X.; Chang, X. L.; Chen, X. X.; Gu, Z. J.; Zhao, F.; Chai, Z. F.; Zhao, Y. L. Toxicity of inorganic nanomaterials in biomedical imaging. *Biotechnology Advances* **2014,** *32*, 727-743.

[78] Wang, Y. F.; Sun, L. D.; Xiao, J. W.; Feng, W.; Zhou, J. C.; Shen, J.; Yan, C. H. Rare-earth nanoparticles with enhanced upconversion emission and suppressed rare-earth-ion leakage. *Chemistry-a European Journal* **2012,** *18*, 5558-5564.

[79] Hemmer, E.; Yamano, T.; Kishimoto, H.; Venkatachalam, N.; Hyodo, H.; Soga, K. Cytotoxic aspects of gadolinium oxide nanostructures for up-conversion and nir bioimaging. *Acta Biomaterialia* **2013,** *9*, 4734-4743.

[80] Peretyazhko, T. S.; Zhang, Q. B.; Colvin, V. L. Size-controlled dissolution of silver nanoparticles at neutral and acidic ph conditions: Kinetics and size changes. *Environmental Science & Technology* **2014,** *48*, 11954-11961.

[81] Rai, D.; Yui, M.; Kitamura, A.; Yoshikawa, H.; Felmy, A. R. Thermodynamic model for the solubility of ndf3(cr) in the na+-nh (+)(4)-nd3+-f--h2o system at 25 degrees c. *Journal of Solution Chemistry* **2013,** *42*, 1500-1517.

[82] Mioduski, T.; Guminski, C.; Zeng, D. W. Iupac- nist solubility data series. 100. Rare earth metal fluorides in water and aqueous systems. Part 1. Scandium group (sc, y, la). *J Phys Chem Ref Data* **2014,** *43*.

[83] Lisjak, D.; Plohl, O.; Ponikvar-Svet, M.; Majaron, B. Dissolution of upconverting fluoride nanoparticles in aqueous suspensions. *Rsc Advances* **2015,** *5*, 27393-27397.

[84] Lisjak, D.; Plohl, O.; Vidmar, J.; Majaron, B.; Ponikvar-Svet, M. Dissolution mechanism of upconverting ayf(4):Yb,tm (a = na or k) nanoparticles in aqueous media. *Langmuir* **2016,** *32*, 8222-8229.

[85] Barbier, O.; Arreola-Mendoza, L.; Del Razo, L. M. Molecular mechanisms of fluoride toxicity. *Chemico-Biological Interactions* **2010,** *188*, 319-333.

[86] Wurth, C.; Pauli, J.; Lochmann, C.; Spieles, M.; Resch-Genger, U. Integrating sphere setup for the traceable measurement of absolute photoluminescence quantum yields in the near infrared. *Analytical Chemistry* **2012,** *84*, 1345-1352.

[87] Hatami, S.; Wurth, C.; Kaiser, M.; Leubner, S.; Gabriel, S.; Bahrig, L.; Lesnyak, V.; Pauli, J.; Gaponik, N.; Eychmuller, A. et al. Absolute photoluminescence quantum yields of ir26 and ir-emissive cd1-xhgxte and pbs quantum dots - method- and material-inherent challenges. *Nanoscale* **2015,** *7*, 133-143.

[88] Resch-Genger, U.; Bremser, W.; Pfeifer, D.; Spieles, M.; Hoffmann, A.; DeRose, P. C.; Zwinkels, J. C.; Gauthier, F.; Ebert, B.; Taubert, R. D. et al. State-of-the art comparability of corrected emission spectra.1. Spectral correction with physical transfer standards and spectral fluorescence standards by expert laboratories. *Analytical Chemistry* **2012,** *84*, 3889-3898.

[89] Sillen, A.; Engelborghs, Y. The correct use of "average" fluorescence parameters. *Photochemistry and Photobiology* **1998,** *67*, 475-486.

[90] Plohl, O.; Kraft, M.; Kovac, J.; Belec, B.; Ponikvar-Svet, M.; Wurth, C.; Lisjak, D.; Resch-Genger, U. Optically detected degradation of nayf4:Yb,tm-based upconversion nanoparticles in phosphate buffered saline solution. *Langmuir* **2017,** *33*, 553-560.

[91] Kraft, M.; Würth, C.; Muhr, V.; Hirsch, T.; Resch-Genger, U. Particle-size-dependent upconversion luminescence of nayf4: Yb, er nanoparticles in organic solvents and water at different excitation power densities. *Nano Res* **2018**.

[92] Wilhelm, S.; Kaiser, M.; Wurth, C.; Heiland, J.; Carrillo-Carrion, C.; Muhr, V.; Wolfbeis, O. S.; Parak, W. J.; Resch-Genger, U.; Hirsch, T. Water dispersible upconverting nanoparticles: Effects of surface modification on their luminescence and colloidal stability. *Nanoscale* **2015,** *7*, 1403-1410.

[93] Klier, D. T.; Kumke, M. U. Upconversion luminescence properties of nayf4:Yb:Er nanoparticles codoped with gd3+. *Journal of Physical Chemistry C* **2015,** *119*, 3363-3373.

[94] Pakkila, H.; Yliharsila, M.; Lahtinen, S.; Hattara, L.; Salminen, N.; Arppe, R.; Lastusaari, M.; Saviranta, P.; Soukka, T. Quantitative multianalyte microarray immunoassay utilizing upconverting phosphor technology. *Analytical Chemistry* **2012,** *84*, 8628-8634.

[95] Wilhelm, S.; del Barrio, M.; Heiland, J.; Himmelstoss, S. F.; Galban, J.; Wolfbeis, O. S.; Hirsch, T. Spectrally matched upconverting luminescent nanoparticles for monitoring enzymatic reactions. *Acs Appl Mater Inter* **2014,** *6*, 15427-15433.

[96] Wilhelm, S.; Hirsch, T.; Patterson, W. M.; Scheucher, E.; Mayr, T.; Wolfbeis, O. S. Multicolor upconversion nanoparticles for protein conjugation. *Theranostics* **2013,** *3*, 239-248.

[97] Shan, J. N.; Uddi, M.; Yao, N.; Ju, Y. G. Anomalous raman scattering of colloidal yb3+,er3+ codoped nayf4 nanophosphors and dynamic probing of the upconversion luminescence. *Advanced Functional Materials* **2010,** *20*, 3530-3537.

[98] Wang, Y.; Deng, R. R.; Xie, X. J.; Huang, L.; Liu, X. G. Nonlinear spectral and lifetime management in upconversion nanoparticles by controlling energy distribution. *Nanoscale* **2016,** *8*, 6666-6673.

[99] Cao, T. Y.; Yang, Y.; Gao, Y. A.; Zhou, J.; Li, Z. Q.; Li, F. Y. High-quality water-soluble and surface-functionalized upconversion nanocrystals as luminescent probes for bioimaging. *Biomaterials* **2011,** *32*, 2959-2968.

[100] Ju, Q. A.; Luo, W. Q.; Liu, Y. S.; Zhu, H. M.; Li, R. F.; Chen, X. Y. Poly (acrylic acid)-capped lanthanide-doped bafcl nanocrystals: Synthesis and optical properties. *Nanoscale* **2010,** *2*, 1208-1212.

[101] Guan, Y.; Zhang, Y. J.; Zhou, T.; Zhou, S. Q. Stability of hydrogen-bonded hydroxypropylcellulose/poly(acrylic acid) microcapsules in aqueous solutions. *Soft Matter* **2009,** *5*, 842-849.

[102] Liu, F.; Ma, E.; Chen, D. Q.; Wang, Y. S.; Yu, Y. L.; Huang, P. Infrared luminescence of transparent glass ceramic containing er3+:Nayf4 nanocrystals. *J Alloy Compd* **2009,** *467*, 317-321.

[103] Ostrowski, A. D.; Chan, E. M.; Gargas, D. J.; Katz, E. M.; Han, G.; Schuck, P. J.; Milliron, D. J.; Cohen, B. E. Controlled synthesis and single-particle imaging of bright, sub-10 nm lanthanide-doped upconverting nanocrystals. *Acs Nano* **2012,** *6*, 2686-2692.

[104] Li, X. M.; Shen, D. K.; Yang, J. P.; Yao, C.; Che, R. C.; Zhang, F.; Zhao, D. Y. Successive layer-by-layer strategy for multi-shell epitaxial growth: Shell thickness and doping position dependence in upconverting optical properties. *Chemistry of Materials* **2013,** *25*, 106-112.

[105] Mousavi, M.; Thomasson, B.; Li, M.; Kraft, M.; Wurth, C.; Resch-Genger, U.; Andersson-Engels, S. Beam-profile-compensated quantum yield measurements of upconverting nanoparticles. *Physical Chemistry Chemical Physics* **2017,** *19*, 22016-22022.

[106] Qian, H. S.; Zhang, Y. Synthesis of hexagonal-phase core-shell nayf4 nanocrystals with tunable upconversion fluorescence. *Langmuir* **2008,** *24*, 12123-12125.

[107] Niu, N.; He, F.; Gai, S. L.; Li, C. X.; Zhang, X.; Huang, S. H.; Yang, P. P. Rapid microwave reflux process for the synthesis of pure hexagonal nayf4:Yb3+,ln(3+),bi3+ (ln(3+) = er3+, tm3+, ho3+) and its enhanced uc luminescence. *J Mater Chem* **2012,** *22*, 21613-21623.

[108] Ostermayer, F. W.; Vanderzi.Jp; Marcos, H. M.; Vanuiter.Lg; Geusic, J. E. Frequency upconversion in yf3-yb3+, tm3+. *Phys Rev B-Solid St* **1971,** *3*, 2698-+.

[109] He, C. F.; Zhao, D.; Qin, G. S.; Zheng, K. Z.; Qin, W. P. Enhanced ultraviolet upconversion luminescence of tm and yb codoped zrf4-baf2-laf3-alf3-naf glass. *J Nanosci Nanotechno* **2011,** *11*, 9494-9497.

[110] El-Agmy, R. M.; Luthy, W.; Graf, T.; Weber, H. P. Excitation of tm+3 at a wavelength of 1064 nm. *Appl Phys B-Lasers O* **2003,** *76*, 23-26.

[111] Yeh, D. C.; Sibley, W. A.; Suscavage, M. J. Efficient frequency upconversion of tm-3+ ions in yb-3+ doped barium thorium fluoride glass. *J Appl Phys* **1988,** *63*, 4644-4650.

[112] Peng, B.; Izumitani, T. Blue, green and 0.8 mu m tm3+, ho3+ doped upconversion laser glasses, sensitized by yb3+. *Opt Mater* **1995,** *4*, 701-711.

[113] Huang, S.; Lai, S. T.; Lou, L.; Jia, W.; Yen, W. M. Upconversion in laf3-tm3+. *Phys Rev B* **1981,** *24*, 59-63.

[114] Qin, G.; Huang, S.; Feng, Y.; Shirakawa, A.; Musha, M.; Ueda, K. I. Power scaling of tm3+ stop doped zblan blue upconversion fiber lasers: Modeling and experiments. *Appl Phys B-Lasers O* **2006,** *82*, 65-70.

[115] Liu, H. C.; Xu, C. T.; Dumlupinar, G.; Jensen, O. B.; Andersen, P. E.; Andersson-Engels, S. Deep tissue optical imaging of upconverting nanoparticles enabled by exploiting higher intrinsic quantum yield through use of millisecond single pulse excitation with high peak power. *Nanoscale* **2013,** *5*, 10034-10040.

[116] Braud, A.; Girard, S.; Doualan, J. L.; Thuau, M.; Moncorge, R.; Tkachuk, A. M. Energy-transfer processes in yb : Tm-doped ky3f10, liyf4, and bay2f8 single crystals for laser operation at 1.5 and 2.3 mu m. *Phys Rev B* **2000,** *61*, 5280-5292.

[117] Yang, X.; Guo, L. F.; Zuo, Y. H.; Li, J.; Mou, H. C. The efficient monochromatic 800 nm near-infrared emission from tm3+-doped naybf4 upconversion luminescence nanoparticles. *Optoelectron Adv Mat* **2016,** *10*, 467-471.

[118] Xue, X. J.; Thitsa, M.; Cheng, T. L.; Gao, W. Q.; Deng, D. H.; Suzuki, T.; Ohishi, Y. Laser power density dependent energy transfer between tm3+ and tb3+: Tunable upconversion emissions in nayf4:Tm3+,tb3+,yb3+ microcrystals. *Opt Express* **2016,** *24*, 26307-26321.

[119] Trindade, C. M.; Rego, F. G.; Astrath, N. G. C.; Jacinto, C.; Gouveia-Neto, A. S. Uv-visible-nir light generation through frequency upconversion in tm3+-doped low silica calcium aluminosilicate glasses using multiple excitation around 1.2 mu m. *J Solid State Chem* **2018,** *260*, 147-150.

[120] Kraft, M.; Würth, C.; Palo, E.; Soukka, T.; Resch-Genger, U. Colour-optimized quantum yields of yb, tm co-doped upconversion nanocrystals. *Methods and Applications in Fluorescence* **2018**.

[121] Palo, E.; Tuomisto, M.; Hyppanen, I.; Swart, H. C.; Holsa, J.; Soukka, T.; Lastusaari, M. Highly uniform up-converting nanoparticles: Why you should control your synthesis even more. *J Lumin* **2017,** *185*, 125-131.

[122] Liu, Q.; Sun, Y.; Yang, T. S.; Feng, W.; Li, C. G.; Li, F. Y. Sub-10 nm hexagonal lanthanide-doped naluf4 upconversion nanocrystals for sensitive bioimaging in vivo. *J Am Chem Soc* **2011,** *133*, 17122-17125.

[123] Huang, P.; Zheng, W.; Zhou, S. Y.; Tu, D. T.; Chen, Z.; Zhu, H. M.; Li, R. F.; Ma, E.; Huang, M. D.; Chen, X. Y. Lanthanide-doped liluf4 upconversion nanoprobes for the detection of disease biomarkers. *Angew Chem Int Edit* **2014,** *53*, 1252-1257.

[124] Fischer, S.; Swabeck, J. K.; Alivisatos, A. P. Controlled isotropic and anisotropic shell growth in beta-nalnf(4) nanocrystals induced by precursor injection rate. *J Am Chem Soc* **2017,** *139*, 12325-12332.

[125] Bogdan, N.; Vetrone, F.; Ozin, G. A.; Capobianco, J. A. Synthesis of ligand-free colloidally stable water dispersible brightly luminescent lanthanide-doped upconverting nanoparticles. *Nano Letters* **2011,** *11*, 835-840.

9 List of Publications

9.1 Articles in Peer Reviewed Journals

1. Kaiser, M.; Würth, C.; *Kraft, M.*; Soukka, T.; Resch-Genger, U. "**Green-red colour tuning of $NaYF_4$: Yb^{3+}, Er^{3+} nanoparticles by variation of doping concentration and modulation of excitation power**"; to be submitted
   DOI:
2. *Kraft, M.*; Würth, C.; Palo, E.; Soukka, T.; Resch-Genger, U. "**Colour-Optimized Quantum Yields of Yb, Tm Co-doped Upconversion Nanocrystals**", submitted to journal *Methods and Applications in Fluorescence*
   DOI:
3. *Kraft, M.*; Würth, C.; Muhr, V.; Hirsch, T.; Resch-Genger, U. "**Particle size dependent upconversion luminescence of $NaYF_4$: Yb, Er nanoparticles in organic solvents and water at different excitation power densities**", Nano Res. (2018)
   DOI: 10.1007/s12274-018-2159-9
4. Huang, K.; Liu, H.; *Kraft, M.*; Shikha, S.; Zheng, X.; Ågren, H.; Würth, C.; Resch-Genger, U.; Zhang, Y. "**Protected excitation-energy reservoir for efficient upconversion luminescence**", Nanoscale, 2018, 10, 250-259
   DOI: 10.1039/C7NR06900F
5. Monirehalsadat, M.; Thomasson, B.; Li, M.; *Kraft, M.*; Würth, C.; Resch-Genger, U.; Andersson-Engels, S. "**Beam-profile-compensated quantum yield measurements of upconverting nanoparticles**", Phys. Chem. Chem. Phys., 2017,19, 22016-22022
   DOI: 10.1039/C7CP03785F
6. Kaiser, M.; Würth, C.; *Kraft, M.*; Hyppänen, I.; Soukka, T.; Resch-Genger, U. "**Power-dependent upconversion quantum yield of $NaYF_4$:Yb^{3+},Er^{3+} nano- and micrometer-sized particles – measurements and simulations**", Nanoscale, 2017, 9, 10051-10058
   DOI: 10.1039/C7NR02449E
7. Muhr, V.; Würth, C.; *Kraft, M.*; Buchner, M.; Resch-Genger, U.; Bäumer, A.; Hirsch, T. "**Particle-size Dependent Förster Resonance Energy Transfer from Upconversion Nanoparticles to Organic Dyes**", Anal. Chem., 2017, 89 (9), 4868–4874
   DOI: 10.1021/acs.analchem.6b04662
8. Plohl, O.*****; *Kraft, M.******; Kovač, J.; Belec, B.; Ponikvar-Svet, M.; Würth, C.; Lisjak, D.; Resch-Genger, U. "**Optically Detected Degradation of $NaYF_4$:Yb,Tm-Based Upconversion Nanoparticles in Phosphate Buffered Saline Solution**", Langmuir, 2017, 33 (2), pp 553–560
   DOI: 10.1021/acs.langmuir.6b03907

***** means equal contributing author

9.2 Contribution to Oral Presentations at Scientific Conferences

1. Hirsch, T.; Buchner, M.; Muhr, V.; Calavia, P.G.; *Kraft, M.*; Würth, C.; Russell, D.A.; Bäumner, A.J.; Resch-Genger, U.; Altaba, M.J.M. "**Dye Modified Upconversion Nanoparticles For Time-Resolved Applications Based On Energy Transfer**", Methods and Applications in Fluorescence, Bruges (Belgium), 2017

2. Resch-Genger, U.; *Kraft, M.*; Würth, C.; Kaiser, M.; Muhr, V.; Hirsch, T. "**Effect Of Particle Size And Excitation Power Density On The Luminescence Efficiency Of Upconversion Nanocrystals In Different Dispersion Media**", Methods and Applications in Fluorescence, Bruges (Belgium), 2017
3. Muhr, V.; Würth, C.; *Kraft, M.*; Bäumner, A.; Resch-Genger, U.; Hirsch, T. "**Effect of Nanoparticle Size on Time-Resolved Upconversion Resonance Energy Transfer**", Materials Research Society, Spring Meeting & Exhibit, Phoenix (Arizona, USA), 2017
4. *Kraft, M.*; Würth, C.; Kaiser, M.; Muhr, V.; Resch-Genger, U. "**Particle Size Dependent Absolute Photoluminescence Quantum Yields and Lifetimes of Hexagonal β -$NaYF_4$: 2 % Er^{3+} 20 % Yb^{3+} Upconversion Nanoparticles in Cyclohexane and Water**", UPCON conference, Wroclaw (Poland), 2016
5. Würth, C.; Kaiser, M.; *Kraft, M.*; Muhr, V.; Wilhelm, S.; Hirsch, T.; Resch-Genger, U. "**Setup for the power-dependent absolute quantum yield measurements of luminescent reporters in the VIS and IR spectral region: example of upconversion nanoparticles**", SPIE Photonics West, San Francisco, 2016
6. Resch-Genger, U.; Moser, M.; *Kraft, M.*; Behnke, T.; Falkenhagen, J.; Kaiser, M.; Muhr, V.; Hirsch, T. "**Simple method for the quantification of PEG ligands and guidelines to the spectroscopic characterization of upconversion nanoparticles**", SPIE Photonics West, San Francisco, 2016
7. *Kraft, M.*; Kaiser, M.; Würth, C.; Soukka, T.; Resch-Genger, U. "**Absolute Photoluminescence Quantum Yields of Oleic Acid-Stabilized Hexagonal β-$NaYF_4$: x % Tm^{3+}, 20 % Yb^{3+} Upconversion Nanoparticles**", DPG Frühjahrstagung, Berlin, 2014

9.3 Poster Presentations at Scientific Conferences

1. *Kraft, M.*; Würth, C.; Kaiser, M.; Muhr, V.; Hirsch, T.; Resch-Genger, U. "**Particle Size Dependent Optical Properties of Hexagonal β-$NaYF_4$: 2 % Er^{3+}, 20 % Yb^{3+} Upconversion Nanoparticles in Cyclohexane and Water**", International Conference on Advanced Materials and Nanotechnology AMN8, Queenstown, 2017
2. *Kraft, M.;* Würth, C.; Kaiser, M.; Muhr, V.; Hirsch, T.; Resch-Genger, U. "**Absolute Photoluminescence Quantum Yields and Lifetimes of 21, 26 and 31 nm Sized Hexagonal β-$NaYF_4$: Er, Yb Upconversion Particles in Cyclohexane and Aqueous Solutions**", Adlershofer Forschungs-forum, Berlin, 2015
3. *Kraft, M.*; Würth, C.; Kaiser, M.; Muhr, V.; Hirsch, T.; Resch-Genger, U. "**Absolute Photoluminescence Quantum Yields and Lifetimes of Differently Sized Hexagonal β -NaYF4: 2 % Er^{3+}, 20 % Yb^{3+} Upconversion Nanoparticles in Cyclohexane and Water**", Methods and Applications in Fluorescence, Würzburg, 2015
4. *Kraft, M.*; Kaiser, M.; Würth, C.; Soukka, T.; Resch-Genger, U. "**Absolute Photoluminescence Quantum Yields and Lifetimes of in Toluene Dispersed Hexagonal β-$NaYF_4$: x % Tm^{3+}, 20 % Yb^{3+} Upconversion Nanoparticles**", DPG Sommer-Schule, Bad Honnef, 2015
5. *Kraft, M.*; Kaiser, M.; Würth, C.; Soukka, T.; Resch-Genger, U. "**Absolute Photoluminescence Quantum Yields and Lifetimes of in Toluene Dispersed Hexagonal β-$NaYF_4$: x % Tm^{3+}, 20 % Yb^{3+} Upconversion Nanoparticles**", DPG Frühjahrstagung, Berlin, 2015
6. *Kraft, M.*; Kaiser, M.; Würth, C.; Soukka, T.; Resch-Genger, U. "**Absolute Photoluminescence Quantum Yields of with Oleic Acid Stabalized Hexagonal β-$NaYF_4$: x % Tm^{3+}, 20 % Yb^{3+} Upcon-version Nanoparticles**", DPG Frühjahrstagung, Berlin, 2014

Danksagung

An dieser Stelle möchte ich meinen ganz besonderen Dank nachstehenden Personen entgegen bringen, ohne deren Mithilfe die Anfertigung dieser Promotionsschrift niemals zustande gekommen wäre: Mein herzlichster Dank gilt zunächst erstmal meiner Betreuerin von der Bundesanstalt für Materialforschung und –prüfung (BAM), Ute Resch-Genger, und meinem Doktorvater von der Humboldt-Universität zu Berlin, Stefan Kirstein. Vielen lieben Dank für die Betreuung dieser Promotionsarbeit und die damit verbundenen produktiven Gespräche, die vielen Anregungen und den konstruktiven Austausch.

Ein ganz besonderer Dank gilt auch all meinen Kollegen aus der Abteilung 1.2 Biophotonik der BAM. Besonders hervorheben möchte ich dabei Christian Würth, dem ich für die freundliche Hilfe und mannigfache Ideengebung, die mir einen kritischen Zugang zu dieser Thematik eröffnete, danken möchte. Die zahlreichen Gespräche auf intellektueller und persönlicher Ebene werden mir immer als bereichernder und konstruktiver Austausch in Erinnerung bleiben. Ein ganz besonderer Dank gilt dabei natürlich auch meinem Kollegen Martin Kaiser für die vielen intellektuellen Gespräche auf dem Gebiet der Aufkonversion. Unvergessen werde mir natürlich auch alle anderen Kollegen bleiben, die mir in dieser Zeit zur Seite standen.

Von meinem besonderen Dank sind auch alle Ko-Autoren von meinen verschiedenen Publikationen nicht ausgenommen. Ganz besonders hervorheben möchte ich dabei Verena Muhr und Thomas Hirsch von der Universität Regensburg, Olivija Plohl und Darja Lisjak von der University of Ljubljana, Arefeh Mousavi, Meng Li und Stefan Andersson-Engels von der Lund University, Kai Huang, Haichun Liu und Yong Zhang von der National University of Singapore, Emilia Palo, Riikka Arppe-Tabbara und Tero Souka von der University of Turku und Thomas Nann vom MacDiarmid Institute for Advanced Materials and Nanotechnology.

In diesem Sinne möchte ich auch nochmal der BAM für die Finanzierung meiner Doktorarbeit und dem Europäischen Netzwerk COST CM1403 für die Finanzierung meines zwei-wöchigen Forschungsaufenthaltes an der Lund University bedanken.

Zuletzt gilt mein ganz besonderer Dank noch meiner Familie, meiner Mutter Martina Kraft, meinem Vater Gerhard Kraft, meinen Geschwistern Mathias und Michael Kraft, meiner Schwägerin Stefanie Kraft, meiner Nichte Leonie Kraft und natürlich auch allen die namentlich hier nicht genannt sind.

Selbstständigkeitserklärung

Ich erkläre, dass ich diese Dissertation selbständig und nur unter Verwendung der von mir gemäß § 7 Abs. 3 der Promotionsordnung der Mathematisch-Naturwissenschaftlichen Fakultät, veröffentlicht im Amtlichen Mitteilungsblatt der Humboldt-Universität zu Berlin Nr. 126/2014 am 18.11.2014, angegebenen Hilfsmittel angefertigt habe.

15. Oktober 2018

Datum Unterschrift Doktorand/in